

2020

## Search for heavy resonance decaying into a photon and a Higgs boson with the ATLAS detector at the LHC

Boping Chen  
*Iowa State University*

Follow this and additional works at: <https://lib.dr.iastate.edu/etd>

---

### Recommended Citation

Chen, Boping, "Search for heavy resonance decaying into a photon and a Higgs boson with the ATLAS detector at the LHC" (2020). *Graduate Theses and Dissertations*. 18292.  
<https://lib.dr.iastate.edu/etd/18292>

This Thesis is brought to you for free and open access by the Iowa State University Capstones, Theses and Dissertations at Iowa State University Digital Repository. It has been accepted for inclusion in Graduate Theses and Dissertations by an authorized administrator of Iowa State University Digital Repository. For more information, please contact [digirep@iastate.edu](mailto:digirep@iastate.edu).

**Search for heavy resonance decaying into a photon and a Higgs boson  
with the ATLAS detector at the LHC**

by

**Boping Chen**

A dissertation submitted to the graduate faculty  
in partial fulfillment of the requirements for the degree of

DOCTOR OF PHILOSOPHY

Major: High Energy Physics

Program of Study Committee:  
Chunhui Chen, Major Professor  
Soeren A. Prell  
Kerry Whisnant  
Kirill Tuchin  
Mani Mina

The student author, whose presentation of the scholarship herein was approved by the program of study committee, is solely responsible for the content of this dissertation. The Graduate College will ensure this dissertation is globally accessible and will not permit alterations after a degree is conferred.

Iowa State University

Ames, Iowa

2020

Copyright © Boping Chen, 2020. All rights reserved.

**DEDICATION**

I would like to dedicate this thesis to my parents Yuliang Chen and Yinghong Feng without whose support I would not have been able to complete this work.

# TABLE OF CONTENTS

	Page
LIST OF TABLES . . . . .	v
LIST OF FIGURES . . . . .	vi
ACKNOWLEDGMENTS . . . . .	xii
ABSTRACT . . . . .	xiii
CHAPTER 1. INTRODUCTION . . . . .	1
CHAPTER 2. THEORY: STANDARD MODEL . . . . .	2
2.1 Historical background of particle discovery . . . . .	2
2.2 Fermion and Boson . . . . .	5
2.2.1 Fermion . . . . .	7
2.2.2 Boson . . . . .	8
2.3 Standard model . . . . .	14
2.3.1 Gauge theory . . . . .	14
2.3.2 Spontaneous symmetry breaking and Higgs mechanism . . . . .	15
2.3.3 Beyond Standard model . . . . .	17
CHAPTER 3. PARTICLE DETECTOR . . . . .	19
3.1 CERN and LHC . . . . .	19
3.2 ATLAS detector . . . . .	21
3.2.1 ATLAS coordinate . . . . .	21
3.2.2 Inner detector . . . . .	24
3.2.3 EM calorimeter . . . . .	25
3.2.4 Hadronic calorimeter . . . . .	25
3.2.5 Muon detector . . . . .	27
3.2.6 Forward detectors and luminosity . . . . .	28
3.2.7 Trigger, data acquisition . . . . .	29
3.2.8 Underlying Events and pile-up . . . . .	29
3.3 Object reconstruction . . . . .	30
3.3.1 Track and primary vertex . . . . .	30
3.3.2 Electron and photon . . . . .	31
3.3.3 Muon . . . . .	31
3.3.4 Jet . . . . .	32
3.3.5 Missing $E_T$ . . . . .	33



CHAPTER 4. PHYSICS ANALYSIS DETAIL . . . . .	34
4.1 Analysis motivation and overview . . . . .	34
4.2 Monte Carlo sample and Data . . . . .	36
4.3 Event selection . . . . .	38
4.3.1 Trigger . . . . .	39
4.3.2 Baseline selection . . . . .	39
4.3.3 Large- $R$ jet mass window optimization . . . . .	41
4.3.4 The $b$ -tagging algorithm and previous ATLAS $H \rightarrow b\bar{b}$ tagger . . . . .	45
4.3.5 Center-of-mass subjet algorithm . . . . .	47
4.3.6 Optimization of the selection criteria of photon and large- $R$ jet $p_T$ . . . . .	53
4.4 Signal sample overall efficiency . . . . .	54
4.5 Signal model . . . . .	54
4.5.1 Signal shape probability density function . . . . .	54
4.5.2 Signal pdf parametrization and interpolation . . . . .	58
4.6 Background model . . . . .	61
4.6.1 Background composition . . . . .	61
4.6.2 Background pdf . . . . .	61
4.6.3 Control region study . . . . .	63
4.6.4 F-test study for background model . . . . .	71
4.7 Systematic uncertainty . . . . .	75
4.7.1 Detector modeling systematic uncertainties . . . . .	75
4.7.2 Theoretical systematic uncertainties . . . . .	79
4.7.3 Background modeling systematic uncertainties . . . . .	84
CHAPTER 5. ANALYSIS STATISTICAL RESULT . . . . .	86
5.1 Data distribution . . . . .	86
5.2 Likelihood and hypothesis testing . . . . .	88
5.2.1 Search for the signal . . . . .	91
5.2.2 Limit . . . . .	92
CHAPTER 6. CONCLUSION . . . . .	98
6.1 SUMMARY . . . . .	98
6.1.1 Future Work . . . . .	98
APPENDIX. ADDITIONAL MATERIAL . . . . .	109
.1 Signal systematic uncertainties . . . . .	109

## LIST OF TABLES

	<b>Page</b>
Table 4.1	Branching ratios of Higgs boson . . . . . 35
Table 4.2	Expected composition of backgrounds at luminosity = $139 \text{ fb}^{-1}$ in the range of $m_{J\gamma}$ from 600 GeV to 4200 GeV. . . . . 62
Table 4.3	$F$ -test results with control region data events. 3-parameters function provides the best fit performance for both single and double $b$ -tagged categories. 74
Table 4.4	Qualitative summary of the systematic uncertainties included in this analysis. . . . . 78
Table 4.5	Breakdown of systematics effects. The systematic variations on $X \rightarrow H + \gamma$ signal modeling effecting the signal selection efficiency, the fitted peak position and the width of the $m_{J\gamma}$ distribution. The mass of the signal resonance mass here is 2000 GeV. . . . . 80
Table 4.6	Breakdown of systematics effects. The systematic variations on $X \rightarrow H + \gamma$ signal modeling effecting the signal selection efficiency, the fitted peak position and the width of the $m_{J\gamma}$ distribution. The mass of the signal resonance mass here is 2000 GeV. . . . . 81
Table 4.7	Acceptance difference due to the effect of parton shower for $m = 1000, 3000, 5000$ GeV. . . . . 84

## LIST OF FIGURES

		Page
Figure 2.2	Plum pudding model by J. J. Thomson. The electrons are surrounded by a volume of positive charge, like negatively-charged “plums” embedded in a positively-charged “pudding”. <a href="#">Figure is from wikipedia.</a> . . . . .	3
Figure 2.4	Rutherford model by Hans Geiger, Ernest Marsden and Ernest Rutherford. In this model, charge and mass are highly concentrated in a small region at the center of the atom, which is called “nucleus” of the atom. And the nucleus is surrounded by the electron. <a href="#">Figure is from wikipedia.</a> . . . . .	4
Figure 2.6	Summary of the particles in SM. In general, the fundamental particles are divided into two groups: Fermion (left) and Boson (right). Fermion is the unit to build the matter and Boson is the one propagate interaction . . . . .	6
Figure 2.8	Feynman diagram for the tree-level QED interaction between electron and positron. (a): electron positron annihilation; (b) electron interacts with positron with photon as propagator. . . . .	11
Figure 2.10	Feynman diagram for the tree-level QCD interaction between quark and anti-quark. (a): quark interacts with anti-quark with gluon as propagator; (b) quark anti-quark annihilation. . . . .	12
Figure 2.12	Feynman diagram for the tree-level weak interaction between. (a): electron positron annihilation; (b) electron interacts with electron neutrino and generate the $W$ boson. . . . .	13
Figure 3.2	Overall view of the LHC. There are four main detectors: ATLAS, CMS, ALICE and LHCb. . . . .	20
Figure 3.4	Overall view of ATLAS detector. It includes the inner detector, EM calorimeter, Hadronic calorimeter, muon spectrometer and forward detectors. . . . .	22
Figure 3.6	ATLAS coordinate system . . . . .	22
Figure 3.8	Example of pseudorapidity value in the X-Z plane. The angle separation between two dashed lines are $15^\circ$ . . . . .	23
Figure 3.10	The overall view of ID. It consists of three parts: Pixel Detector, Semiconductor Tracker and Transition Radiation Tracker. . . . .	24

Figure 3.12	The overall view of EM calorimeter and Hadronic calorimeter. . . . .	26
Figure 3.14	The overall view of muon system. There are four subsections of the muon system: Thin Gap Chambers, Resistive Plate Chambers, Monitored Drift Tubes, and Cathode Strip Chambers. . . . .	27
Figure 3.16	The overall view of forward detector. There are four subsections of the forward detector: Luminosity measurement using Cerenkov Integrating Detector, Zero-Degree Calorimeter, ATLAS Forward Proton Detector and Absolute Luminosity For ATLAS. . . . .	28
Figure 4.2	Feynman diagram for the dominant SM background. (a) Example for $\gamma$ +jet; (b) example for $Z/W + \gamma$ and (c) example for $t\bar{t} + \gamma$ . . . . .	37
Figure 4.3	Feynman diagram for signal channel $Z' \rightarrow H\gamma$ . . . . .	38
Figure 4.4	Efficiency of photon triggers requiring loose identification and $E_T > 25$ GeV (squares), 35 GeV (triangles) and 140 GeV (inverted triangles, which is the one used in this analysis) and the efficiency of photon trigger requiring tight identification and $E_T$ greater than 22 GeV (circles) for data (filled markers) and MC simulated samples (empty markers) as a function of the transverse energy of the photon candidates reconstructed offline passing the tight identification selection with $ \eta  < 2.37$ , excluding the transition region between the barrel and endcap electromagnetic calorimeters at $1.37 <  \eta  < 1.52$ . The efficiencies were measured with the bootstrap method using events recorded with a Level-1 trigger requiring an electromagnetic cluster with $E_T > 15$ GeV. This Level-1 requirement is fully efficient selecting offline photons with $E_T > 22$ GeV. No background subtraction is applied. The error bars represent the statistical uncertainty. Small drop in efficiency of 22 GeV tight trigger at high $E_T$ has no effect in trigger performance, since 35 GeV loose trigger should be used above 50 GeV. . . . .	40
Figure 4.5	Signal efficiencies of events passing the baseline selection (before categorization) . . . . .	42
Figure 4.6	Data/MC comparisons after baseline selections for (a) photon $p_T$ , (b) large- $R$ jet $p_T$ , (c) large- $R$ jet mass and (d) large- $R$ jet $\eta$ . . . . .	43
Figure 4.7	The large- $R$ jets (a) mass and (b) $p_T$ distributions from the data events and MC simulated signal events after the baseline event selection. . . . .	44
Figure 4.8	(a) The large- $R$ jet mass window boundaries as functions of large- $R$ jet $p_T$ . The boundaries are parameterized with a fourth-order polynomial. (b) The large- $R$ jet mass selection efficiency as a function of resonance mass. . . . .	45

Figure 4.9	Illustration for the b-jet and light jet. For the b-jet, the associated tracks are from the secondary vertex, while for other jets, the tracks are from the primary vertex. . . . .	46
Figure 4.11	CoM subjet reconstruction and track association . . . . .	49
Figure 4.13	Illustration of the constituent particle distribution of a jet. (a)Higgs jet in the lab frame. (b)Higgs jet in the jet rest frame. (c) QCD jet in its rest frame.	50
Figure 4.14	The fraction of the MC signal events in different $b$ -tagged categories as a function of resonance mass after baseline selection and large- $R$ jet mass optimization. . . . .	51
Figure 4.16	QCD jet rejection as a function of $h \rightarrow b\bar{b}$ efficiency when applying double $b$ -tagging selection on subjets found by the anti- $kt$ $R=0.2$ subjet, VR subjet, ExKt subjet, and CoM subjet algorithms in different $p_T$ regions. In general, CoM subjet algorithm has the best performance among these four $H \rightarrow b\bar{b}$ tagger. . . . .	52
Figure 4.18	Top plots: The optimized minimum $p_T$ requirement of the photon as a function of the resonance mass $m_{Z'}$ for MC simulated signal events in the single $b$ -tagged (Left) and double $b$ -tagged categories (Right). Bottom plots: the relative selection efficiencies of the optimized $p_T$ requirements of the photon and the large- $R$ jet as a function of the resonance mass $m_{Z'}$ for MC simulated signal events in the single $b$ -tagged (Left) and double $b$ -tagged categories (Right). . . . .	55
Figure 4.19	Signal overall efficiency after all the selection introduced in this section. . .	56
Figure 4.21	Signal shape parameterization with an analytical function for several different resonance masses ( $m_{Z'}$ ). Plots on the left shows the result for double $b$ -tagged category and plots on the right presents the result for single $b$ -tagged category. The black points are from MC simulation events, the green curves are from the fitting result, and the red curves are from the analytical pdf in which their parameters are set to the predicted values from the parametrized function as described in Equation 4.3. . . . .	57
Figure 4.23	Parameterization of the signal PDF parameters: $\sigma_{CB}$ (Top left) , $\alpha_{CB}$ (Top right), $\sigma_{Gauss}$ (Bottom left) and $f_{CB}$ (Bottom right) as functions of the resonance mass in the double $b$ -tagged category. . . . .	59
Figure 4.25	Parameterization of the signal PDF parameters: $\sigma_{CB}$ (Top left) , $\alpha_{CB}$ (Top right), $\sigma_{Gauss}$ (Bottom left) and $f_{CB}$ (Bottom right) as functions of the resonance mass in the single $b$ -tagged category. . . . .	60

Figure 4.27	Comparison of signal shapes interpolated from coefficients parametrization (red) and the signal shapes obtained from MC events fit (blue) for (a) double $b$ -tagged and (b) single $b$ -tagged categories. The interpolated shape are plotted with 100 GeV per step. . . . .	61
Figure 4.29	large- $R$ jet mass windows(central area between red curve) and side-band boundaries(outer area between black and blue area) as functions of large- $R$ jet $p_T$ . Area between red and black curves is a 5GeV gap between signal region and side-band region. . . . .	64
Figure 4.31	Comparison of $m_{J\gamma}$ distributions for MC simulated events in (a) single $b$ -tagged and (b) double $b$ -tag signal and side-band regions. Number of background events in side-band and signal regions are in the same order and compatible. . . . .	65
Figure 4.33	Comparison of $m_{J\gamma}$ distributions for MC simulated events in (a) single $b$ -tagged and (b) double $b$ -tag signal and un-tagged regions. Number of background events in un-tagged region is around 10 times more than the ones in the single $b$ -tagged signal region, and 100 times more than the ones in double $b$ -tagged signal region. Good shape agreements observed between signal and un-tagged regions. . . . .	67
Figure 4.35	Signal region (SR) and control region (CR) definitions. Green area is the signal region whose events pass the large- $R$ jet mass optimization and the $b$ -tagged selection, while the blue area is the control region whose events fall into large- $R$ jet mass side-band region and fail the looser $b$ -tagging selection criteria. The red vertical area represents the 5 GeV gap between signal region and large- $R$ jet mass side-band, and the red horizontal line represents the difference in the $b$ -tagging selection criteria. . . . .	68
Figure 4.37	Control region single $b$ -tagged data/MC comparison for (a) large- $R$ jet $p_T$ , (b) large- $R$ jet $\eta$ , (c) photon $p_T$ and (d) invariant mass of large- $R$ jet and photon. . . . .	69
Figure 4.39	Control region double $b$ -tagged data/MC comparison for (a) large- $R$ jet $p_T$ , (b) large- $R$ jet $\eta$ , (c) photon $p_T$ and (d) invariant mass of large- $R$ jet and photon. . . . .	70
Figure 4.41	The comparison of the $m_{J\gamma}$ distributions for the MC simulated events in the signal region and control regions and their ratio plot. The total number of events in the control region is scaled to be the same as the one in the signal region. A second-order polynomial function is used to fitted to the ratio plots. . . . .	72

Figure 4.43	Background fits to the data $m_{J\gamma}$ mass distributions in the control region. The bottom pad shows the significance, which is the variation between fitted function and the data distribution divided by the uncertainty of data events in that bin. . . . .	74
Figure 4.44	PDF uncertainty in the signal efficiency as a function of the resonance mass. . . . .	82
Figure 4.45	QCD scale uncertainty in the signal efficiency as a function of the resonance mass. . . . .	83
Figure 4.47	The number of spurious signal events, which is from the fitting with signal+background model using data events in (a) single b-tagged control region and (b) double b-tagged control region. The Y-axis is the absolute value of number of spurious signal events, in log scale. The number of spurious signal events distribution are fitted with a straight line, the red line. To cover most of the spurious signal events, the red line is moved up for $\log 2$ and becomes the black straight line, which is used for the limit calculation. . . . .	85
Figure 5.2	(a) and (b): Distribution of the reconstructed $m_{J\gamma}$ in the single b-tagged and double b-tagged categories. Blue curves show the background only fitting result. Hypothetical signal distributions for $m_{Z'} = 2$ TeV and $m_{Z'} = 3$ TeV with arbitrary normalizations are plotted for illustration purposes. The bottom panel gives the significance (deviation / statistical uncertainty) for each bin. The impact on the background fit from the statistical uncertainties of background pdf parameters is shown as a light band around the solid line. . . . .	87
Figure 5.4	The standard normal distribution and the relationship between p-value at 0.05 and the significance. . . . .	91
Figure 5.6	p-value scan for different resonance mass $m_{J\gamma}$ hypothesis with a step 25 GeV. Left axis shows the p-value and the right axis shows the corresponding significance value. No large significance is observed along the search region and the largest significance is below $3\sigma$ . The largest significance is $2.69\sigma$ at 775 GeV. . . . .	92
Figure 5.8	Observed and expected 95 % confidence-level limits on $\sigma \times B$ for search range. No obvious deviation is observed. . . . .	95
Figure 5.10	Comparison between the latest ATLAS result and the previous CMS result. On top of the statistic gain, the ATLAS upper limit is 30 % better than CMS result . . . . .	97
Figure 6.2	VBF topology for $H\gamma$ resonance. . . . .	99

Figure .2	Signal resonance mass at 2000 GeV, in single $b$ -tagged SR. Comparison of $H\gamma$ mass spectrum between nominal signal MC sample and all the systematic variations. . . . .	110
Figure .4	Signal resonance mass at 2000 GeV, in single $b$ -tagged SR. Comparison of $H\gamma$ mass spectrum between nominal signal MC sample and all the systematic variations. . . . .	111
Figure .6	Signal resonance mass at 2000 GeV, in single $b$ -tagged SR. Comparison of $H\gamma$ mass spectrum between nominal signal MC sample and all the systematic variations. . . . .	112
Figure .8	Signal resonance mass at 2000 GeV, in double $b$ -tagged SR. Comparison of $H\gamma$ mass spectrum between nominal signal MC sample and all the systematic variations. . . . .	113
Figure .10	Signal resonance mass at 2000 GeV, in double $b$ -tagged SR. Comparison of $H\gamma$ mass spectrum between nominal signal MC sample and all the systematic variations. . . . .	114
Figure .12	Signal resonance mass at 2000 GeV, in double $b$ -tagged SR. Comparison of $H\gamma$ mass spectrum between nominal signal MC sample and all the systematic variations. . . . .	115



## ACKNOWLEDGMENTS

I would like to take this opportunity to express my thanks to those who helped me with various aspects of conducting research and the writing of this thesis. First and foremost, I would like to thank my major advisor professor Chunhui Chen, for his guidance, patience and support throughout this analysis and my post-doc application. I would also like to thank my committee members for their efforts and contributions to this work: professor Soeren Prell, Kerry Whisnant, Kirill Tuchin and Mani Mina.

## ABSTRACT

A search for heavy resonance decaying into a photon and a Higgs boson is performed, where the Higgs boson continually decaying into a pair of  $b$ -quarks. Data was collected from 2015 to 2018 using the ATLAS detector at the LHC at the center-of-mass energy of  $\sqrt{s} = 13$  TeV with an integrated luminosity of  $139 \text{ fb}^{-1}$ . To improve the sensitivity of this analysis, a novel  $H \rightarrow b\bar{b}$  tagger method, Center-of-Mass sub-jet b-tagging algorithm, is implemented to identify the two  $b$ -quarks in a single Large- $R$  jet. There is no obvious deviation from the Standard Model prediction. Upper limit is set using  $CL_s$  strategy at 95% confidence level. Compared with previous ATLAS and CMS result, on top of the statistic gain, more than 30% improvement is observed in the expected upper limit.

## CHAPTER 1. INTRODUCTION

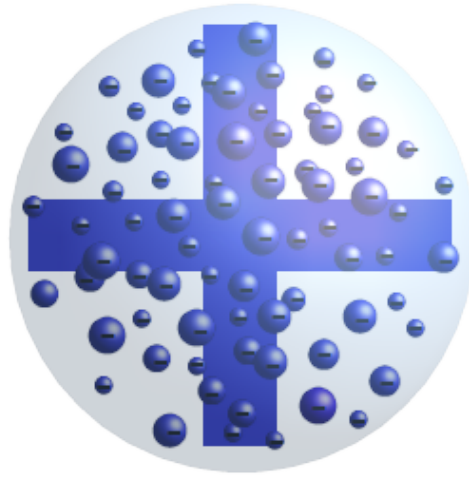
“Who are we?”, “Where did we come from?”, “Where are we going?”, these questions puzzle humans for many years, not just in philosophy, but also in physics. In ancient Greek, people proposed that everything is made with “ATOM”. From Greek, ATOM means uncuttable, which is the most fundamental element, although at that time no one knew what ATOM should be. Hundreds of years ago, John Dalton found an indivisible unit block in the chemistry interaction and called it “atom”. Although later Thomson discovered the electron inside the atom and Rutherford found the nucleus. If we continually cut the nucleus into pieces, we find proton and neutron, and inside proton and neutron, there are quarks. Scientists keep increasing the searching energy and the fundamental unit becomes smaller and smaller. As for high energy physics nowadays, people are trying to find out the most fundamental particles and study the fundamental interaction between these particles. The most successful theory is called the “Standard Model” (SM). However, still there are a few phenomenons that can not be explained by the SM. So theorists build many models beyond the SM, trying to explain those phenomenons. For example, technicolor, little Higgs, or a more complex Higgs sector. All of them predict new massive bosons. Some of these bosons can decay into a Higgs boson plus a photon. My work is to find out these kinds of heavy boson from a Higgs boson plus a photon final state.

## CHAPTER 2. THEORY: STANDARD MODEL

This chapter starts with the history of the discovery of the microscopic particle, and is followed by the introduction of the fundamental particle and the SM.

### 2.1 Historical background of particle discovery

For a long time, humans have been trying to figure out what consists of the universe, and how the matter interacts with each other. Nowadays the most successful theory, which can describe almost all the phenomenons in high energy physics, is called the “Standard Model” (SM). It takes scientists a very long time to build this model. Start from around 2000 years ago, in ancient Greece, Leucippus and his pupil Democritus[1, 2, 3, 4] proposed that the smallest element exists and is called “ATOM”, which means “uncuttable” and is the unit block for building all the matter in the world. In the 19<sup>th</sup> century, chemists found out that “if two elements form more than one compound between them, then the ratios of the masses of the second element which combine with a fixed mass of the first element will always be ratios of small whole numbers.”, stated as Law of multiple proportions. This common pattern, observed by John Dalton[5], suggests that in the chemical interaction, the smallest elements attending the interaction as the basic indivisible unit of mass exists, which is called “atom” by Dalton. Although now it is well known that this “atom” is not really “uncuttable”. Later In 1897, J. J. Thomson[6] discovered the electron in the cathode rays. He found that the charge-to-mass ratio of the particles in the cathode rays is a constant, which doesn’t depend on the cathode material. He called such particles “corpuscles”. Since the discovery of the electron, J. J. Thomson proposed a “Plum pudding model”[7], as shown in Figure 2.2, to explain why the electron is negative but the atom is neutral. In this model, the electrons are surrounded by a volume of positive charge, like negatively-charged “plums” embedded in a positively-charged “pudding”. A few years later, in



(a)

Figure 2.2: Plum pudding model by J. J. Thomson. The electrons are surrounded by a volume of positive charge, like negatively-charged “plums” embedded in a positively-charged “pudding”. [Figure is from wikipedia.](#)

1909, Hans Geiger, Ernest Marsden, and Ernest Rutherford[8] found that this “Plum pudding model” was wrong when they did the gold foil experiment. In the gold foil experiment, they emitted a beam of alpha particles to a very thin gold foil and found that almost all the alpha particles passed the gold foil without much effect, while around 1 of 8000 alpha particles were deflected with very large angles (almost  $180^\circ$ ). This is conflicted with the “Plum pudding model”, in which the alpha particles should not be deflected with a large angle. From this experiment, in 1911, Rutherford proposed a new model, called Rutherford model, as shown in Figure 2.4, suggesting that at the center of the atom, charge and mass are highly concentrated in a small region, which is called “nucleus” of the atom; and the electrons are moving around the nucleus inside the atom. But from classical electromagnetism, an accelerating charged particle will emit electromagnetic waves and lose energy, so that the electron outside the nucleus will continually move close and eventually drop to the nucleus, then there will be no stable atom at all. Two years after the Rutherford model, Niels Bohr[9, 10, 11] came up with a different model that electrons

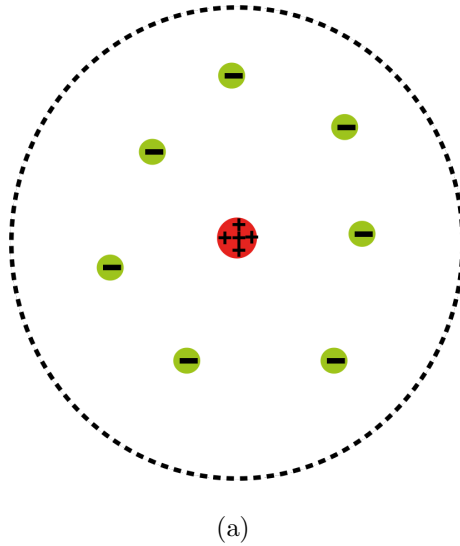


Figure 2.4: Rutherford model by Hans Geiger, Ernest Marsden and Ernest Rutherford. In this model, charge and mass are highly concentrated in a small region at the center of the atom, which is called “nucleus” of the atom. And the nucleus is surrounded by the electron. [Figure is from wikipedia.](#)

are moving around the nucleus in some “stationary orbits”. The electron can jump between different orbit, and electron in different orbit has a different energy. This interesting idea involves the concept of quantum mechanics. Inside the nucleus, proton was found in 1919 by Rutherford[12] in the cloud chamber images, and James Chadwick confirmed the neutron[13]. However, that is not the end of the story, a lot of new particles were discovered later. Antiparticle was proposed by Paul Dirac as a consequence of the Dirac equation[14] and the first antiparticle, positron, was discovered by Carl D. Anderson[15] in a cloud chamber. A few years later, in 1937, a particle similar to the electron, but with a much larger masses,  $\mu$ , called “Muon”, was discovered by Carl D. Anderson and Seth Neddermeyer[16]. Besides, lots of hadrons were found, including Pion ( $\pi$ ), Kaon ( $K$ ),  $\Lambda^0$ , etc. From the discovery of the hadrons, people started to wonder, whether these hadrons were all the fundamental particles or not. In 1964, Gell-Mann[17] and George Zweig[18] found a way to explain these hadrons, the quark model. There are three kinds of quarks, “up”, “down” and “strange”, the combination between two of them or three of

them forms the mesons (two quarks) or baryons (three quarks). Later people discovered another three kinds of quarks: charm quark at the Stanford Linear Accelerator Center[19] and Brookhaven National Laboratory[20] in 1974; bottom(beauty) quark in 1977[21] and top quark in 1995[21] at Fermilab. Totally six kinds of quarks are discovered, which are the fundamental particles that can build hundreds of different hadrons. On the other side, the last charged lepton in SM,  $\tau$ , called “Tau”, was discovered in SLAC[22]. Although we call it “lepton”, actually it is even heavier than up, down and strange quarks. The last piece of Fermion (Fermion will be introduced in Section 2.2.1) in SM is the neutrino. It was theorized by Wolfgang Pauli in a letter to a group of physicists meeting in 1930 to explain the energy conservation in the beta decay, and the first discovered neutrino is the electron-antineutrino  $\bar{\nu}_e$ , in 1956 in the Cowan–Reines neutrino experiment[23]. Later in 1962, muon neutrino  $\nu_\mu$  was found by Leon M. Lederman, Melvin Schwartz and Jack Steinberger[24]. And 20 years ago, in 2000, the last neutrino, tau neutrino  $\nu_\tau$ , was found by DONUT collaboration at Fermilab[25]. Besides Fermion, there is another kind of particle in SM, the Boson (Boson will be introduced in Section 2.2.2). The Bosons are divided into two groups. The first group is Gauge boson (vector boson), including photon, gluon and  $W$  and  $Z$  bosons. Photon is well-known, it is the electromagnetic force carrier. In 1979, gluon was found in PLUTO experiments at Desy[26]. And in 1983,  $W$  and  $Z$  bosons were discovered in UA1 and UA2 in CERN[27, 28, 29]. The second group is Scalar Boson, which only has one member: the Higgs boson. In 2012, ATLAS and CMS announced the discovery of Higgs boson[30, 31].

## 2.2 Fermion and Boson

In SM, there are two different kinds of particles: Fermion and Boson. Figure 2.6<sup>1</sup> shows the summary of all the particles in the SM. The matter consists of the proton, neutron and electron, etc. Proton is made with up and down quark. All these particles belong to Fermion. In SM, there are two different groups of Fermion particles: quark (in purple box in Figure 2.6) and lepton (in green box in Figure 2.6). There are six different quarks and six different leptons. On the right

---

<sup>1</sup>By MissMJ, Cush - Own work by uploader, PBS NOVA, Fermilab, Office of Science, United States Department of Energy, Particle Data Group, Public Domain, <https://commons.wikimedia.org/w/index.php?curid=4286964>

side in Figure 2.6, there are four vector Bosons (in red box): photon,  $W/Z$  and gluon for interaction. And the last one is one special scale Boson, Higgs Boson (in yellow box).

Besides, every particle has its antiparticle with the same mass but opposite charges. For example, the antiparticle for electron is positron. The mass of positron is the same as the mass of electron. However, positron has a charge of  $+e$ , and the electron has a charge of  $-e$ . For some of the particles, their antiparticle are themselves, such as  $Z$  boson, in Section 2.2.2.3, gluon, in Section 2.2.2.2 and photon, in Section 2.2.2.1.

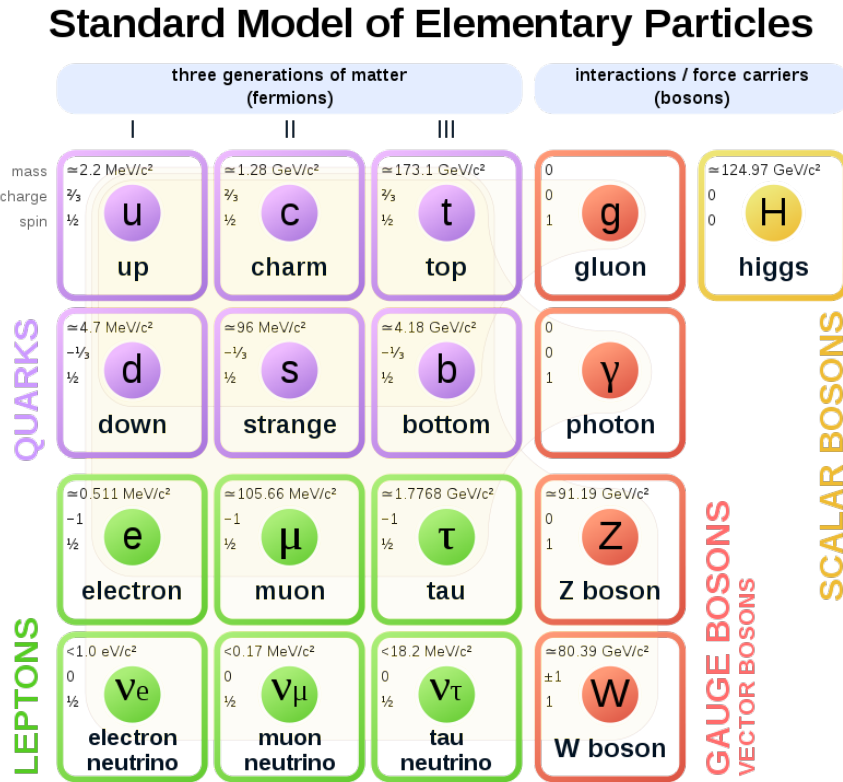


Figure 2.6: Summary of the particles in SM. In general, the fundamental particles are divided into two groups: Fermion (left) and Boson (right). Fermion is the unit to build the matter and Boson is the one propagate interaction



### 2.2.1 Fermion

Fermion, which follows the Fermi–Dirac statistics, has half odd integer spin, such as  $1/2$ ,  $3/2$ , etc. Fermion can be the fundamental particle, for example, electron and quark. Fermion can be the composite particles, too, such as all baryon and some atom. These composite Fermion particles are the important blocks for all the matter, such as proton, neutron, so people usually associate Fermion to matter, and Boson to interaction. In SM, there are two kinds of fundamental Fermion particle, quark and lepton, and both of them have spin  $1/2$ . For the quark and lepton, it is further split into three generations: first generation, including up quark, down quark, electron and electron neutrino  $\nu_e$ ; second generation, including charm quark, strange quark,  $\mu$  and muon neutrino  $\nu_\mu$ ; third generation, including top quark, bottom quark, tau and tau neutrino  $\nu_\tau$ , as shown in Figure 2.6.

#### 2.2.1.1 Quark

There are six different quarks: up ( $u$ ), down ( $d$ ), charm ( $c$ ), strange ( $s$ ), top ( $t$ ) and bottom ( $b$ ). Up, charm and top quarks have  $+2/3$  electric charge ( $+\frac{2}{3}e$ ). Down, strange and bottom quarks have  $-1/3$  electric charge ( $-\frac{1}{3}e$ ). Besides electric charge, every quark also has the color charge, which can be red, blue or green (or the corresponding anti-color, anti-red, anti-blue, anti-green for anti-quark). Because of the color confinement, there is no free isolated quark in nature, all the quarks are found in the hadron, including baryons and mesons. For baryon, it consists of three valence quarks. For example, proton consists of two up and one down quarks, so its net electric charge is 1. As for the color charge, one of the quarks has red charge, one of them has blue charge and the other has green charge, to form a color singlet. The other common baryon is neutron, it is made with two down and one up quarks. So it is electric charge neutral. For meson, it is built with a valence quark-anti-quark pair. For example, a  $\pi^+$  is made with an up and anti-down quark. Depends on the composition of the quarks, the electric charge of meson can be -1, 0 or +1. But their color charges are always neutral, which means it can be only red-anti-red, blue-anti-blue or green-anti-green pairs.

### 2.2.1.2 Lepton

There are two types of leptons. The first group is charged lepton, including electron  $e$ , muon  $\mu$  and tau  $\tau$ . Electron is the first lepton been observed, which is surrounding the nucleus inside the atom. Muon and tau are similar to electron, but with a much larger masses. The mass of  $e$  is 0.5 MeV, the mass of  $\mu$  is 106 MeV and the mass of  $\tau$  is 1.7 GeV, which is even heavier than up and down quarks. Since  $e$  is the lightest charged lepton, it is stable. While  $\mu$  is heavier, it is possible for  $\mu$  to decay, and its lifetime is  $2.2 \times 10^{-6}s$ . Tau is even heavier, its lifetime is much shorter, only  $2.9 \times 10^{-13}s$ . Although the lifetime of  $\mu$  is short, it is still long enough to be observed in the particle detector, like ATLAS and CMS. However, the lifetime for  $\tau$  is too small, the  $\tau$  is almost immediately decaying into a neutrino and an off-shell  $W$  boson (will be introduced in Section 2.2.2.3) after  $\tau$  is produced. The other group of lepton is neutrino, including  $\nu_e$ ,  $\nu_\mu$  and  $\nu_\tau$ . Neutrino is charge 0, and thought to be massless initially in the SM. However, recently many experiments, for example, Super-Kamiokande[32] and Sudbury Neutrino Observatory[33] showed that neutrinos have mass. Unlike quark, lepton doesn't have color charge. But if we group  $e$  and  $\nu_e$ ,  $\mu$  and  $\nu_\mu$ ,  $\tau$  and  $\nu_\tau$ , and assign the electronic lepton number for  $e$  and  $\nu_e$  to be +1, assign the muonic lepton number for  $\mu$  and  $\nu_\mu$  to be +1, assign the tauonic lepton number for  $\tau$  and  $\nu_\tau$  to be +1, these three lepton numbers are conserved in the absence of neutrino mass. The conservation of the lepton number in the SM is violated by the neutrino oscillation, which describes the phenomena that neutrinos with one specific type of flavor can spontaneously change to neutrinos with a different flavor. However, such an effect is too small to be observed in experiments.

### 2.2.2 Boson

Boson, which follows the Bose–Einstein statistics, has an integer spin, such as 0, 1, 2, etc. Like Fermion, Boson can be the fundamental particle or composite particles. For the composite particles, for example, all mesons are bosons. In SM, there are four kinds of gauge bosons (vector bosons), including photon, gluon,  $W$  and  $Z$ ; one kind of scale boson, Higgs boson. There are two  $W$  bosons,  $W^+$  and  $W^-$ . For gluon, there are eight gluons, each of them has a different color

charge, which will be introduced in Section 2.2.2.2. For the gauge bosons, they have spin 1, and are the interaction propagator. There are three kinds of interaction in SM: electromagnetic interaction, the corresponding carriers are photons; strong interaction, the corresponding carriers are gluons; weak interaction, the corresponding carriers are  $W/Z$  bosons. For Higgs boson, its spin is zero, and it will interact with all the massive particles.

### 2.2.2.1 Photon

Photon is the force carrier of the electromagnetic interaction, so it only interacts with charged particles, such as the charged lepton and quark, but not the charge-neutral particle, such as the neutrino. In quantum field theory, the relativistic quantum field theory of electrodynamics is called quantum electrodynamics (QED). The photon itself is charge neutral, so it won't interact with itself. The mass of photon is zero, so it is stable and won't decay to other particles, and the electromagnetic interaction is a long-range interaction, the potential field is proportional to  $1/r$ . In Lagrange, the interaction between the electromagnetic field and charge Fermion, for example, quark, is:

$$\mathcal{L}_{QED} = \bar{\psi}(i\gamma^\mu \mathcal{D}_\mu - m)\psi - \frac{1}{4}F_{\mu\nu}F^{\mu\nu} \quad (2.1)$$

Here  $\mathcal{D}_\mu$  is the gauge-covariant derivative:  $\mathcal{D}_\mu \equiv \partial_\mu + ieA_\mu$ .  $A_\mu$  is the electromagnetic field,  $F_{\mu\nu} = \partial_\mu A_\nu - \partial_\nu A_\mu$  is the electromagnetic field strength tensor.  $e$  is the electron charge.  $\psi$  is the Fermion field,  $\bar{\psi}$  is called “Dirac adjoint”, defined as:

$$\bar{\psi} \equiv \psi^\dagger \gamma^0 \quad (2.2)$$

where  $\gamma^{\mu\nu}$  is called “Dirac matrices” or gamma matrices, which satisfy:

$$\{\gamma^\mu, \gamma^\nu\} = \gamma^\mu \gamma^\nu + \gamma^\nu \gamma^\mu = 2g^{\mu\nu} \quad (2.3)$$

with:

$$g^{\mu\nu} = \begin{bmatrix} 1 & 0 & 0 & 0 \\ 0 & -1 & 0 & 0 \\ 0 & 0 & -1 & 0 \\ 0 & 0 & 0 & -1 \end{bmatrix} \quad (2.4)$$

Here  $g^{\mu\nu}$  is the “Metric tensor” for flat time-space. A common choice for the gamma matrix is:

$$\begin{aligned} \gamma^0 &= \begin{pmatrix} 1 & 0 & 0 & 0 \\ 0 & 1 & 0 & 0 \\ 0 & 0 & -1 & 0 \\ 0 & 0 & 0 & -1 \end{pmatrix}, & \gamma^1 &= \begin{pmatrix} 0 & 0 & 0 & 1 \\ 0 & 0 & 1 & 0 \\ 0 & -1 & 0 & 0 \\ -1 & 0 & 0 & 0 \end{pmatrix}, \\ \gamma^2 &= \begin{pmatrix} 0 & 0 & 0 & -i \\ 0 & 0 & i & 0 \\ 0 & i & 0 & 0 \\ -i & 0 & 0 & 0 \end{pmatrix}, & \gamma^3 &= \begin{pmatrix} 0 & 0 & 1 & 0 \\ 0 & 0 & 0 & -1 \\ -1 & 0 & 0 & 0 \\ 0 & 1 & 0 & 0 \end{pmatrix} \end{aligned} \quad (2.5)$$

Figure 2.8 is an example of the QED Feynman diagram, the tree-level electron-positron interaction. The solid line represents the electron, the wavy line is for a photon. The electron can annihilate with the positron and produce a photon decaying back into electron and positron in Figure 2.8(a) or the electron interacts with positron through the photon Figure 2.8(b).

### 2.2.2.2 Gluon

Gluon is the strong interaction force carrier, it only interacts with particles which have the color charge. The theory of strong interaction is called quantum chromodynamics (QCD). Different from the photon, gluon itself has a color charge, so it can interact with itself, and change the color charge of the particles. Each gluon has one color charge and one anticolor charge. So there are 9 possible combinations:

$$r\bar{r}, r\bar{b}, r\bar{g}, b\bar{r}, b\bar{b}, b\bar{g}, g\bar{r}, g\bar{b}, g\bar{g} \quad (2.6)$$

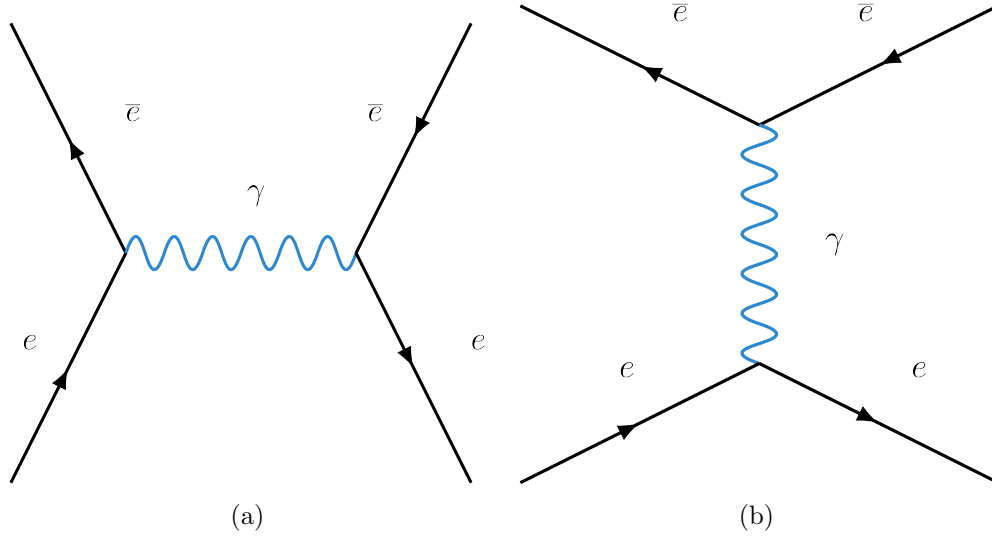


Figure 2.8: Feynman diagram for the tree-level QED interaction between electron and positron. (a): electron positron annihilation; (b) electron interacts with positron with photon as propagator.

This is possible in theory, but in the real world, the strong interaction is a short-range interaction. The color confinement requires that all the free particles are color singlet. And since gluon is massless, if the color singlet gluon exists,  $(r\bar{r} + b\bar{b} + g\bar{g})/\sqrt{3}$ , then this color single gluon can be free and the strong interaction become a long-range interaction. So there is no singlet gluon, and there are only eight different charge combination, a common choice is:

$$\begin{aligned}
 |1\rangle &= (r\bar{b} + b\bar{r})/\sqrt{2} & |5\rangle &= -i(r\bar{g} - g\bar{r})/\sqrt{2} \\
 |2\rangle &= -i(r\bar{b} - b\bar{r})/\sqrt{2} & |6\rangle &= (b\bar{g} + g\bar{b})/\sqrt{2} \\
 |3\rangle &= (r\bar{r} - b\bar{b})/\sqrt{2} & |7\rangle &= -i(b\bar{g} - g\bar{b})/\sqrt{2} \\
 |4\rangle &= \{r\bar{g} + g\bar{r}\}/\sqrt{2} & |8\rangle &= (r\bar{r} + b\bar{b} - 2g\bar{g})/\sqrt{6}
 \end{aligned} \tag{2.7}$$

For a color singlet particle, for example, a meson, the strong interaction between the quark-anti-quark pair is attractive, and it will become stronger if the distance between the quark-anti-quark is larger, until the energy is large enough to produce extra quark-anti-quark pair, then the connection between the origin quark-anti-quark will be broken and two quark-anti-quark pairs will be produced. This will avoid the production of color charged particle.

On the other hand, the strong interaction between two quark is repulsive, since there is no way to combine to quark and make a color singlet particle. The Lagrange for QCD is:

$$L_{QCD} = \bar{\psi}(i\gamma^\mu \mathcal{D}_\mu - m)\psi - \frac{1}{4}G_{\mu\nu}G^{\mu\nu} \quad (2.8)$$

$\mathcal{D}_\mu$  is similar as the one for QED:  $D_\mu \equiv \partial_\mu + ieB_\mu$ , here  $B_\mu$  is the Gauge field:

$B_\mu = \frac{1}{2}\lambda \cdot \mathbf{b}_\mu = \frac{1}{2}\lambda^l b_\mu^l$  and  $b_\mu^l$  is the gluon field. Since QCD is Non-Abelian theory, compared with QED field strength tensor, there is an extra term for the gluon field strength tensor:

$G_{\mu\nu}^l = \partial_\nu b_\mu^l - \partial_\mu b_\nu^l + gf^{jkl}b_\mu^j b_\nu^k$ . Due to this extra term, the gluon field can interact with itself.

Figure 2.10 is an example for the QCD Feynman diagram, the tree-level quark-anti-quark interaction. The solid line represents the quark, the curled line is for gluon. The quark interacts with anti-quark through the gluon in Figure 2.10(a) or the quark is annihilated with the anti-quark and produce a gluon.

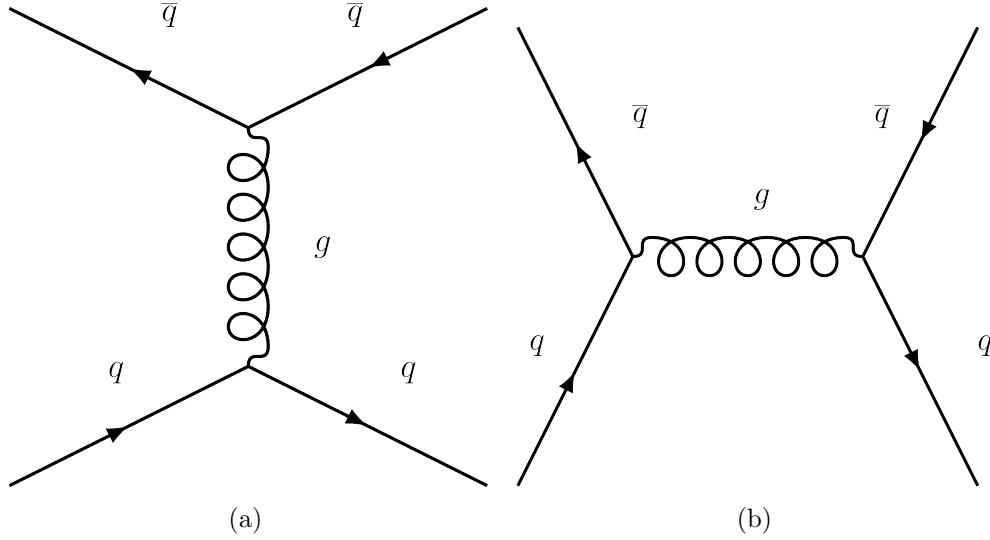


Figure 2.10: Feynman diagram for the tree-level QCD interaction between quark and anti-quark. (a): quark interacts with anti-quark with gluon as propagator; (b) quark anti-quark annihilation.

### 2.2.2.3 $W$ and $Z$ boson

$W$  and  $Z$  bosons are the weak force carriers. Different from QED and QCD,  $W$  and  $Z$  bosons are massive, and  $W$  has the electric charge,  $Z$  is charge 0. Weak interaction is the only interaction which can change the flavor of the quarks, for example, top quark decays into bottom quark and  $W$ :  $t \rightarrow b + W^+$ . It is the only interaction that violates the parity and charge-parity symmetry. The lifetime for  $W$  and  $Z$  is very short, about  $10^{-24}$ s. The charge for weak interaction is called weak isospin. The left-hand component of all the fundamental Fermion has either  $+1/2$  or  $-1/2$  isospin charge, while the right-hand component is zero. So all the fermions can have weak interaction. Similar to the strong interaction,  $W$  and  $Z$  can interact with themselves. Figure 2.12 is an example of the Feynman diagram for the tree-level weak interaction between. (a) electron positron annihilation; (b) electron and electron neutrino scattering through an exchange of a  $W$  boson.

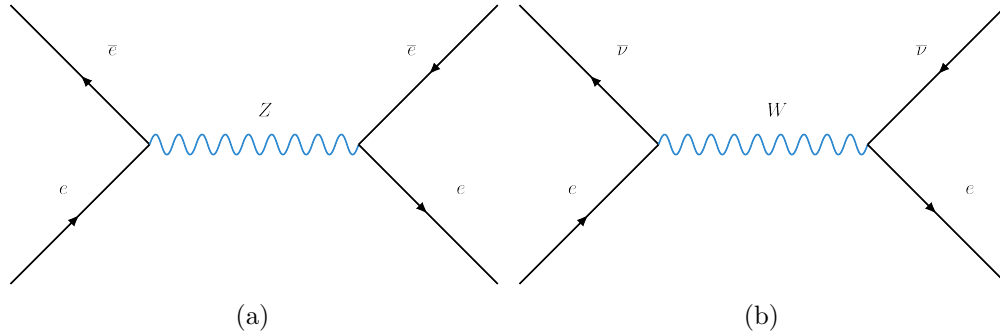


Figure 2.12: Feynman diagram for the tree-level weak interaction between. (a): electron positron annihilation; (b) electron interacts with electron neutrino and generate the  $W$  boson.

### 2.2.2.4 Higgs boson

Higgs boson is a special one, it interacts with all the massive particles, and give the inertial mass to the particles. It is a fundamental scalar (spin 0) boson, name after Peter Higgs, also called

“God particle” by the media. The Higgs boson was proposed to solve the problem of the mass of gauge bosons, which will be introduced in Section 2.3.2.

## 2.3 Standard model

The SM is a gauge-invariant theory 2.3.1, it describes the three fundamental interactions, electromagnetic interaction, weak interaction and strong interaction, between the fundamental particles. All these three interactions are explained as the gauge fields. The gauge theory requires that the mass terms for the gauge field should be zero, in order to maintain the gauge symmetry. To explain the massive gauge particle,  $W$  and  $Z$ , the spontaneous symmetry breaking and Higgs mechanism will be introduced in Section 2.3.2.

### 2.3.1 Gauge theory

Start from classical relativistic field theory, the Lagrange for the scale field, spinor (spin 1/2) field and a vector (spin 1) field is:

$$\mathcal{L}_{scalar} = \frac{1}{2}(\partial_\mu \phi)(\partial^\mu \phi) - \frac{1}{2}(m^2)\phi^2 \quad (2.9)$$

$$\mathcal{L}_{spinor} = i\bar{\psi}\gamma^\mu \partial_\mu \psi - m\bar{\psi}\psi \quad (2.10)$$

$$\mathcal{L}_{vector} = -\frac{1}{16\pi}F^{\mu\nu}F_{\mu\nu} + \frac{m^2}{8\pi}A_\nu A^\nu \quad (2.11)$$

Where  $\phi$  is the scalar field,  $\psi$  is the spinor field,  $A$  is the scalar field and  $F^{\mu\nu} = \partial^\mu A^\nu - \partial^\nu A^\mu$  is called field strength tensor. Gauge theory is a theory that the Lagrange is unchanged under the local phase transformation. For SM, it is unchanged under  $SU(3) \times SU(2) \times U(1)$  symmetry. Here  $SU(3)$  symmetry corresponds to the strong interaction,  $SU(2) \times U(1)$  corresponds to electroweak interaction. For the gauge theory, let's consider the Lagrange for the spinor field as an example:

$$\mathcal{L}_{spinor} = i\bar{\psi}\gamma^\mu \partial_\mu \psi - m\bar{\psi}\psi \quad (2.12)$$

This Lagrange is invariant under a global phase transformation:  $\psi \rightarrow e^{i\theta}\psi$ . The gauge theory requires that the Lagrange is invariant under not only global phase transformation, but also local



phase transformation:  $\psi \rightarrow e^{i\theta(x)}\psi$ , here  $\theta(x)$  is a function of space-time. However, free Lagrange is not local phase invariant, there is one additional term when doing the local phase transformation:  $\mathcal{L} \rightarrow \mathcal{L} - \partial_\mu \theta \bar{\psi} \gamma^\mu \psi$ , we need to add a coupling term between the spinor field and vector field to cancel it:

$$\mathcal{L} = i\bar{\psi}\gamma^\mu\partial_\mu\psi - m\bar{\psi}\psi - q\bar{\psi}\gamma^\mu\psi A_\nu \quad (2.13)$$

Here  $A_\nu$  is a new vector field, and under the local phase transformation:  $A_\mu \rightarrow A_\mu - \frac{1}{q}\partial_\mu\theta$ . We call this vector field “gauge field”, and the transformation is called “gauge transformation”.  $q$  is the interaction coupling constant. The last part is to add the kinematic term for this gauge field into Lagrange, and notice that for the kinematic term of a gauge(vector) field,  $F^{\mu\nu}F_{\mu\nu}$  is gauge invariant, but  $\frac{m^2}{8\pi}A_\nu A^\nu$  is not invariant, which means the parameter  $m$ , which is the mass of the vector field, should be zero. So the final Lagrange becomes:

$$\mathcal{L} = i\bar{\psi}\gamma^\mu\partial_\mu\psi - m\bar{\psi}\psi - q\bar{\psi}\gamma^\mu\psi A_\nu - \frac{1}{16\pi}F^{\mu\nu}F_{\mu\nu} \quad (2.14)$$

Here the “covariant derivation”:  $\mathcal{D}_\mu \equiv \partial_\mu + iA_\nu$ , and the Lagrange become:

$$\mathcal{L} = i\bar{\psi}\gamma^\mu\mathcal{D}_\mu\psi - m\bar{\psi}\psi - \frac{1}{16\pi}F^{\mu\nu}F_{\mu\nu} \quad (2.15)$$

Now both the whole Lagrange and each term in the Lagrange are gauge invariant.

### 2.3.2 Spontaneous symmetry breaking and Higgs mechanism

We have a gauge invariant Lagrange now, the spinor field is the Fermion field, which can be electron, muon, quark, etc. For the gauge field, it is a vector field. From the experiment, we know that photon is massless, but  $W$  and  $Z$  boson is massive. So we have to add a mass term in Lagrange, which will violate the gauge invariant at first glance. To consider the mass term, we will need to introduce the spontaneous symmetry breaking and the Higgs mechanism. Let's consider two real scalar field:  $\phi_1$  and  $\phi_2$ , and define the combination:  $\phi = \phi_1 + i\phi_2$ , and the Lagrange for these two fields is:

$$\mathcal{L} = \frac{1}{2}(\partial_\mu\phi)^*(\partial^\mu\phi) + \frac{1}{2}\mu^2(\phi^*\phi) - \frac{1}{4}\lambda^2(\phi^*\phi)^2 \quad (2.16)$$

Here the  $\frac{1}{2}\mu^2(\phi^*\phi) - \frac{1}{4}\lambda^2(\phi^*\phi)^2$  is the potential term. To satisfy the gauge invariant, we add the gauge field and the interaction term into the Lagrange:

$$\mathcal{L} = \frac{1}{2}(\mathcal{D}_\mu\phi)^*(\mathcal{D}^\mu\phi) + \frac{1}{2}\mu^2(\phi^*\phi) - \frac{1}{4}\lambda^2(\phi^*\phi)^2 - \frac{1}{16\pi}F^{\mu\nu}F_{\mu\nu} \quad (2.17)$$

From the potential term, the minimum value of the potential is at  $\phi_1^2 + \phi_2^2 = \frac{\mu^2}{\lambda^2}$ . Since the gauge symmetry, it is free to choose any gauge. We can choose such gauge that  $\phi$  becomes a real field.

And then we replace  $\phi$  with another field which has a minimum at 0:  $\eta = \phi - \frac{\mu}{\lambda}$ , then the

Lagrange will become:

$$\begin{aligned} \mathcal{L} = & \left[ \frac{1}{2}(\partial_\mu\eta)(\partial^\mu\eta) - \mu^2\eta^2 \right] + \left[ -\frac{1}{16\pi}F^{\mu\nu}F_{\mu\nu} + \frac{1}{2}\left(\frac{q}{\hbar c}\frac{\mu}{\lambda}\right)^2 A_\mu A^\mu \right] \\ & + \left\{ \frac{\mu}{\lambda}\left(\frac{q}{\hbar c}\right)^2 \eta(A_\mu A^\mu) + \frac{1}{2}\left(\frac{q}{\hbar c}\right)^2 \eta^2(A_\mu A^{jt}) - \lambda\mu n^3 - \frac{1}{4}\lambda^2\eta^4 \right\} \\ & + \left(\frac{\mu^2}{2\lambda}\right)^2 \end{aligned} \quad (2.18)$$

And now there is a mass term for the gauge field:  $\frac{1}{2}\left(\frac{q}{\hbar c}\frac{\mu}{\lambda}\right)^2 A_\mu A^\mu$ , and the mass for the gauge field is:  $m_A = 2\sqrt{\pi}\left(\frac{q\mu}{\lambda}\right)$ . And notice that now the  $\eta$  has self-interaction term:  $-\lambda\mu n^3 - \frac{1}{4}\lambda^2\eta^4$ . As for the mass of Fermion, it is from the Yukawa term:  $\mathcal{L}_{Yukawa} = -G_e[\bar{R}(\phi^\dagger L) + (\bar{L}\phi R)]$ ,  $L$  is the left-hand component of the “weak-isospin” doublet, take electron and electron neutrino as an example:

$$L = \begin{pmatrix} \nu \\ e \end{pmatrix}_L, \quad (2.19)$$

here  $\nu_L = \frac{1}{2}(1 - \gamma_5)\nu$ , which is the left-hand component of the electron neutrino field,

$e_L = \frac{1}{2}(1 - \gamma_5)e$  is the left-hand component of the electron field, while  $R = e_R = \frac{1}{2}(1 + \gamma_5)e$  is the right-hand component of the electron field, the right-hand component of electron neutrino is zero, and  $\phi$  is the scalar field:

$$\phi = \begin{pmatrix} \phi^1 \\ \phi^2 \end{pmatrix}, \quad (2.20)$$

Now if we add the same potential term for the scalar field, and expand the scalar field at one of the minimum point of the potential:

$$\langle\phi\rangle_0 = \begin{pmatrix} 0 \\ \frac{\mu}{\lambda} \end{pmatrix}, \quad (2.21)$$

and absorb three degrees of freedom of the scalar field into the gauge, then we have:

$$\phi = \begin{pmatrix} 0 \\ h + \frac{\mu}{\lambda} \end{pmatrix}, \quad (2.22)$$

Here  $h$  is the Higgs boson field, and the Yukawa term becomes:  $\mathcal{L}_{\text{YuKawa}} = -G_e[\frac{\mu}{\lambda}\bar{e}e + h\bar{e}e]$ . The mass of electron becomes:  $\frac{\mu}{\lambda}$ , and the Higgs boson field is coupling with the electron field, but not the electron neutrino field. It is slightly different for the Yukawa term between quark and lepton. For lepton, the neutrino only has left-hand component, while for quark, all of the six quarks have both left hand and right-hand components.

### 2.3.3 Beyond Standard model

The SM is a very successful theory, especially with the prediction of the Higgs boson which is discovered in 2012, it can explain most of the phenomenon from many different experiments. However, it is not the final theory for everything, many open questions need the theory beyond SM, or the extension of the SM. For example, there are four fundamental interactions, electromagnetic interaction, weak interaction, strong interaction and Gravity. But the SM only includes the first three of them. In the classical SM, neutrino doesn't have mass, while the neutrino oscillations[32, 33] imply a very small mass for neutrino. Although the SM can explain the mass of neutrino with the extension including the Seesaw Mechanism [34], it is not clear why the mass of neutrino is so small, and why the gap in mass between different particles are such huge. Other puzzles are from Astronomy, dark matter and dark energy. It is found that only about 5 % of the matter-energy is from the SM particles, for example, the Astronomical objects including stars, asteroids, comets and debris, etc. However, these objects are not enough to explain many phenomena, for example, the abnormal angular speed of many galaxies. So the dark matter[35], which is hardly interacted with the electromagnetic field (that is why it is called "Dark"), is proposed. And it consists of 27 % of the matter-energy of the universe. There are many observation evidence for the dark matter, such as the galaxy rotation curves [36] and Gravitational lensing [37]. On the other thing, the universe is expanding not at a constant speed,

but the expansion is accelerating [38]. There is no way to explain this acceleration from the SM particles. A possibly and generally accepted explanation is the dark energy, which is not included in the SM. Over the universe, dark energy contributes around 68 % of the total energy, 27 % of the universe is from dark matter and only around 5 % of the ordinary matter. As for the ordinary matter, we don't understand why there is more matter than antimatter in the universe. So we only know a very tiny fraction of the universe.

## CHAPTER 3. PARTICLE DETECTOR

In this chapter, a brief introduction about CERN and LHC will be presented first, following by the introduction of ATLAS and each part of the ATLAS detector. Afterwards, some basic concepts about the detector and physics objects reconstruction are introduced.

### 3.1 CERN and LHC

The European Organization for Nuclear Research, also known as [CERN](#), began in 1954. The goal of CERN is to study the fundamental physics, using the particle detector. Since the birth of CERN, many detector and accelerator were built:

- 1: The first accelerator: “the Synchrocyclotron”, started in 1957;
- 2: The Proton Synchrotron, started in 1959;
- 3: Intersecting Storage Rings, ran from 1971, recorded the world’s first interaction from colliding proton;
- 4: Super Proton Synchrotron, started in 1976, the first underground ring of CERN, discovered the  $W$  and  $Z$  boson;
- 5: Large Electron–Positron collider(LEP), first injection in 1989, the most powerful accelerator of the lepton;
- 6: Large Hadron Collider(LHC), the highest energy particle collider ever built, using the same tunnel of LEP after LEP retired.

The LHC is the largest particle collider with the highest energy in the world. It has a huge ring with a 27 km circumference that is 175 meters underground. The LHC was built from 1998 to 2008. Figure [3.2](#) shows the overall view of the LHC[\[39\]](#).

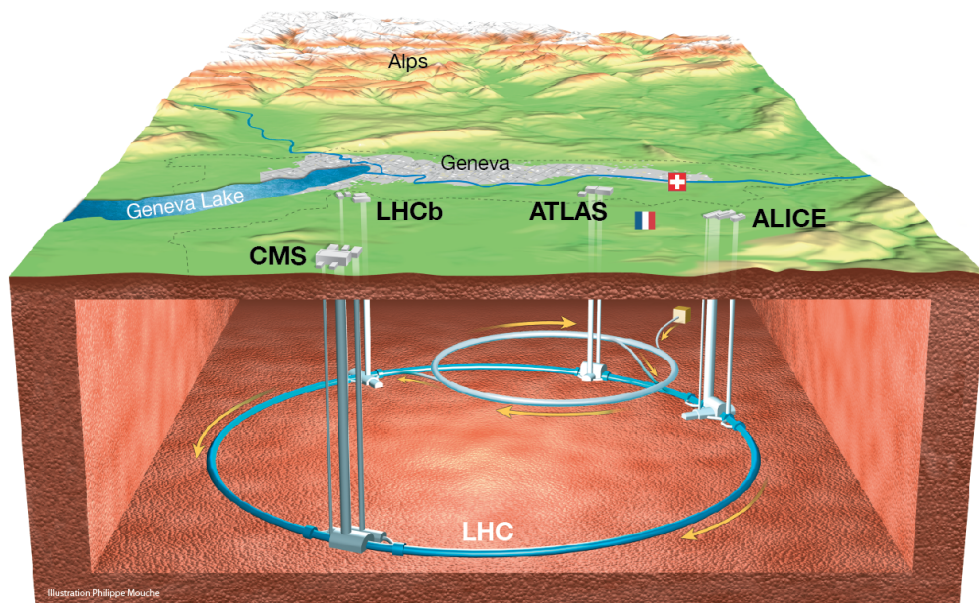


Figure 3.2: Overall view of the LHC. There are four main detectors: ATLAS, CMS, ALICE and LHCb.

The first data taking (run) was from 2009 to 2013 at the center-of-mass (c.m.) energy of 7 TeV from 2009 to 2012, and was later upgraded to 8 TeV in 2012. After the first run, it was shut down for two years for the upgrade, to raise the c.m. energy to 13 TeV. Later it started the second run from 2015 to 2018, with a much higher c.m. energy, 13 TeV. Start from the end of 2018, it is now the second long shutdown, to prepare the upgrade for run 3, which is planned to start in 2021. At the LHC, there are four major detectors: ATLAS, CMS, ALICE and LHCb. ATLAS and CMS are “general-purpose” detectors, they are designed to search for Higgs boson and new physics evidence. In the running year, usually there are around 7 months for proton-proton collision, and around one month for ion collision. The data used in this thesis is from the proton-proton collision from 2015 to 2018, during the run 2 period, with a total luminosity of  $139 \text{ fb}^{-1}$ .

## 3.2 ATLAS detector

ATLAS [40, 41] is the “A Toroidal LHC ApparatuS”. It is one of the main detectors at the LHC, located in the south-west of Geneva, closed to the main CERN office area. Figure 3.4 shows the whole ATLAS detector[42].

It is a general-propose particle detector, including five sub-detectors: inner detector, electromagnetic (EM) calorimeter, hadronic calorimeter, muon spectrometer and forward detectors, to measure the momentum and energy of the outgoing particle.

### 3.2.1 ATLAS coordinate

The ATLAS experiment uses a right-handed coordinate system with its origin at the nominal interaction point (IP) in the center of the detector and the  $z$ -axis along the beam pipe. The  $x$ -axis points from the IP to the center of the LHC ring, and the  $y$ -axis points upward. Cylindrical coordinates  $(r, \phi)$  are used in the transverse plane,  $\phi$  being the azimuthal angle around the  $z$ -axis. The pseudorapidity is defined in terms of the polar angle  $\theta$  as  $\eta = -\ln \tan(\theta/2)$ . Figure 3.6[43] and Figure 3.8 shows the ATLAS coordinate system. The transverse momentum is defined as the momentum component of momentum in the transverse plane (X-Y plane).

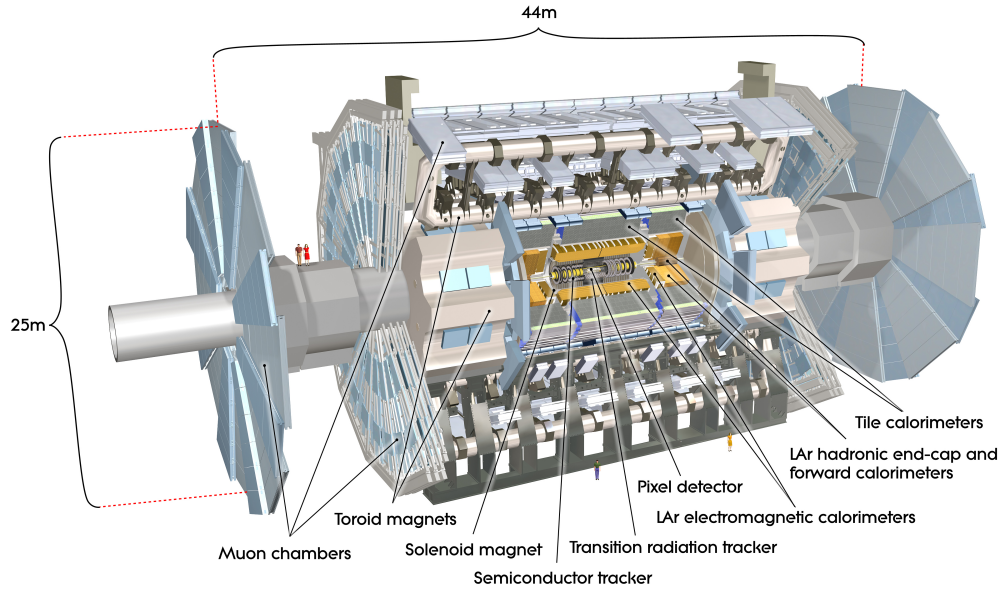


Figure 3.4: Overall view of ATLAS detector. It includes the inner detector, EM calorimeter, Hadronic calorimeter, muon spectrometer and forward detectors.

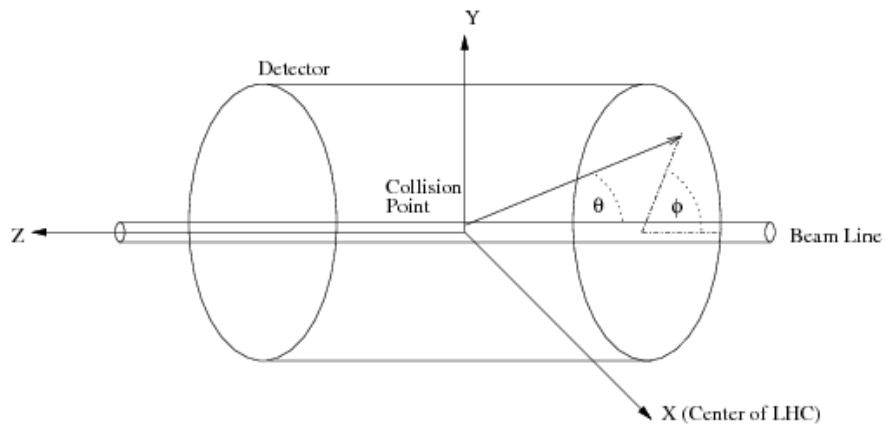


Figure 3.6: ATLAS coordinate system



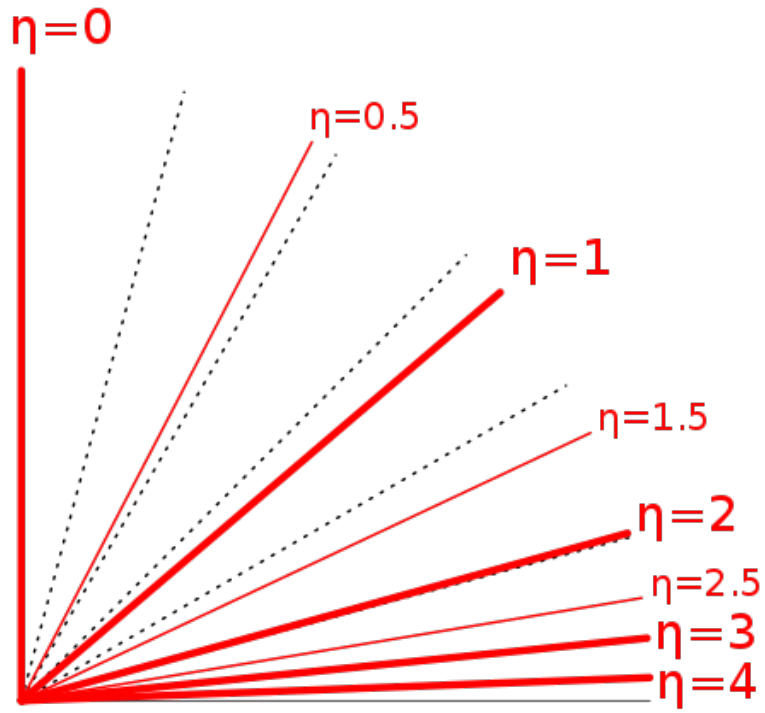


Figure 3.8: Example of pseudorapidity value in the X-Z plane. The angle separation between two dashed lines are  $15^\circ$

### 3.2.2 Inner detector

In ATLAS, during the running time, there will be around 1000 particles generated from the collision points every 25 ns, creating a very dense environment for the measurement. To make a precise measurement for the momentum of the particle and the vertex, the inner detector (ID) is installed to measure the charged particles. Figure 3.10 shows the structure of the whole ID[44].

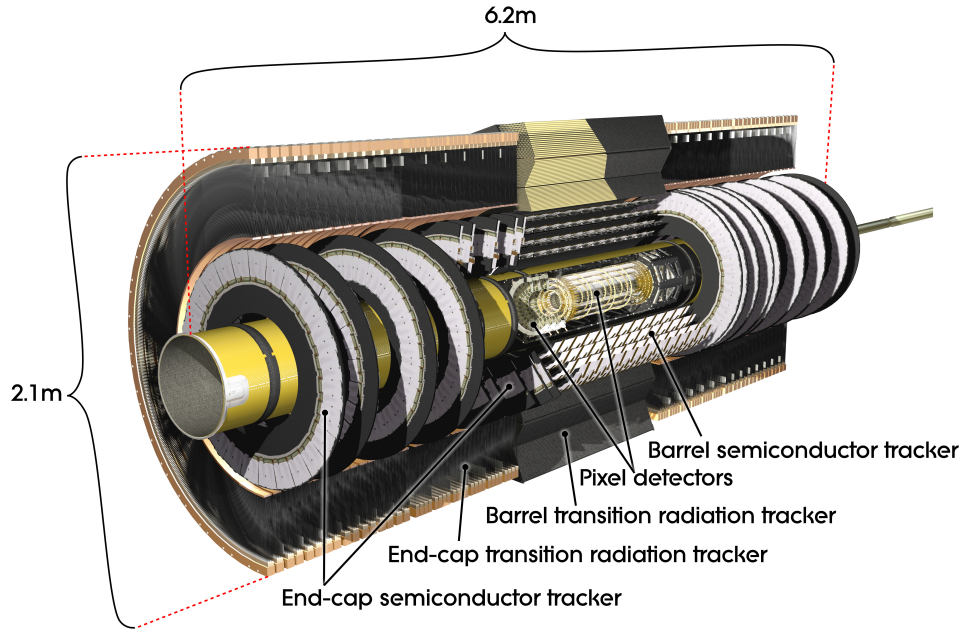


Figure 3.10: The overall view of ID. It consists of three parts: Pixel Detector, Semiconductor Tracker and Transition Radiation Tracker.

The ID is in a 2 T magnetic field environment (parallel to the beam axis), produced by a solenoid aligned on the beam axis surrounding the ID, so that the charged particle will be bent inside the inner detector. When the charged particle passes the inner detector, a “hit” signal will be recorded by the inner detector. Then the ATLAS software will be run to pick the hits from the same particle and connect them to build a “track” for this particle. In the end the momentum of the particle can be calculated from the curvature and the magnetic field. There are three main components of the ID: Pixel Detector, Semiconductor Tracker (SCT), and Transition Radiation

Tracker (TRT), providing the precise measurement of the track in the pseudorapidity range of  $|\eta| < 2.5$ . And for each sub-detector, it is divided into two-part. The central region is called barrel, and the forward region is called endcap. Pixel Detector is the most inner part of the ID. It provides the precisest measurement of the hit position of the track, the pixel size is  $50 \times 400\mu m$ , and its resolution is  $10 \times 115\mu m$ . SCT is outside the pixel detector, with a resolution of  $17 \times 580\mu m$ . The outermost is TRT, providing a large number of hits (typically 30 per track), with intrinsic accuracy of  $130\mu m$ .

### 3.2.3 EM calorimeter

EM calorimeter is ideally suited to measure the energy of electron and photon and stop or absorb them since they will interact with the matter. It is a lead-liquid argon(LAr) detector with accordion-shaped kapton electrodes and lead absorber plates over its full coverage. It consists of **two parts**: barrel covers the pseudorapidity range of  $|\eta| < 1.475$  and two endcap components for  $1.375 < |\eta| < 3.2$ . To fully stop the particles, the total thickness of the barrel part is around 9.7 interaction length( $\lambda$ ) and for the endcap it is  $10\lambda$ [40]. For the barrel, it is 6.4m long and 53cm thick. For the endcap, it is 0.632m thick and its radius is 2,077m. Figure 3.12 shows the computer generated image of both the EM calorimeter and Hadronic calorimeter[45].

### 3.2.4 Hadronic calorimeter

Hadron calorimeter can measure the energy of hadrons(for example, proton and neutron). There are three parts of Hadron calorimeter, Tile calorimeter, The Hadronic End-cap Calorimeter (HEC) and Forward Calorimeter (FCal), as shown in Figure 3.12. The Tile calorimeter is just outside the barrel EM calorimeter, and it is further divided into barrel, covering  $|\eta| < 1$  and extended barrel for  $0.8 < |\eta| < 1.7$ . The barrel and extended barrel are using steel as the absorber and scintillating tiles as the active material. The total thickness of the barrel calorimeter is around 2m and it is 7.4 interaction length. For HEC, it consists of two independent wheels on each side, outside the EM endcap calorimeter. It covers  $1.375 < |\eta| < 3.2$ , using copper plates as

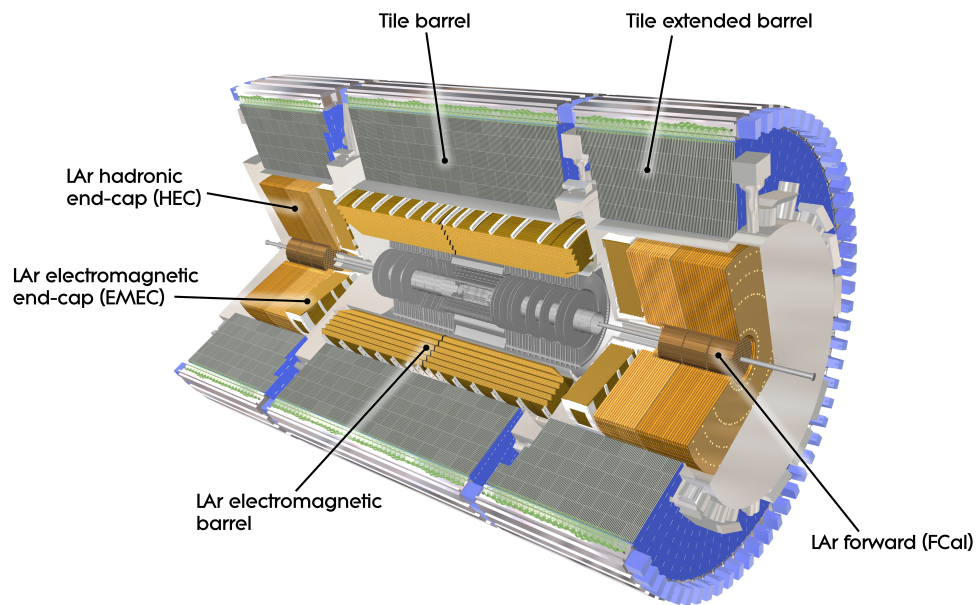


Figure 3.12: The overall view of EM calorimeter and Hadronic calorimeter.

absorber, interleaved with LAr gaps, which provides the active material. The FCal is about 10 interaction length, covers  $3.1 < |\eta| < 4.9$ . It consists of three model: the first one is made of copper, for electromagnetic measurements, and the other two are made of tungsten, for the hadronic interactions.

### 3.2.5 Muon detector

The muon spectrometer is the most outside part of ATLAS detector and is built for muon detection. Figure 3.14 shows the overall view of the muon system. Similar to the inner detector,

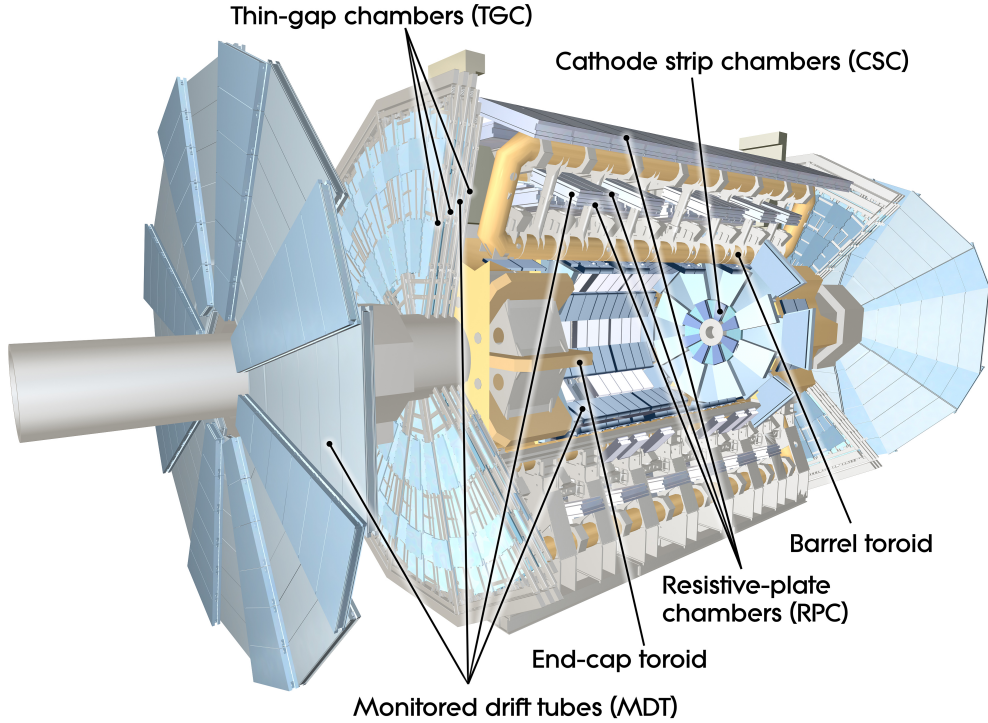


Figure 3.14: The overall view of muon system. There are four subsections of the muon system: Thin Gap Chambers, Resistive Plate Chambers, Monitored Drift Tubes, and Cathode Strip Chambers.

the magnetic field is produced by the large superconducting air-core toroid magnets to bend the muon track. Different from the inner detector, whose magnetic field is paralleled to the beam axis,

there are eight coils encased in individual racetrack-shaped outside the calorimeter for both barrel and endcap, producing the magnetic field in  $\phi$  direction, perpendicular to the beam axis. There are four chambers for the [muon detector](#), Monitored Drift Tubes (MDT), Cathode Strip Chambers (CSC), Resistive Plate Chambers(RPC) and Thin Gap Chambers (TGC). MDT and CSC provide precise measurement of the track coordinates in the bending direction, while MDT covers  $|\eta| < 2.7$  and CSC covers  $2.0 < |\eta| < 2.7$ . CSC and RPC are for triggering while RPC is for barrel and TGC is for endcap. The trigger chambers, RPC and TGC, serve to provide bunch-crossing identification and well-defined  $p_T$  thresholds, and measure the unbending direction of the track.

### 3.2.6 Forward detectors and luminosity

Luminosity is defined as the number of hard scattering events in one unit time period in one unit area. The forward detectors are built to measure the luminosity during the running period. There are [four sub-detectors of forward detectors](#) in ATLAS: Luminosity measurement using Cerenkov Integrating Detector(LUCID), Zero-Degree Calorimeter(ZDC), ATLAS Forward Proton Detector(AFP) and Absolute Luminosity For ATLAS(ALFA). Figure 3.16 shows the overall view of forward detector.

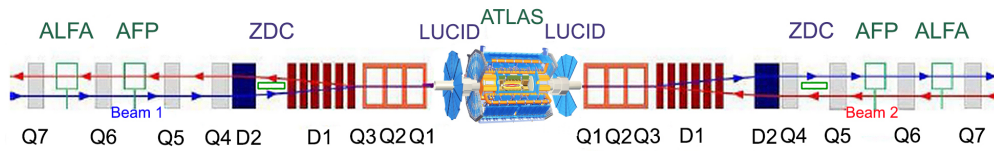


Figure 3.16: The overall view of forward detector. There are four subsections of the forward detector: Luminosity measurement using Cerenkov Integrating Detector, Zero-Degree Calorimeter, ATLAS Forward Proton Detector and Absolute Luminosity For ATLAS.

LUCID is located at  $\pm 17m$  from the interaction point, is the online relative-luminosity monitor for the p-p collision. ZDC is at  $\pm 140m$  from the interaction point to detect forward neutrons in heavy-ion collisions. AFP is for the diffractive protons, and is located at 204m and

217m. ALFA lies at  $\pm 240m$  from the interaction point to measure the absolute luminosity of p-p collision.

### 3.2.7 Trigger, data acquisition

The [trigger system](#) [46] in ATLAS is built to reduce the data rate from 1.7 billion collisions per second to around 1000 events per second. And the data acquisition stores the information from the detectors. For run 2, ATLAS upgrades the trigger system, and there are two parts of the trigger: a hardware-based first level trigger (L1), and a software-based high level trigger (HLT). The L1 trigger takes the subset of calorimeter and muon detector information as input to determine whether to keep the events. It makes the decision whether to keep this event in less than  $2.5\mu s$ , reduces the bunch crossing rate to around 100 kHz. After the L1 trigger, the events are passed to HLT. HLT will use the full information of the detector, including inner detector, to construct the physics object, including electron, photon, muon, tau, Jet(next section), missing transverse energy and b-jet. The thresholds for different objects are determined to satisfy the analysis requirement and reduce the rate to about 1kHz in  $200ms$ .

### 3.2.8 Underlying Events and pile-up

Except for the hard scattering between the proton, event which is not coming from the primary hard scattering is called underlying events[47]. There are several different sources for the underlying events, including the multiple parton interactions, the interactions between the “remnants” of the protons, like the valence quarks and any partners of sea quarks.

In ATLAS, a bunch of protons will collide with another bunch of protons at the center of the detector. In one bunch, it is possible that more than one proton hit the proton from another bunch, this average number of particle interactions per bunch-crossing is called pile-up. There are two kinds of pile-up, In-time pile-up and Out-of-time pile-up. For in-time pile-up, the collisions happen in the same bunch-crossing as the hard scattering. The Out-of-time pile-up is the interaction between the proton and the other one before or after the hard scattering bunch.

### 3.3 Object reconstruction

From the detector output, what we directly observe are the electrical signals, which are from the interaction between the detector material and the outgoing particle. We need to reconstruct the physics object, for example, the photon and muon, from these electrical signals, so that we can use this information for the physics analysis. This chapter will introduce the reconstruction for different physics objects. An overall summary: with the inner detector, we can reconstruct the track for the charged particles to get the momentum information; with the EM and the Hadron calorimeter we can reconstruct the energy for electron, photon and hadron; with the muon detector and combined with the inner detector, we can reconstruct the muon track.

#### 3.3.1 Track and primary vertex

The track of the charged particle can be measured in the inner detector. After we get the track of each charged particle, we can reconstruct the primary vertex. The track reconstruction procedure [48] can be divided into three stages:

1. A pre-processing stage. The raw data from pixel and SCT detectors are converted into clusters.
2. A track-finding stage. For the default tracking reconstruction, first track seeds will be formed from the pixel layers and first SCT layer, then extend to SCT to form the track candidates. Then these track candidates are fitted, rejecting the fake tracks, solving the cluster-to-track ambiguities. After the selection, the track is extended to TRT and finally refitted again with all the information of these three detectors. There is another track-finding strategy, which forms the track seeds in TRT instead of pixel, since the distance between the hits in the out-layer is much larger than the inner layer, so that it can make it easier to pick the seeds.
3. A post-processing stage. The vertex finder is used to reconstruct the primary vertex with all the track information.



### 3.3.2 Electron and photon

For standard electron and photon reconstruction [49], first in the EM calorimeter, a seed cluster is reconstructed and it search for a loosely matching track from all the reconstructed track. In the inner detector, the photon can decay into two electrons, at a rate of about 10 % to 50 %, depending on the  $\eta$ . And this track from the photon decay is called photon conversion track. So if the cluster is associated to a track but not a photon conversion track, then this cluster is identified as an electron, while if the cluster is associated to a photon reconstruction track or no track, then the cluster is identified as a photon.

### 3.3.3 Muon

Since muon is charged particle, it will leave a hit in both the inner detector and also the muon spectrometer. The reconstruction of muon track in the muon spectrometer is similar to the track reconstruction in the inner detector. There are five kinds of muon [50]:

1. Stand-alone muon: muon reconstruction using only the information from muon spectrometer.
2. Combined muon: tracks are reconstructed independently in both inner detector and muon spectrometer, and then a combined fitting using both the track in the inner detector and in the muon spectrometer is performed to reconstruct the muon.
3. Segment tag muon: the track in the inner detector is identified as the muon if the track can extrapolate to the muon spectrometer and associate to at least one local track segment in the MDT or CSC chambers.
4. Calorimeter-tagged muon: the track in the inner detector is identified as the muon if the track can be matched to an energy deposit in the calorimeter compatible with a minimum-ionizing particle.
5. Extrapolated muon: the muon is reconstructed using the track in muon spectrometer and apply a loose requirement on compatibility with originating from the interaction point.

### 3.3.4 Jet

After the proton-proton collision, lots of quarks and gluons will be generated. Since free quark and gluon cannot exist due to the color confinement, they will hadronize to different hadrons immediately after the production. As a result, in the ATLAS detector, we will observe a bunch of collimated particles interact with the calorimeter. Since we are interested in the energy and momentum of the decay product from the hard scattering (for example, a Higgs boson decaying into two  $b$  quarks), we need to collect the information of all these collimated particles and reconstruct a “jet” to represent the initial particle. In ATLAS, primarily the input of the jet reconstruction is topo-clusters and the algorithm is called anti- $kt$  algorithm [51]. The topo-cluster is a group of calorimeter cells whose energy is higher than a certain threshold, to compress the noise (from pile-up and electronics). After we get the topo-cluster, the anti- $kt$  algorithm is applied to these clusters. In the algorithm, it defines the distance between two clusters:

$$d_{ij} = \min(1/p_{ti}^2, 1/p_{tj}^2) \Delta R_{ij}^2 / R^2 \quad (3.1)$$

Here  $1/p_{ti}^2$  and  $1/p_{tj}^2$  are the transverse momenta of  $i^{th}$  and  $j^{th}$  clusters, and  $\Delta R_{ij}^2 = (y_i - y_j)^2 + (\eta_i - \eta_j)^2$  is the angular separation, where  $y_i$  and  $\eta_i$  are the rapidity and azimuth. And it also defines a threshold:  $d_{iB} = \frac{1}{k_{ti}^2}$ . The algorithm calculates the distance between two clusters, and the threshold for each cluster, then it finds out the minimum value for both  $d_{iB}$  and  $d_{ij}$ . If the minimum is one of the  $d_{ij}$ , then these two clusters,  $i^{th}$  and  $j^{th}$ , are combined into one cluster and it will re-calculate  $d_{iB}$  and  $d_{ij}$  these two values. If the minimum is one of the  $d_{iB}$ , then this cluster is dropped and it finds another minimum. At the end it loops over all the clusters and forms a jet. For this analysis, two common jet radius,  $R = 1.0$  and  $R = 0.2$  are mentioned. For  $H \rightarrow b\bar{b}$ , if the momentum of the Higgs boson is large enough, the decay products, two  $b$ -quark, will be collimated and in the detector they are merged with each other and make it very difficult to separate. In this case, we use a larger radius jet, a  $R = 1.0$  anti- $kt$  jet to include all the final product, later use other algorithm to tagger the Higgs boson.

### 3.3.5 Missing $E_T$

ATLAS detector can't detect all kinds of particles, even in the SM, the neutrino hardly interacts with other particles. Those undetectable particles will carry momentum, so that if we know the initial momentum, we will find that the sum of 4-momentum at the final state is not equal to the initial 4-momentum. Since ATLAS is using proton-proton collision, and actually it is the partons that collide with each other, we don't know the exact momentum of the parton. However, in the transverse direction, the momentum of the proton is almost zero, which means the initial transverse momentum is closed to zero. So we can calculate this missing transverse energy by reverse the sum of the transverse energy for all the detectable object [52]:

$$\begin{aligned} E_T^{\text{miss}} &= \sqrt{(E_x^{\text{miss}})^2 + (E_y^{\text{miss}})^2}, \\ E_{x(y)}^{\text{miss}} &= - \left( E_{x(y)}^{\text{jets}} + E_{x(y)}^e + E_{x(y)}^\gamma + E_{x(y)}^\tau + E_{x(y)}^\mu + E_{x(y)}^{\text{ST}} \right) \end{aligned} \quad (3.2)$$

Here  $E_{x(y)}^{\text{jets}}, E_{x(y)}^e, E_{x(y)}^\gamma, E_{x(y)}^\tau$  and  $E_{x(y)}^\mu$  are the sum of x(y)-components of momentum of all the jets, electrons, photons, taus and muons.  $E_{x(y)}^{\text{ST}}$  is the sum of x(y)-components of momentum of all the topo-clusters and tracks which are not associated to the above physics objects.

## CHAPTER 4. PHYSICS ANALYSIS DETAIL

In this chapter the detail of heavy resonance  $Z'$  decaying into a Higgs boson and a photon  $Z' \rightarrow H + \gamma$  analysis strategy will be shown. The analysis is based on the full run 2 data set from 2015 to 2018 at the center of mass energy of 13 TeV by the ATLAS experiment.

### 4.1 Analysis motivation and overview

Many new physics beyond the Standard Model (SM) include predictions of new massive bosons resulting from extension of the Higgs sector or from additional gauge fields, such as technicolor [53], little Higgs [54], or a more complex Higgs sector [55]. Among them, the final state containing the Higgs boson and a photon is interesting where the Higgs boson can be a portal to the new physics beyond the Standard Model. This analysis searches for a massive neutral boson ( $Z'$ ) with a decay final state of a SM Higgs ( $H$ ) boson and a photon ( $\gamma$ ) [56]. In ATLAS, photon can be directly detected with EM calorimeter and inner detector(for photon conversion). However, it is a challenging task to find the Higgs boson in the proton-proton (pp) collision. Higgs boson is not stable, it will decay into other particles immediately after it is generated from the pp collision. So in ATLAS and CMS, people try to find the decay products from Higgs boson to measure the Higgs boson. There are many decay channels to search for the Higgs boson. For example, in 2012 the combined result from ATLAS and CMS shows the first evidence of the Higgs boson [30]. It combines the  $H \rightarrow ZZ$ ,  $H \rightarrow \gamma\gamma$  and  $H \rightarrow WW$  channels. Although the Higgs boson can only directly couple to massive particle, it can still decay into the massless particle at the loop level decay. Later in 2018 the coupling with Fermion is observed:  $H \rightarrow b\bar{b}$ . And in 2020 a strong evidence for  $H \rightarrow \mu\mu$  is found in both ATLAS and CMS. Because of the clean background, it is much easier to find a Higgs boson decaying into a vector boson,

instead of the quark. However, the branching ratio for Higgs decaying into boson is much smaller than decaying into Fermion, as shown in Table 4.1 [57].

Table 4.1: Branching ratios of Higgs boson

$H \rightarrow b\bar{b}$	$H \rightarrow \tau\tau$	$H \rightarrow \mu\mu$	$H \rightarrow c\bar{c}$	$H \rightarrow g\bar{g}$	$H \rightarrow \gamma\gamma$	$H \rightarrow Z\gamma$	$H \rightarrow WW$	$H \rightarrow ZZ$
58 %	6.3 %	0.02 %	2.9 %	8.2 %	0.22 %	0.15 %	21 %	2.6 %

For the di-boson channel, both  $H \rightarrow ZZ$  and  $H \rightarrow WW$ , one of the  $Z$  and one of the  $W$  boson are virtual. Both ATLAS and CMS observed the Higgs boson decaying into vector boson earlier than decay channel with the largest branching ratio:  $H \rightarrow b\bar{b}$ . It is because for the bottom quark pair decaying channel, although the branching fraction is much larger than all other channels, there is much more background, too. The dominant background is the QCD process, and most of the outgoing particles are light quark [58](up quark and down quark). For the Higgs decaying into two b quarks:  $H \rightarrow b\bar{b}$ , the decaying b-quark will hadronize and produce a jet in the calorimeter. To find the  $H \rightarrow b\bar{b}$  decay, two b-hadron jet need to be identified. Although previously ATLAS built different algorithms to identify the b-hadron jet, based on the long lifetime of b-hadron, which will be introduced in Section 4.3.4, but since the cross-section of QCD process is many order higher than the Higgs boson production, it is still very difficult to distinguish the  $H \rightarrow b\bar{b}$  from the QCD background. There are two reasons that we still use  $H \rightarrow b\bar{b}$  as the Higgs boson decay channel. First, we are searching for the new physics, which means it is a rare decay and almost no  $H + \gamma$  events in the final state. So if we choose a channel with higher signal efficiency, we can achieve a better sensitivity. The second reason is that, since we are searching for a heavy resonance, from 600 GeV to 4 TeV, so the energy of the Higgs boson is also very large, which makes the two b-hadron collimated and merge into one large- $R$  jet (J), which is called boosted Higgs. ATLAS build many algorithms, which will be introduced in Section 4.3.5, to tag this boosted Higgs boson by tagging two b-hadron jets inside the large- $R$  jet (called Higgs jet). And these new algorithms can give a very good tagging performance, so that this analysis can benefit from it. In summary, we search for a Higgs boson and photon as the final

state. For the Higgs boson, a large- $R$  jet is reconstructed and the Higgs tagger is applied to tag the Higgs boson. I generate the MC sample, which will be introduced in Section 4.2, to find out the optimal cut value for the photon and large- $R$  jet, in Section 4.3, and study the model for signal, in Section 4.5.1, and background, in Section 4.6. To improve the search sensitivity, I implement a novel Higgs tagger, center-of-mass tagger, which will be introduced in Section 4.3.5. Compared with the previous CMS result, on top of the statistic gain, around 30 % improvement for the search sensitivity is observed, in Section 5.2.2.

## 4.2 Monte Carlo sample and Data

Before using the data for the analysis, in ATLAS, usually the Monte Carlo (MC) simulated sample is used for the analysis study first, which is called blinding. MC samples are generated for the study of SM background and the  $Z' \rightarrow H\gamma$  signal sample, and only after every step of the analysis is finalized, then the data can be used, which is called unblinding. For each MC sample, it represents one interaction process. In this analysis, there are four dominant SM background:  $\gamma + \text{jet}$ ,  $Z + \gamma$ ,  $W + \gamma$  and  $t\bar{t} + \gamma$ . All of these four processes have at least one photon and at least one large- $R$  jet at the final state. The major background is from  $\gamma + \text{jet}$  (85 %), and about 10 % are from  $Z/W + \gamma$ , only a few fraction is from  $t\bar{t} + \gamma$ . Tree-level  $\gamma + \text{jet}$  events can be produced through either scattering of a quark and a gluon, for example, Figure 4.1a, or through quark-antiquark annihilation plus and ISR photon and 2-jets processes with ISR or FSR photons. This kind of photon, participating in the hard scattering process, is called “prompt” photon. For the  $\gamma + \text{jet}$  process, it is also possible that a photon is not from hard scattering, but from fragmentation. In this case, this photon is not a prompt photon, and usually the photon  $p_T$  is very small. Since in this analysis, a high  $p_T$  photon is required, so those “not prompt” photons won’t contribute much to the final background. Since the  $\gamma + \text{jet}$  cross-section is very large, and that the photon energy is large enough, so that this process is the largest background contribution for this analysis. The other less dominant SM backgrounds are the SM production of

diboson  $Z/W + \gamma$ , Figure 4.1b shows the Feynman diagram example, where  $Z/W$  decay into two quarks; and SM production of  $t\bar{t} + \gamma$ , whose Feynman diagram is shown in Figure 4.1c.

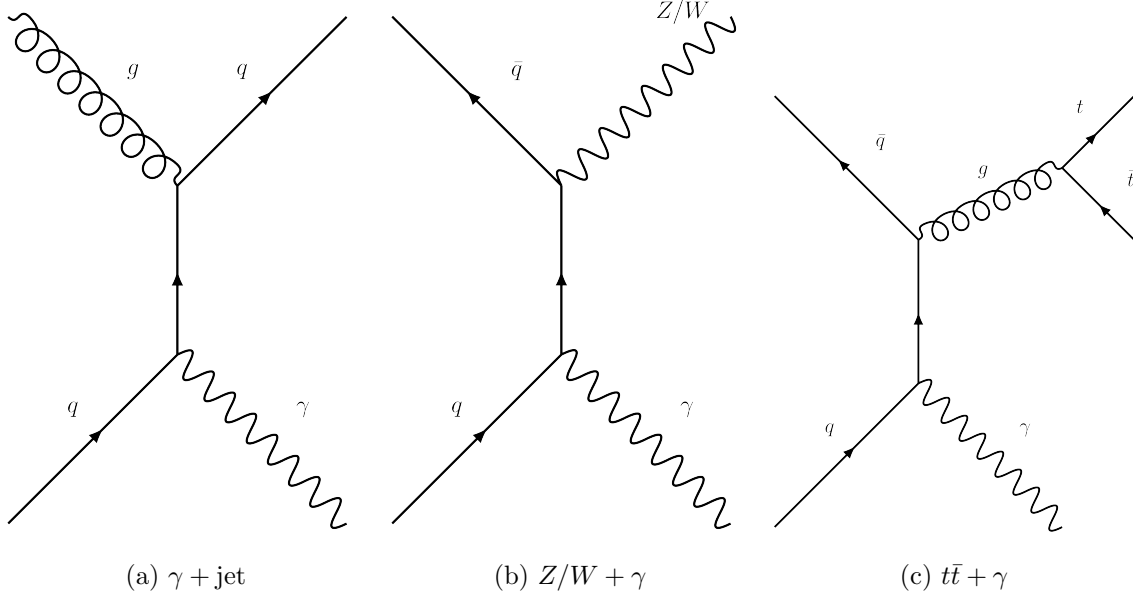


Figure 4.2: Feynman diagram for the dominant SM background. (a) Example for  $\gamma + \text{jet}$ ; (b) example for  $Z/W + \gamma$  and (c) example for  $t\bar{t} + \gamma$

The signal of this analysis is a spin-1 neutral particle, which can decay into a Higgs boson and a photon final state at one-loop level [56]:  $Z' \rightarrow H + \gamma$ , as shown in Figure 4.3

The  $\gamma + \text{jet}$  sample is generated by Sherpa v2.2.2 generator [59] with up to two additional parton emissions at next-to-leading-order (NLO) accuracy and up to four additional partons at leading-order (LO) accuracy using Comix [60] and OpenLoops [61]. The events were then merged with the Sherpa parton shower [62] using the ME+PS@NLO prescription [63]. Samples are generated using the NNPDF3.0nnlo PDF set [64], along with the dedicated set of tuned parton-shower parameters developed by the Sherpa authors. The  $Z/W + \gamma$  events were modeled with Sherpa 2.1.1 at LO with the CT10 PDFs [65] for both generators and the underlying event. The  $t\bar{t} + \gamma$  events were simulated using MadGraph5\_aMC@NLO v2.2.3 at LO with the CTEQ6L1 PDFs [66], then interfaced to Pythia 8.186 with the A14 parameter tune and the NNPDF23LO

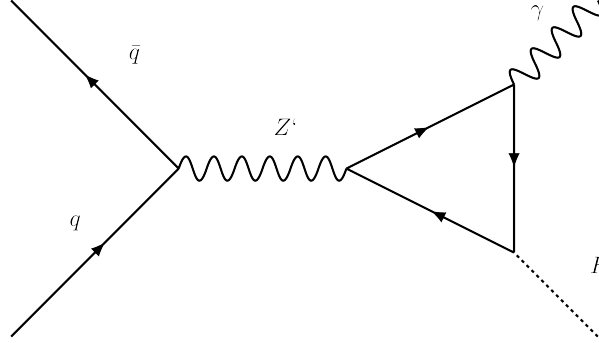


Figure 4.3: Feynman diagram for signal channel  $Z' \rightarrow H\gamma$

PDFs. The signal samples are generated for eight different mass points, 700 GeV, 800 GeV, 900 GeV, 1000 GeV, 1500 GeV, 2000 GeV, 3000 GeV, 4000 GeV, using the MadGraph LO v2.6.2 generator [67] interfaced to Pythia 8.235 [68] with the NNPDF23LO parton distribution functions (PDFs) [69] for both generators and the A14 set of tuned parameters [70] for the underlying event. The total decay widths of the  $Z'$  resonances were set to 4.2 MeV, which is much smaller than the experimental mass resolution, which varies from around 35 GeV at the 700 GeV signal mass point to 150 GeV at the 4000 GeV signal mass point. In the signal samples and  $t\bar{t} + \gamma$  background sample, EvtGen [71] was used to model charm and b-hadron decays. The effect of multiple pp interactions in the same and neighboring bunch crossings (pileup) is included by overlaying minimum-bias events simulated with Pythia 8.186 on each event of interest in all samples. The average pileup in the Run-2 dataset is 33.7. The generated samples were processed through a Geant4-based detector simulation [72, 73] and the same ATLAS reconstruction software as the data.

### 4.3 Event selection

This analysis is using full run 2 data (from 2015 to 2018) from ATLAS detector with center-of-mass energy of 13 TeV, only events passing “Good Run List” is used, corresponding to  $139\text{fb}^{-1}$ . The ATLAS detector is not working 100 % perfectly all the time, the Good Run List



tells us the period of data we can use. Since this analysis is looking for a photon and a Higgs jet, selection on the photon and the large- $R$  jet are applied to reduce the background and at the same time keep a high signal efficiency.

#### 4.3.1 Trigger

This analysis applies the photon trigger HLT\_g140\_loose trigger [74], which requires a loose online ID photon with photon transverse energy greater than 140 GeV. The [trigger efficiency](#) is shown in Figure 4.4 (inverted triangles).

#### 4.3.2 Baseline selection

For the final state, there is one photon and one Higgs boson. Photon candidates are required to have  $p_T > 200$  GeV and  $|\eta| < 1.37$ , where the first layer of the electromagnetic calorimeter has high granularity and provides large discrimination between prompt photons and photons from decays of hadrons inside jets. The identification (ID) of photons is performed by requiring the photon to pass a cut-based identification selection [75] based on shower shapes measured in the first two longitudinal layers of the electromagnetic calorimeter and the leakage into the hadronic calorimeter. The *tight* identification criteria is used to select photon candidate which has the highest background rejection power and reasonable high enough selection efficiency ( $> 90\%$ ) [75]. In addition, an isolation requirement is applied to photon candidates to further suppress fake photons from jets. The isolation selection is applied to a calorimeter-based variable  $E_{T,iso}^\gamma$  (TopoEtCone40), which is the sum of the energies of all topo-clusters calibrated with EM scale in a cone of  $\Delta R = 0.4$  around the photon direction without counting this photon energy. Additional corrections are then applied to remove the contribution from the underlying event, pileup collisions and the photon energy leaking in the isolation cone. The cut applied on the fully corrected isolation variable is  $E_{T,iso} < 2.45 + 0.022 \cdot E_T^\gamma$  (with energy expressed in GeV), which guarantees a signal efficiency around 98% over the  $E_T^\gamma$  range relevant for this analysis[75].  $E_T^\gamma$  is

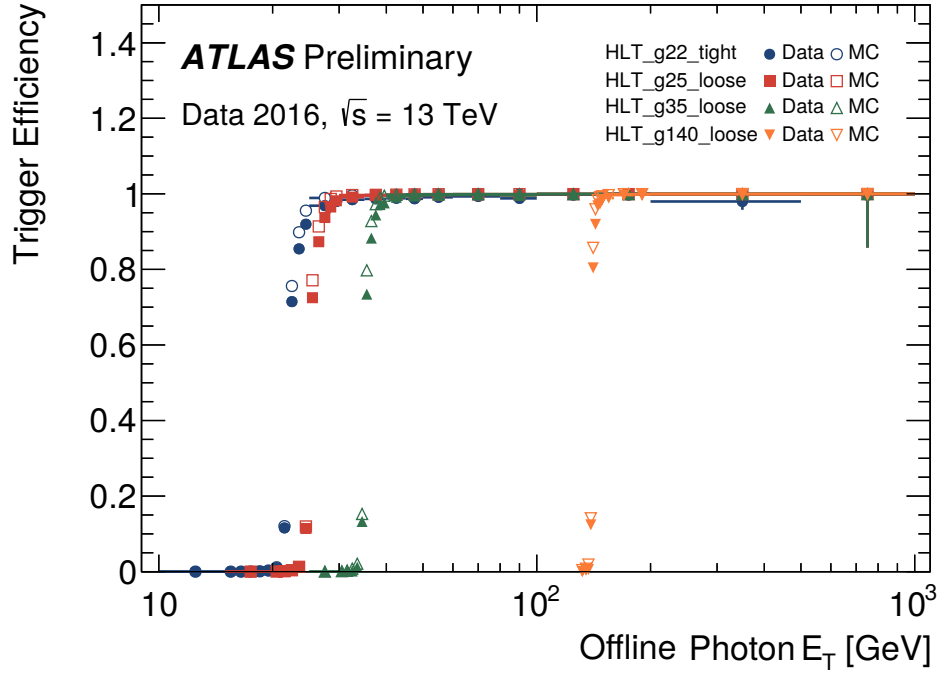


Figure 4.4: Efficiency of photon triggers requiring loose identification and  $E_T > 25$  GeV (squares), 35 GeV (triangles) and 140 GeV (inverted triangles, which is the one used in this analysis) and the efficiency of photon trigger requiring tight identification and  $E_T$  greater than 22 GeV (circles) for data (filled markers) and MC simulated samples (empty markers) as a function of the transverse energy of the photon candidates reconstructed offline passing the tight identification selection with  $|\eta| < 2.37$ , excluding the transition region between the barrel and endcap electromagnetic calorimeters at  $1.37 < |\eta| < 1.52$ . The efficiencies were measured with the bootstrap method using events recorded with a Level-1 trigger requiring an electromagnetic cluster with  $E_T > 15$  GeV. This Level-1 requirement is fully efficient selecting offline photons with  $E_T > 22$  GeV. No background subtraction is applied. The error bars represent the statistical uncertainty. Small drop in efficiency of 22 GeV tight trigger at high  $E_T$  has no effect in trigger performance, since 35 GeV loose trigger should be used above 50 GeV.

defined as the “transverse energy”:  $E_T^\gamma = \sqrt{p_T^2 + m^2}$ . Since the photon mass is zero, so for photon,  $E_T^\gamma = p_T^\gamma$ .

As for the Higgs boson, since it is produced from heavy resonance decay, the energy for the Higgs boson is much larger than its mass, and its hadronic decay products are contained inside the large- $R$  jet. So the large- $R$  jet is used to represent the boosted Higgs boson. The large- $R$  jets are reconstructed by anti- $kt$  algorithm with a larger radius parameter of  $R = 1.0$ . To reduce the pileup and underlying effect, a trimming algorithm with subjet  $R_{sub} = 0.2$  and subjet  $p_T$  fraction  $f_{sub} = 0.05$  is applied to large- $R$  jets [76]. Then the following selections are applied to the large- $R$  jets:

- large- $R$  jets are required to have  $|\eta| < 2.0$ , to ensures a good overlap with the tracking volume of ATLAS detector.
- large- $R$  jet with  $p_T > 200$  GeV,  $50 \text{ GeV} < m_J < 200 \text{ GeV}$ , to assure collecting the hadronic decay products of Higgs boson in the boosted cone jet.
- Any large- $R$  jet overlapping the photon with  $\Delta R(\text{large-}R \text{ jet}, \gamma) < 1.0$  is rejected.

The events are kept if more than one large- $R$  jet and more than one photon survive while the leading  $p_T$  ones are selected to construct the large- $R$  jet+ $\gamma$  system and used to calculate the invariant mass  $m_{J\gamma} = \sqrt{(E_J + E_\gamma)^2 - (\vec{p}_J + \vec{p}_\gamma)^2}$ . Figure 4.5 shows the signal efficiency with baseline selection applied as a function of the resonance mass. Figure 4.6 shows the comparison between data and MC background samples for several kinematic variables after baseline selection is applied.

### 4.3.3 Large- $R$ jet mass window optimization

To improve the final sensitivity, a two side optimized mass cut for large- $R$  jet is applied. For the Higgs jets, the mass distribution of the large- $R$  jets should peak at around the SM Higgs boson mass. However, the resolution of the mass distribution depends on the large- $R$  jet  $p_T$ . Figure 4.7 shows the large- $R$  jet mass and large- $R$  jet  $p_T$  distribution for different mass signal

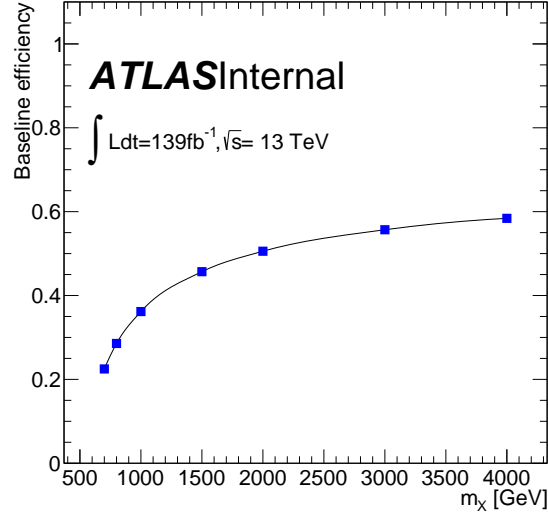


Figure 4.5: Signal efficiencies of events passing the baseline selection (before categorization)

sample. Besides, the large- $R$  jet mass distribution for background events need to be considered, too, since it is also depends on the large- $R$  jet  $p_T$ . So a fixed mass range for the large- $R$  jet mass is not optimal for the whole  $p_T$  range, and in this analysis an optimized mass cut, as a function of large- $R$  jet  $p_T$ , is applied for the large- $R$  jet. To determine the optimal cut:

- For each MC simulated signal sample with a specific hypothesis resonance mass  $m_{Z'}$ , after the baseline event selection, a two-dimensional scan is performed for the two boundaries of the large- $R$  jet mass window cut and the corresponding search significance for each cut combination is calculated as  $\epsilon/(\sqrt{B} + n/2)$ , where  $n = 3$  [76],  $\epsilon$  is the signal efficiency, and  $B$  is the number of background events predicted by the MC simulation. For  $\epsilon$  and  $B$ , they are estimated by counting the numbers of the corresponding events in which the invariant mass of the large- $R$  jet and photon pair ( $m_{J\gamma}$ ) falls within the resonance mass window:  $\bar{m}_Z - 2\sigma_{m_{Z'}} < m_{J\gamma} < \bar{m}_Z + 2\sigma_{m_{Z'}}$ . Here  $\bar{m}_Z$  and  $\sigma_{m_{Z'}}$  are the peak position and the core resolution of the reconstructed  $m_{J\gamma}$  distribution of the  $Z \rightarrow H + \gamma$  signal MC events, respectively, which will be introduced in Section 4.5.1. As described later in Section 4.5.1,

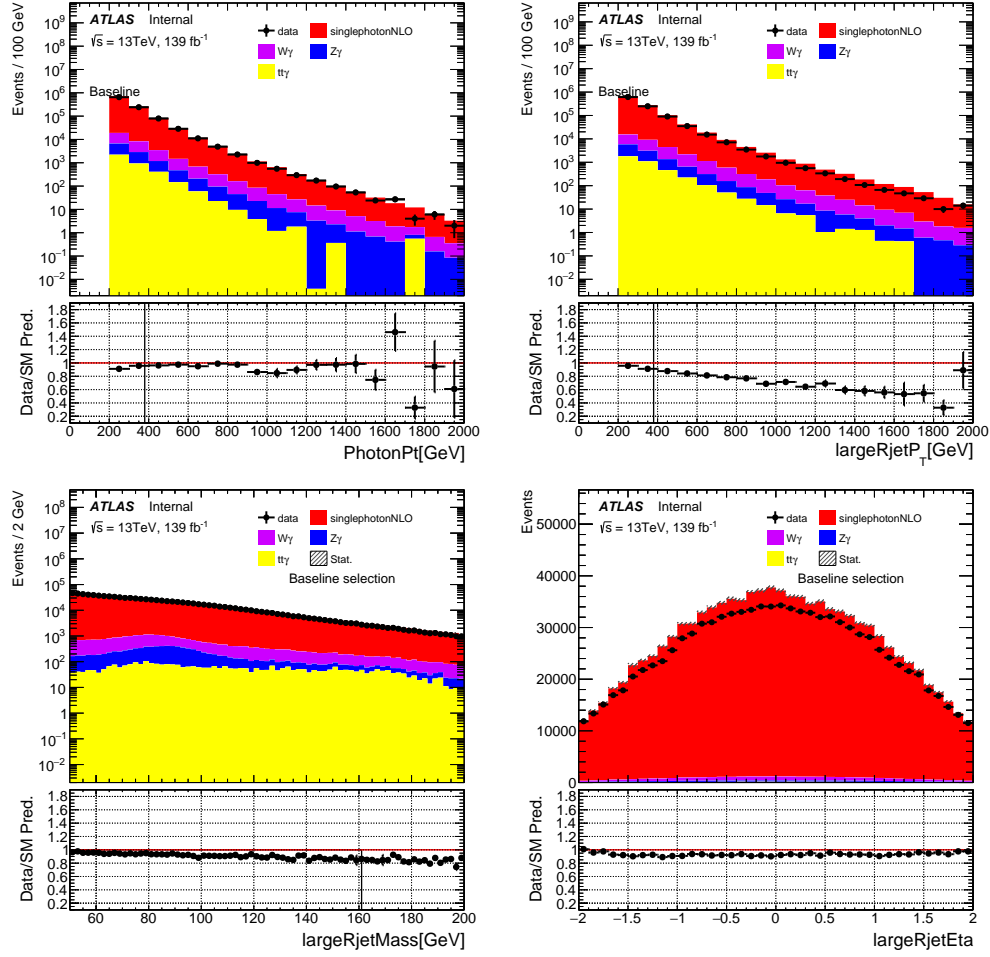


Figure 4.6: Data/MC comparisons after baseline selections for (a) photon  $p_T$ , (b) large- $R$  jet  $p_T$ , (c) large- $R$  jet mass and (d) large- $R$  jet  $\eta$ .

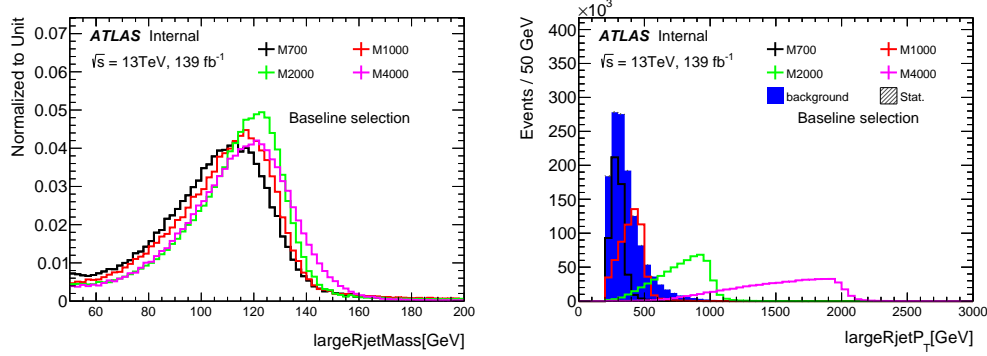


Figure 4.7: The large- $R$  jets (a) mass and (b)  $p_T$  distributions from the data events and MC simulated signal events after the baseline event selection.

the signal  $m_{J\gamma}$  distribution can be well described by a Crystal Ball function with a small fraction of a Gaussian function. The width of the Crystal Ball function is used here as the core resolution in the definition of the resonance mass window.

- The mass window selection that gives the highest search significance is chosen as the optimal cut for each given  $m_{Z'}$  point.
- The optimized mass window cut (lower and higher mass window boundaries) as a function of resonance mass  $m_{Z'}$  is then converted to a function of the large- $R$  jet  $p_T$  by replacing each  $m_{Z'}$  value with the a  $p_T$  value, which is chosen as the peak position of the large- $R$  jet  $p_T$  distribution of the corresponding signal MC events with the resonance mass  $m_{Z'}$ .
- The mass window cut as a function of large- $R$  jet  $p_T$  obtained from the above procedure is then fitted as a fourth-order polynomial, as shown in Figure 4.8(a). The resulting analytical functions are then used to apply the large- $R$  jet mass window selection based on the  $p_T$  of the large- $R$  jet  $p_T$  in the selected events of the analysis. Figure 4.8(b) shows the relative selection efficiency of the large- $R$  jet mass selection.

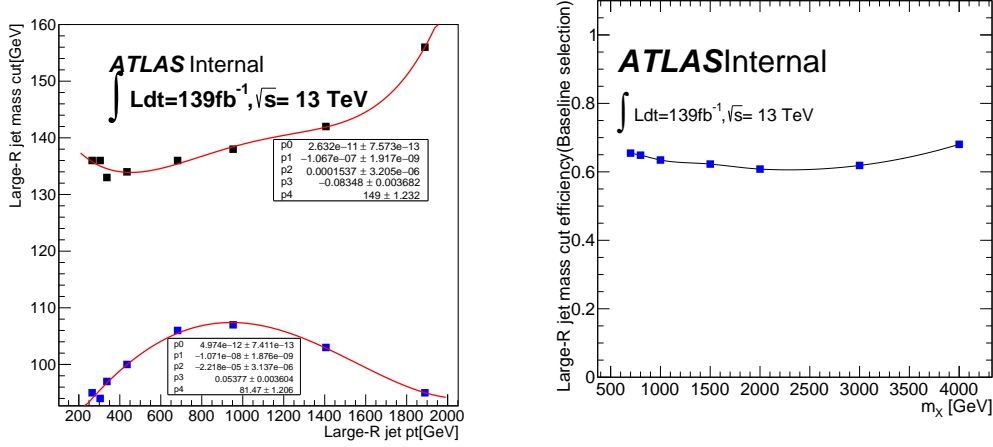


Figure 4.8: (a) The large- $R$  jet mass window boundaries as functions of large- $R$  jet  $p_T$ . The boundaries are parameterized with a fourth-order polynomial. (b) The large- $R$  jet mass selection efficiency as a function of resonance mass.

#### 4.3.4 The $b$ -tagging algorithm and previous ATLAS $H \rightarrow b\bar{b}$ tagger

In ATLAS, one of the very important task is to find the Higgs boson. From the SM, 58% of Higgs boson will decay into  $b\bar{b}$ , a lot of effort are made to identify the  $H \rightarrow b\bar{b}$  process. The two  $b$  quarks from the Higgs will hadronize and become two  $b$ -hadrons, and since  $b$ -hadron is not stable, it will decay into other hadrons and at the end form a jet in the calorimeter. So to identify the  $H \rightarrow b\bar{b}$  process is to find out two jets which are from the  $b$ -hadrons. The jet from the  $b$ -hadron is called  $b$ -hadron jet or  $b$ -jet, and the method to find the  $b$ -hadron jet is called  $b$ -tagging algorithm. The jet passing the  $b$ -tagging algorithm is called  $b$ -tagged jet. Here the background is the jet from other quark, like the up and down quark, and from the gluon. If the energy of the Higgs boson is not too large, these two  $b$ -hadron jets will not overlap with each other. This is called resolved jets, and ATLAS set the jet radius to be  $R = 0.4$ . ATLAS build a lot of different  $b$ -tagging algorithms, all of them are based on the special quality of the  $b$ -hadron, which is its long lifetime. Although  $b$ -hadron is not stable, it has a non-negligible lifetime, which makes it travels around 1mm before the decay. So for a  $b$ -hadron jet, if we collect all the tracks from this  $b$ -hadron, we

will find a secondary vertex from these tracks, while for the jet from the light quark, its tracks are all from the primary vertex, as shown in Figure 4.9 by Nazar Bartosik [77].

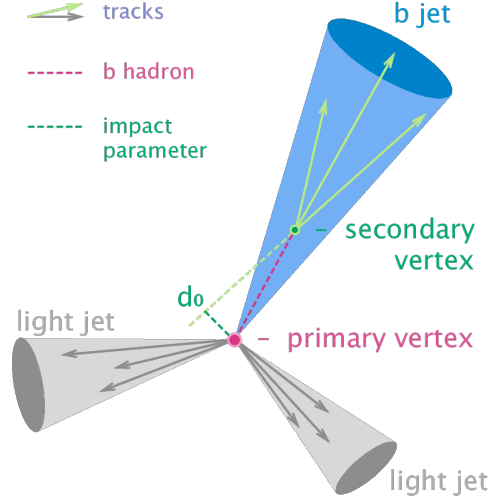


Figure 4.9: Illustration for the b-jet and light jet. For the b-jet, the associated tracks are from the secondary vertex, while for other jets, the tracks are from the primary vertex.

For this analysis, since it is searching for a heavy resonance decaying into a Higgs and a photon, which means the energy of the Higgs is very large, much larger than the Higgs mass. This will cause the two b-hadron jets to merge together due to the Lorentz boost, which is called boost/merge region. So instead of reconstructing the two separate resolved jets, first we reconstruct a larger jet, which includes all the final decay products from these two b-hadrons inside. In the previous ATLAS  $H + \gamma$  resonance search, besides the large- $R$  jet, another kind of jet, using the jet radius  $R = 0.2$ , is reconstructed. The large- $R$  jet is for the overall Higgs boson decay product, and the smaller jet is for the b-hadron decay product. After both large- $R$  jet and small jet are formed, the “ghost association” [78, 79, 80] algorithm is applied to associate the smaller jet to the large- $R$  jet, and those associated smaller jets are called the “subjet” of this large- $R$  jet. To determine whether this subjet is a b-jet, a machine learning algorithm, “MV2c10”, [81, 82] is applied on each subjet and return a  $b$ -tagging score, also called “MV2c10”, for this subjet. This  $b$ -tagging score, MV2c10, is a number at the range  $[-1,1]$ , and the higher



MV2c10 value, the higher probability that it is a b-jet. At the end, a threshold cut value is manually picked, and if the  $b$ -tagging score for this subjet is higher than the threshold, this subjet is tagged as a b-hadron jet.

#### 4.3.5 Center-of-mass subjet algorithm

In this analysis, a novel  $H \rightarrow b\bar{b}$  tagger is applied to tag the Higgs jet. This new tagger is called center-of-mass[83, 84] tagger (CoM), which is dedicated to the identification of  $H \rightarrow b\bar{b}$ , with two-body decay. It is done by reconstructing two subjets containing the b-hadrons within the large- $R$  jet. This algorithm uses the calorimeter cluster constituents of the trimmed large- $R$  jet [85]. First, a trimmed large- $R$  jet is reconstructed in the lab frame, and the associated tracks are collected. Second, both the tracks and the energy clusters are boosted into the center-of-mass frame of the large- $R$  jet. Then two subjects are reconstructed in the c.m. frame using EEKt algorithm [86, 87] with exclusive number of subjects set to 2. Different from anti- $kt$  algorithm, this EEKt algorithm, firstly proposed in the  $e^+e^-$  collision in LEP, defines the distance parameter:  $d_{i,j} = 2 \times \min(E_i^2, E_j^2) \times (1 - \cos \theta_{i,j})$  in the c.m. frame, where  $i, j$  are the indices of the energy cluster, and the  $\theta_{i,j}$  is the relative angle between  $i^{th}$  and  $j^{th}$  energy cluster. Similar to anti- $kt$ , the algorithm calculates the distance between two clusters, and finds out the minimum value from  $d_{iB}$ . Then the corresponding  $i^{th}$  and  $j^{th}$  clusters are combined into one cluster and it re-calculate  $d_{iB}$  with the new cluster lists. The algorithm will continue this process until two jets are reconstructed, since the two-body decay  $H \rightarrow b\bar{b}$ , is expected. Compared with the previous ATLAS  $H \rightarrow b\bar{b}$  tagger, which uses anti- $kt$   $R=2$  for subjet reconstruction, the CoM subjet can avoid the extremely high energy cases where two b-hadron can merge into one anti- $kt$   $R=2$  subjet. After the subjet reconstruction, the tracks in the large- $R$  jet are associated to the subjet in the c.m. frame. The angular distance is defined as:  $y_{i,j} = 2 \times (1 - \cos \theta_{i,j})$ , where  $i-$  and  $j-$  are two objects, which can be subjet or track, in the c.m. frame, and  $\theta$  is the open angle between these two objects. Tracks within range:  $y_{subjet,track} < y_{cut} = 0.8$  are associated to that CoM subjet [88]. Since in the c.m. frame, the two subjects are at the opposite direction, so the track

can only be associated to one of the subjet. And the threshold  $y_{cut} = 0.8$  is independent of the large- $R$  jet  $p_T$ . In the c.m. frame, the open angle, in which tracks are associated to the subjet, is a fixed value, but in the lab frame, this open angle depends on the boost vector. The procedure of CoM subjet reconstruction and track to subjet association can be summarized in Figure 4.11:

- (a) large- $R$  jet reconstruction and track to large- $R$  jet association: large- $R$  jet are reconstructed in the lab frame, and tracks are associated to the large- $R$  jet within  $\Delta R < 1.0$ .
- (b) Boost to c.m. frame of large- $R$  jet: the trimmed energy clusters and the associated tracks to the large- $R$  jet are boosted to the c.m. frame of the large- $R$  jet.
- (c) CoM subjet reconstruction: two subjets are reconstructed exclusively using the energy clusters in the c.m. frame
- (d) track to subjet association in c.m. frame: tracks are exclusively associated to the closest CoM subjet with a threshold  $y_{ij} < j_{cut} = 0.8$  in the c.m. frame. Not all the tracks will be associated to the subjet.
- (e) Boost back to lab frame: both the CoM subjets and their associated tracks are boosted back to the lab frame. This process doesn't change anything about the kinematic information about the tracks, but only the relationship between the tracks and the subjets.

The logic to reconstruct the CoM subjet is that, in the c.m. frame of the Higgs boson, its decay product, two b-hadrons, will fly back to back, so that it is much easier to reconstruct two subjet and do the track to subjet association in the c.m. frame. While for QCD jet, in the c.m. frame the particle distribution is more likely to be random, as shown in Figure 4.13[83].

Afterward, the  $b$ -tagging algorithm, MV2c10, mentioned in Section 4.3.4, is applied on each CoM subjet to identify those CoM subjets containing b-hadrons. For this analysis, a fixed cut value, 0.71, is applied to the MV2c10 variable, which is the  $b$ -tagging output. If the MV2c10 value for the CoM subjet is higher than 0.71, then it is considered as a b-hadron subjet. This cut value is chosen so that the overall  $H \rightarrow b\bar{b}$  efficiency in the Graviton sample  $G \rightarrow HH \rightarrow bbbb$  is around

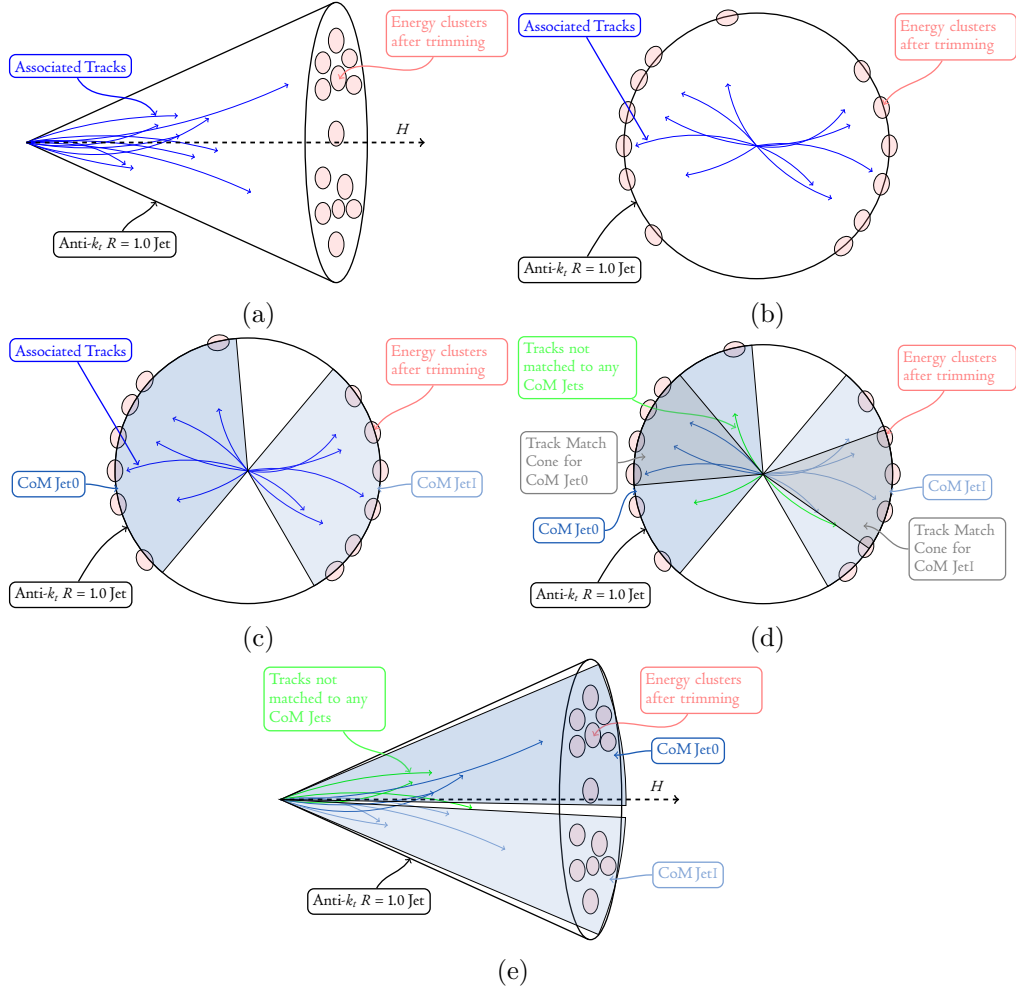


Figure 4.11: CoM subjet reconstruction and track association

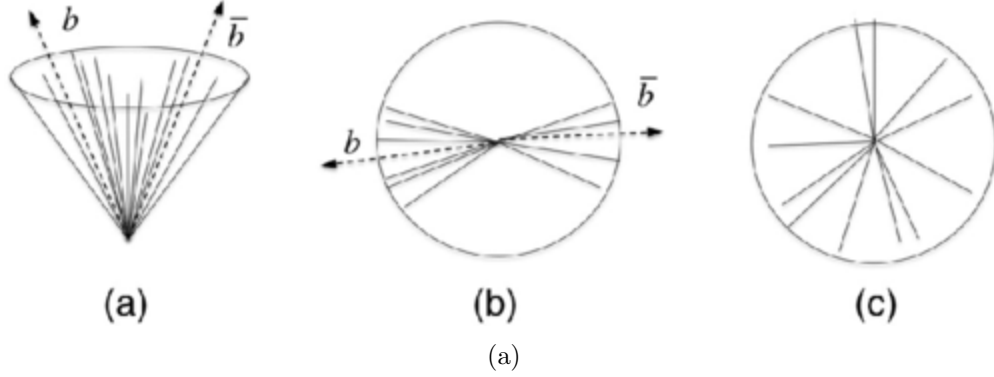


Figure 4.13: Illustration of the constituent particle distribution of a jet. (a) Higgs jet in the lab frame. (b) Higgs jet in the jet rest frame. (c) QCD jet in its rest frame.

77 %. The events are divided into three categories based on the number of  $b$ -hadron subjet inside the large- $R$  jet:

- Double  $b$ -tagged category: both two CoM subjets are identified as  $b$ -hadron subjets (pass 0.71 cut value for MV2c10)
- Single  $b$ -tagged category: only one of the CoM subjet is identified as  $b$ -hadron subjet (pass 0.71 cut value for MV2c10)
- Untagged category: None of the CoM subjets are identified as  $b$ -hadron subjets

Only events at single  $b$ -tagged and double  $b$ -tagged categories are used to search for the resonance. The relative selection efficiency of the different  $b$ -tagged categories for the MC signal samples after the baseline selection and large- $R$  jet mass optimization is shown in Figure 4.14.

Besides the anti- $kt$   $R=0.2$  and CoM subjet reconstruction algorithm, ATLAS build another two subjet reconstruction algorithms: variable-radius (VR) and Exclusive- $k_T$  (ExKt)[88]. For VR, instead of using a fixed radius side for the subjet, the radius for the subjet depends on the  $p_T$  as:

$$R = \frac{\rho}{p_T} \quad (4.1)$$

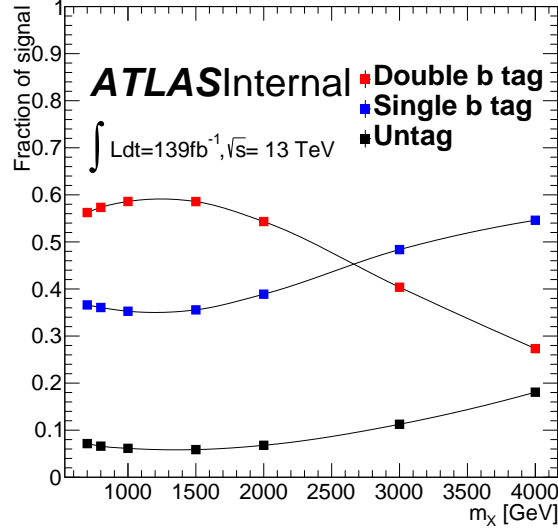


Figure 4.14: The fraction of the MC signal events in different  $b$ -tagged categories as a function of resonance mass after baseline selection and large- $R$  jet mass optimization.

$\rho$  is a constant, the optimal value is 30 GeV. And the optimal maximum and minimum value for  $R$  are  $R_{max} = 0.4$ ,  $R_{min} = 0.06$ . For ExKt, it uses the same distance metric as the common anti- $kt$  algorithm, but it will not stop clustering constituents until two jets are exclusively reconstructed. Figure 4.16 shows the  $b$ -tagging performance for the anti- $kt$   $R=0.2$  subjet, VR subjet, ExKt subjet, and CoM subjet algorithms. For the  $H \rightarrow b\bar{b}$  tagging, the majority background are the jets from other quark or gluon, which is called QCD background. In Figure 4.16, Y-axis is the QCD jet rejection, defines as the inverse of fraction of QCD jet passing the double  $b$ -tagging selection criteria, X-axis is the Higgs efficiency. For the same Higgs efficiency, the higher background rejection means better tagging performance. The performance is studied in three different  $p_T$  range of the large- $R$  jet. In general, CoM subjet algorithm has the best performance among these four  $H \rightarrow b\bar{b}$  taggers for all these three  $p_T$  ranges.

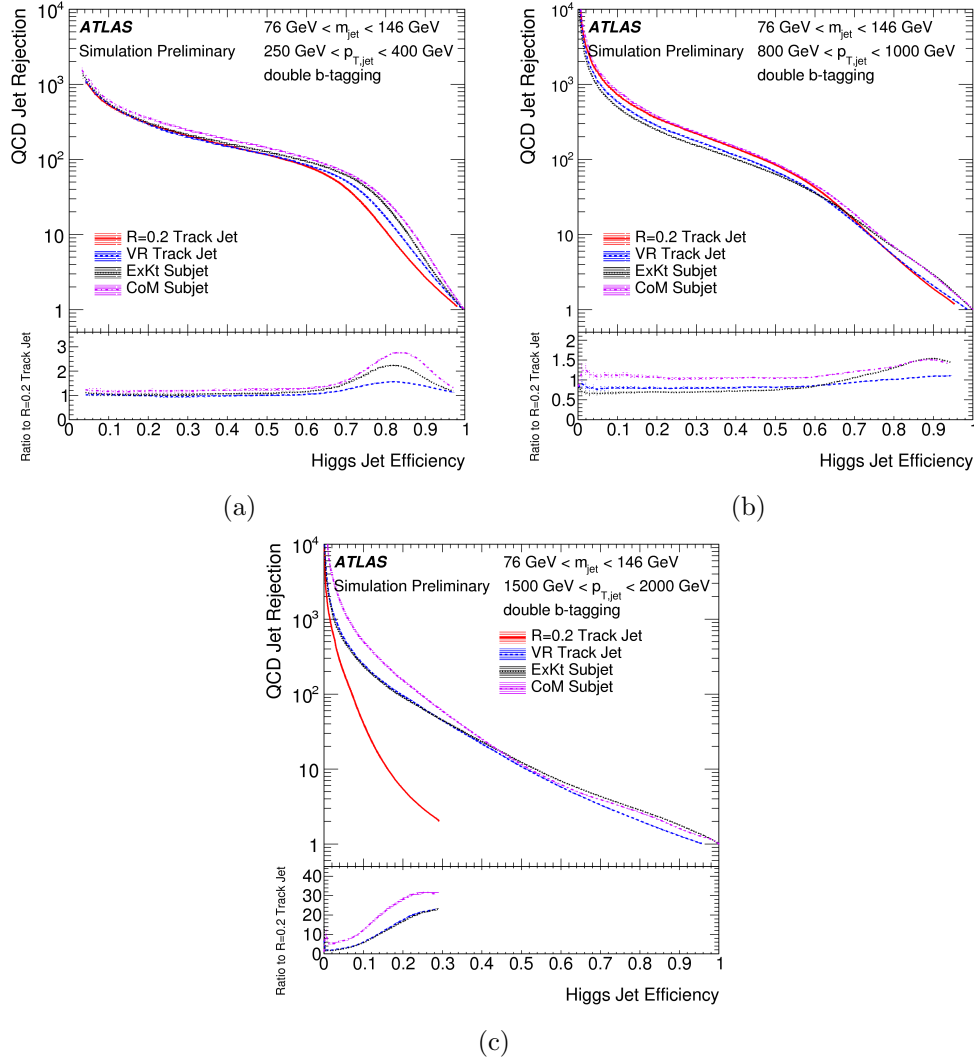


Figure 4.16: QCD jet rejection as a function of  $h \rightarrow b\bar{b}$  efficiency when applying double  $b$ -tagging selection on subjets found by the anti- $kt$   $R=0.2$  subjet, VR subjet, ExKt subjet, and CoM subjet algorithms in different  $p_T$  regions. In general, CoM subjet algorithm has the best performance among these four  $H \rightarrow b\bar{b}$  tagger.

#### 4.3.6 Optimization of the selection criteria of photon and large- $R$ jet $p_T$

After applying the CoM subjet  $b$ -tagging selection, the selection requirement for large- $R$  jet  $p_T$  and photon  $p_T$  are optimized to further improve the search sensitivity. For the signal events, since it is a two-body decay, the photon  $p_T$  and large- $R$  jet  $p_T$  are strongly correlated with each other and both of them are correlated to the resonance mass, so that in this analysis this optimization is done requiring that the cut value for large- $R$  jet  $p_T$  is proportional to the photon  $p_T$  cut value, to reduce the complexity in the optimization. A linear function is chosen to parametrize the cut value as a function of the resonance mass. The cut value ratio: large- $R$  jet  $p_T$  cut / photon  $p_T$  is chosen to be 80 %. This 80 % is chosen because the large- $R$  jet  $p_T$  resolution for signal events is larger than the photon  $p_T$  resolution and a looser selection can keep more signal events. For the optimization of the large- $R$  jet and photon  $p_T$ :

- For each MC signal sample with a specific resonance mass, after the baseline event selection and mass window cut, a scan is performed by applying a minimum  $p_T$  requirement on both the photon and the large- $R$  jet:  $p_T^\gamma > p_T^{\min}$  and  $p_T^{\text{jet}} > 0.8p_T^{\min}$ . The corresponding search significance for each  $p_T^{\min}$  is then calculated as  $\epsilon/(\sqrt{B} + 3/2)$ , where the signal efficiency  $\epsilon$  and the expected background event number are estimated using the identical procedure used for the large- $R$  jet mass window optimization, described in detail in Sec. 4.3.3.
- The value of  $p_T^{\min}$  that gives the highest search significance is chosen as the optimal cut for each given  $m_{Z'}$  point.
- The optimized  $p_T^{\min}$  as a function of the resonance mass  $m_{Z'}$  is found to be reasonably described by a linear function up to  $m_{Z'} = 2000$  (1500) GeV for single (double)  $b$ -tagged category, as shown in Fig 4.18. For resonance signal with  $m_{Z'} > 2000$  (1500) GeV, the  $p_T$  optimization yields no improvement of the search sensitivity for single (double)  $b$ -tagged category, and a very tight requirement of the  $p_T^{\min}$  will actually reduce the search significance. This is actually what we expected as the expected background for high mass

$H\gamma$  resonance is very low, and the search sensitivity is completely dominated by the signal selection efficiency.

- As the possible  $H\gamma$  resonance mass is unknown, a direct application of the optimized  $p_T^{\min}$  is not trivial unless we repeat the analysis for each given  $m_{Z'}$ . To simplify the search, the optimized  $p_T^{\min}$  as a function of the  $m_{Z'}$  is converted to a function of the reconstructed invariant mass  $m_{J\gamma}$  of selected events as:

$$p_T^\gamma > p_T^0 + a \times m_{J\gamma}, \quad p_T^{jet} > 0.80 \times p_T^\gamma \quad (4.2)$$

where  $p_T^0 = 12.0$  GeV (121.8 GeV) and  $a = 0.35$  (0.22) for the selected events with  $m_{J\gamma} < 2000(1500)$  GeV in the single (double)  $b$ -tagged category. For events with  $m_{J\gamma} > 2000(1500)$  GeV, the selection requirements on the photon and the large- $R$  jet  $p_T$  are the same as the ones for events with  $m_{J\gamma} = 2000(1500)$  GeV. The relative selection efficiencies of the optimized  $p_T$  requirements of the photon and the large- $R$  jet as a function of the resonance mass  $m_{Z'}$  for MC simulated signal events are shown in Fig. 4.18.

## 4.4 Signal sample overall efficiency

Figure 4.19 shows the signal overall efficiency for all the MC signal samples. The overall efficiency is defined as the ratio of the number of signal events, passing all the selection and applying the optimization mentioned in this section, to the yield number, which is the cross-section times luminosity. This overall efficiency is fitted with a fourth-order polynomial to parametrize the efficiency.

## 4.5 Signal model

### 4.5.1 Signal shape probability density function

For signal events, the distribution of resonance mass  $m_{j\gamma}$  is modelled by a joint probability density function(pdf) of a Crystal Ball(CB) [89], representing the core part of the



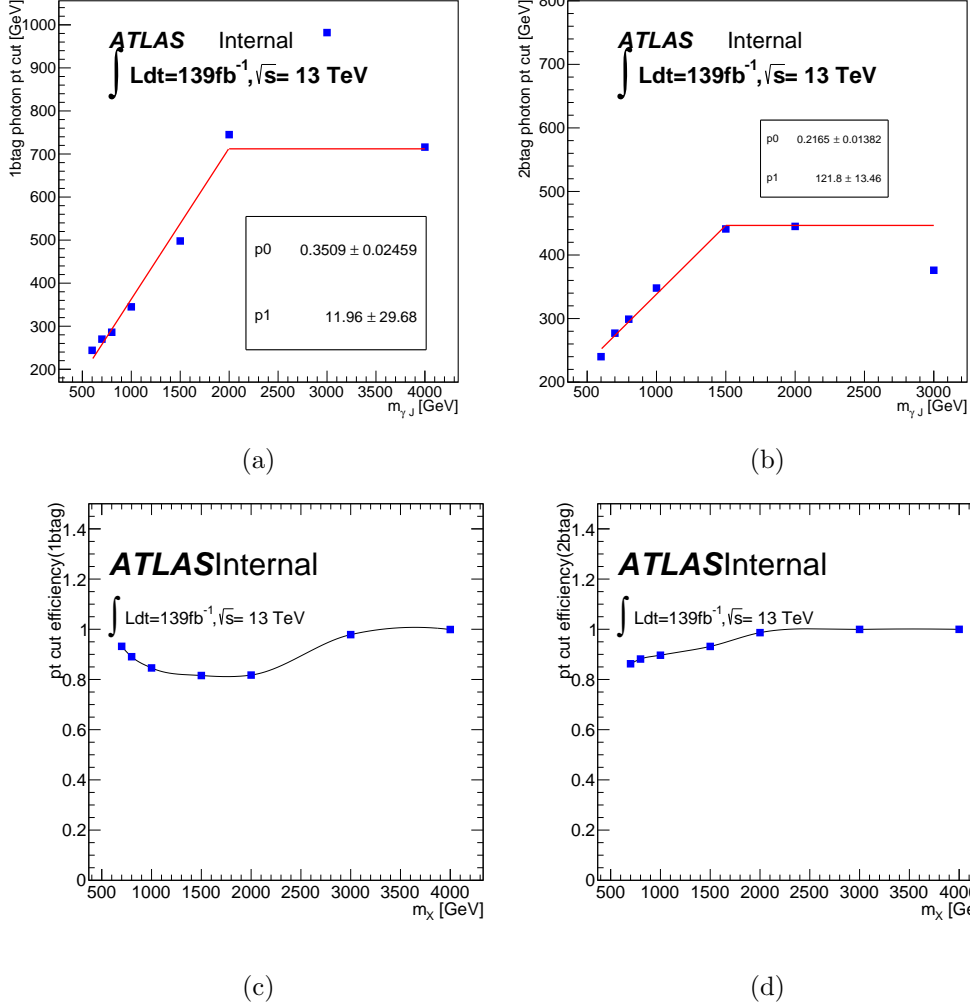


Figure 4.18: Top plots: The optimized minimum  $p_T$  requirement of the photon as a function of the resonance mass  $m_{Z'}$  for MC simulated signal events in the single  $b$ -tagged (Left) and double  $b$ -tagged categories (Right). Bottom plots: the relative selection efficiencies of the optimized  $p_T$  requirements of the photon and the large- $R$  jet as a function of the resonance mass  $m_{Z'}$  for MC simulated signal events in the single  $b$ -tagged (Left) and double  $b$ -tagged categories (Right).

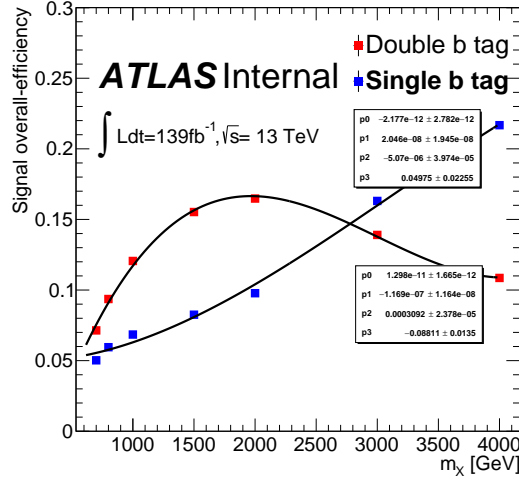


Figure 4.19: Signal overall efficiency after all the selection introduced in this section.

well-reconstructed events, and a Gaussian distribution(Gauss), representing the tails of the poorly reconstructed events:

$$f_{\text{signal}}(m_{J\gamma}) = f_{CB} \cdot CB(m_{J\gamma}; \mu, \sigma_{CB}, \alpha_{CB}, n_{CB}) + (1 - f_{CB}) \cdot \text{Gauss}(m_{J\gamma}; \mu, \sigma_{\text{Gauss}})$$

$$CB(m; \mu, \sigma, \alpha, n) = N_{CB} \cdot \begin{cases} \exp\left(-\frac{(m-\mu)^2}{2\sigma^2}\right) & \text{for } \frac{m-\mu}{\sigma} > -\alpha \\ \left(\frac{n}{|\alpha|}\right)^n \exp\left(-\frac{|\alpha|^2}{2}\right) \left(\frac{n}{|\alpha|} - |\alpha| - \frac{m-\mu}{\sigma}\right)^{-n} & \text{for } \frac{m-\mu}{\sigma} \leq -\alpha \end{cases} \quad (4.3)$$

$$\text{Gauss}(m; \mu, \sigma) = N_{\text{Gauss}} \exp\left(-\frac{(m-\mu)^2}{2\sigma^2}\right)$$

Where  $\mu$  is the position of the peak and shared between CB and the Gauss distribution.  $\sigma_{CB}$  is the width of the CB and  $\sigma_{\text{Gauss}}$  is the width of the Gauss.  $n_{CB}$  together with  $\alpha_{CB}$  control the exponential part of the CB, while  $n_{CB}$  is fixed to 100 in order to reduce the complexity of the fitting.  $N_{CB}$  and  $N_{\text{Gauss}}$  are the normalization factors of CB and Gauss. At the end  $f_{CB}$  is the relative fraction to be fixed in the fitting. The resonance mass distribution of the MC signal sample is fitted using the signal pdf in Equation 4.3. Examples of the fitting result are shown in Figure 4.21. Good agreement between the MC signal events  $m_{J\gamma}$  distribution and the signal pdf is observed.

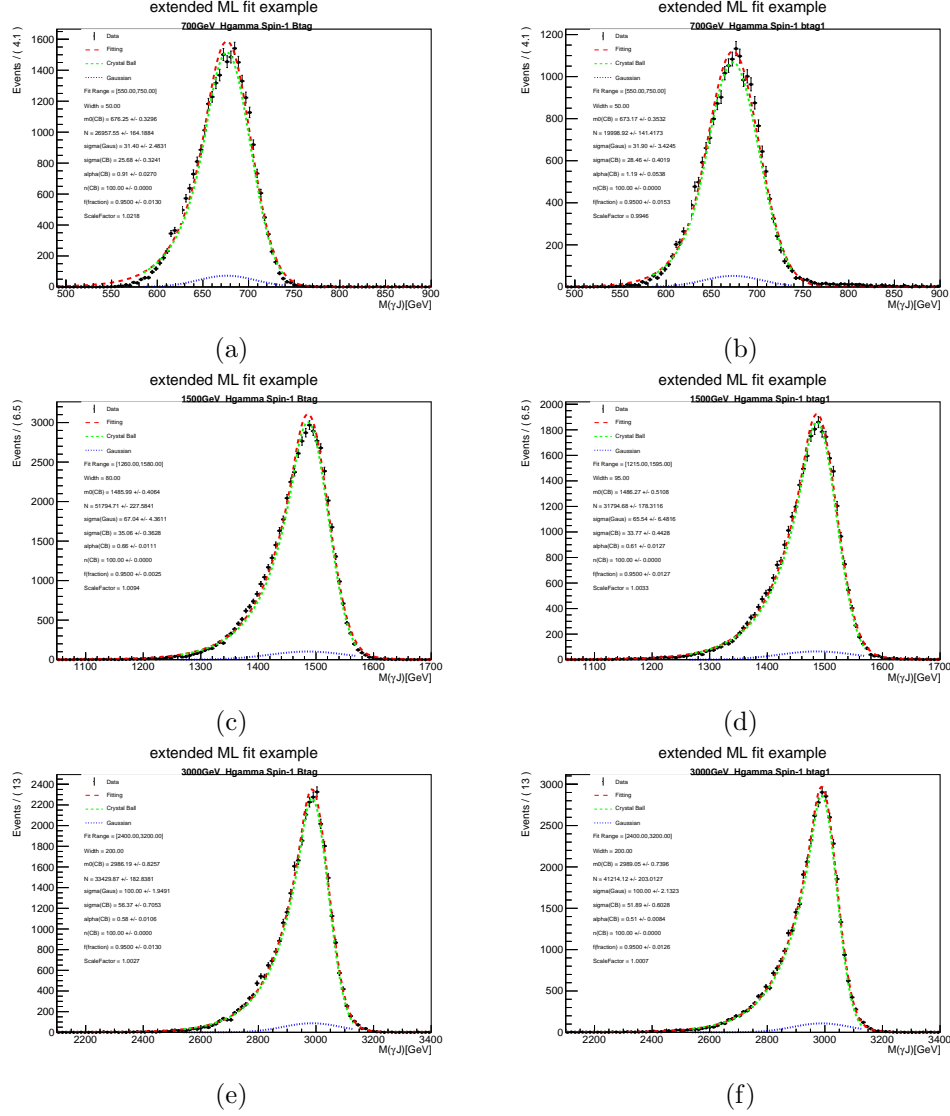


Figure 4.21: Signal shape parameterization with an analytical function for several different resonance masses ( $m_{Z'}$ ). Plots on the left shows the result for double  $b$ -tagged category and plots on the right presents the result for single  $b$ -tagged category. The black points are from MC simulation events, the green curves are from the fitting result, and the red curves are from the analytical pdf in which their parameters are set to the predicted values from the parametrized function as described in Equation 4.3.

### 4.5.2 Signal pdf parametrization and interpolation

This analysis is searching the heavy resonance decaying into a Higgs boson and a photon in a large resonance mass range, so in principle we need to generate the MC signal sample for each mass point. Then the signal pdf for each mass hypothesis can be reconstructed from the signal MC sample. However, such an approach is unrealistic due to the limited quota of storage spaces and computing resources. Instead of generating a lot of MC signal samples, only eight MC signal samples with different mass points of the hypothesis resonance mass are generated: 700, 800, 900, 1000, 1500, 2000, 3000, 4000 GeV. An extrapolation method is used to build the analytical signal pdf for each mass hypothesis:

- For MC signal events for each mass hypothesis, passing all the selection criteria, the resonance mass  $m_{J\gamma}$  distribution in both the single  $b$ -tagged and double  $b$ -tagged categories are fitted separately with the signal model described in Section 4.5.1. The fitted results for three mass points are shown in Figure 4.21.
- In the signal model, totally there are five parameters are float during the fitting:  $\mu$ ,  $\sigma_{CB}$ ,  $\alpha_{CB}$ ,  $\sigma_{Gauss}$ , and  $f_{CB}$ . For each parameter, the fitted result for each mass points is collected and parametrized using a polynomial function of the resonance mass:
  - The second-order polynomial is used for the peak resolution  $\sigma_{CB}$ , tail width  $\sigma_{Gauss}$  and the relative fraction of CB  $f_{CB}$ .
  - The third-order polynomial is used for the CB parameter:  $\alpha_{CB}$ , since the behavior is more complex.
- Figure 4.23 and 4.25 show the fitted value of each parameter at eight different mass points and the parametrization result as a function of resonance masses in double  $b$ -tagged and single  $b$ -tagged categories.

- The signal pdf models for all the hypothesis mass points are generated, whose parameters values are fixed to the prediction from the parametrized function. And the peak position  $\mu$  represents the resonance mass value.

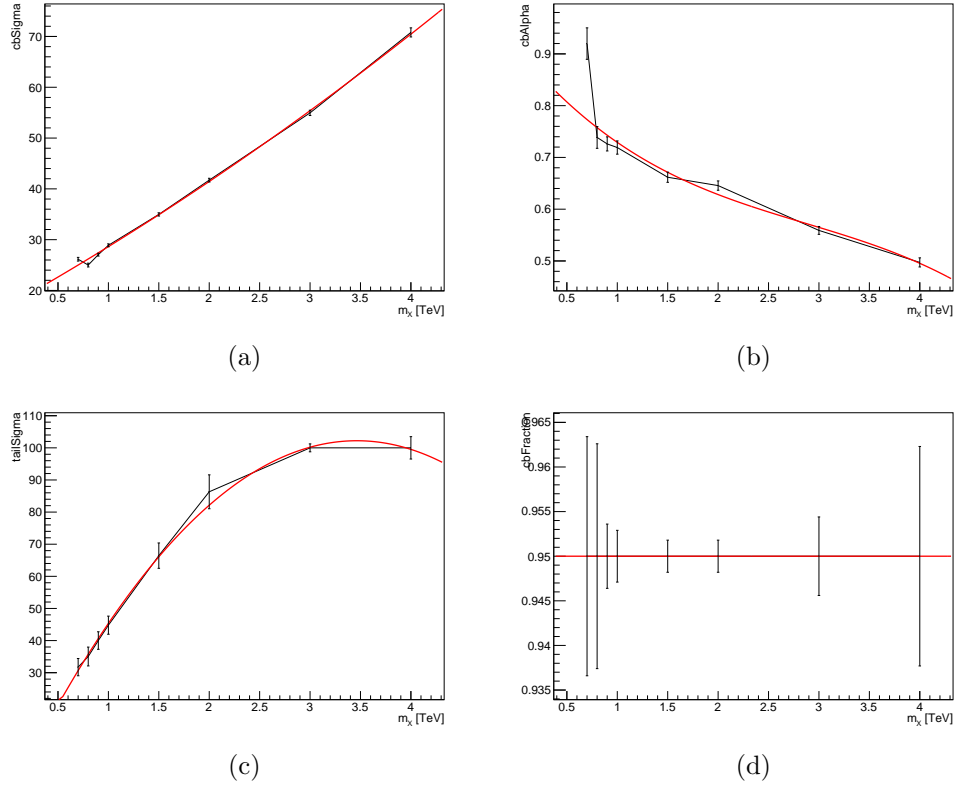


Figure 4.23: Parameterization of the signal PDF parameters:  $\sigma_{CB}$  (Top left) ,  $\alpha_{CB}$  (Top right),  $\sigma_{Gauss}$  (Bottom left) and  $f_{CB}$  (Bottom right) as functions of the resonance mass in the double  $b$ -tagged category.

The signal pdf for different hypothesis mass points from the parametrization (red curve with 100 GeV per step) are shown in Figure 4.27 for double  $b$ -tagged (a) and single  $b$ -tagged (b) categories. The blue curve shows the shape for the signal pdf obtained from the direct fits to the MC signal events. The pdf from parametrization is in good agreement with the direct fitting result.

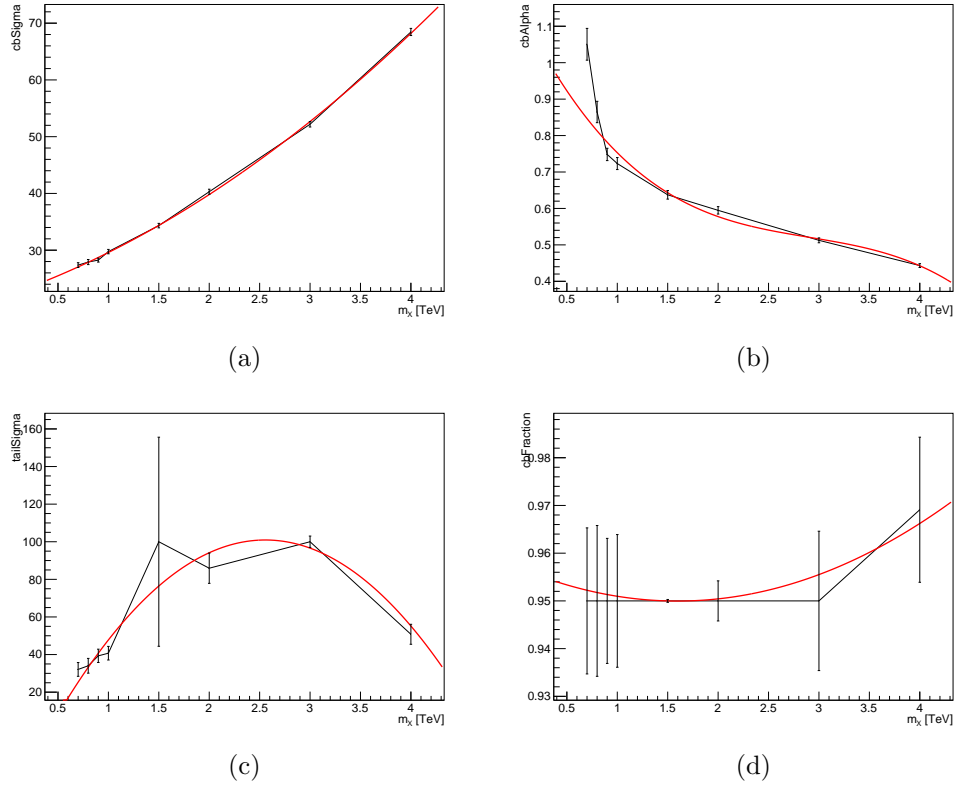


Figure 4.25: Parameterization of the signal PDF parameters:  $\sigma_{CB}$  (Top left) ,  $\alpha_{CB}$  (Top right),  $\sigma_{Gauss}$  (Bottom left) and  $f_{CB}$  (Bottom right) as functions of the resonance mass in the single  $b$ -tagged category.

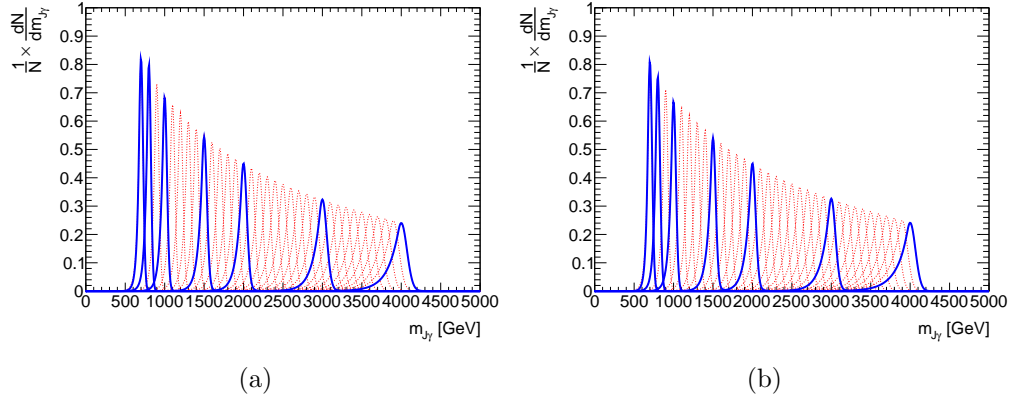


Figure 4.27: Comparison of signal shapes interpolated from coefficients parametrization (red) and the signal shapes obtained from MC events fit (blue) for (a) double  $b$ -tagged and (b) single  $b$ -tagged categories. The interpolated shape are plotted with 100 GeV per step.

## 4.6 Background model

### 4.6.1 Background composition

There are four dominant SM MC background,  $\gamma + \text{jet}$ ,  $Z + \gamma$ ,  $W + \gamma$  and  $t\bar{t} + \gamma$ , as mentioned in Section 4.2. Table 4.2 shows the expected background events number for the MC background samples in double  $b$ -tagged and single  $b$ -tagged categories. The background is dominated by the  $\gamma + \text{jets}$  production, which consists of  $\sim 90\%$  of the total number of background events. The fraction of background contributions from the SM  $t\bar{t}\gamma$  production after baseline selection is quite small, but its fraction is significantly enhanced after the final selection criteria applied ( $b$ -tagged jet selections), and accounts for around 3% in both double  $b$  and single  $b$ -tagged categories. Other backgrounds such as SM  $V\gamma$  ( $V = W/Z$ ) events have similar a contribution as the one from the  $t\bar{t}\gamma$  production.

### 4.6.2 Background pdf

This analysis is searching for a resonance bump in a falling smooth distribution over the  $m_{J\gamma}$  spectrum. To describe this falling  $m_{J\gamma}$  distribution of background events, an analytical function is

Table 4.2: Expected composition of backgrounds at luminosity =  $139 \text{ fb}^{-1}$  in the range of  $m_{J\gamma}$  from 600 GeV to 4200 GeV.

SR	double $b$ -tagged	single $b$ -tagged	baseline
SM $\gamma$ + jets	628	8269	1052710
SM $Z\gamma$	29	113	7809
SM $W\gamma$	8.7	216	21984
SM $t\bar{t}\gamma$	19.1	247	3787.2
Total Backgrounds	685	8845	1086290

used:

$$B(m_{J\gamma}; p_i) = N(1 - x)^{p_1} x^{p_2 + p_3 \log(x) + p_4 \log^2(x) + p_5 \log^3(x) + \dots} \quad (4.4)$$

Where  $x = m_{J\gamma}/\sqrt{s}$ ,  $N$  is a normalization parameter,  $p_i$ ,  $i = 1, 2, \dots$  are dimensionless shape parameters to be determined in the fitting. This is a common background function used in ATLAS for di-jet background [90]. Similar to the polynomial function, it is free to choose the order of this function, the number of free shape parameters,  $p_i$ ,  $i = 1, 2, \dots$ . To determine the optimal order for the background function, a data-driven study is applied. In ATLAS, data in the signal region, which is the data events in single  $b$ -tagged and double  $b$ -tagged categories in this analysis, cannot be used before unblinding. The unblinding requires that the analysis strategy needs to be determined and fixed before using the real data in the signal region, to avoid bias when doing the optimization/selection. So to determine the best number of the free parameters for the background distribution in the final fit in this analysis, instead of directly using data in signal region, this data-driven study is applied in the “control region”, in which the events have similar kinematic distributions to the events in the signal region. The definition of the control region is shown in Section 4.6.3 and the detail of the data-driven study in the control region is shown in Section 4.6.4.



### 4.6.3 Control region study

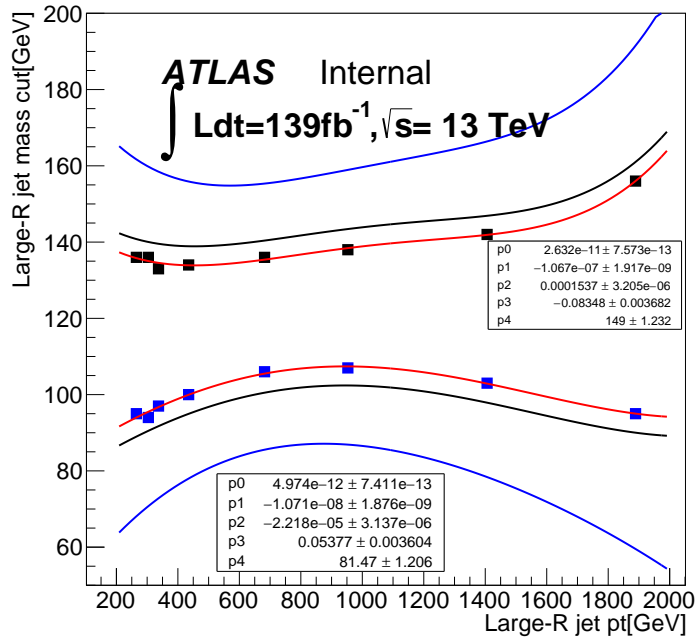
For an ideal control region, the kinematic distribution for the background events should be identical or very close to the distribution for the background events in the signal region and at the same time the signal events in the control region are rare, so that the data in the control region can be used to study the background events only. In this analysis, two selection criteria are used in the control region (CR) definition: large- $R$  jet mass side-band region and un-tagged category for the  $b$ -tagged selection. The control region is defined as the un-tagged category in the large- $R$  jet mass side-band region.

#### 4.6.3.1 large- $R$ jet mass side-band region

The large- $R$  jet mass side-band region is defined by inverting the large- $R$  jet mass optimization selection as defined in Section 4.3.3. The side-band selection is shown in Figure 4.29, the central area between two red curves is the signal region. Outside the signal region, a 5 GeV gap is defined to reduce the signal leaking from the signal region to the side-band region, which is the gap between the red and black curve for both upper and lower parts. The side-band region is divided into two sub-parts, on both the upper and lower sides of the signal region. The width of the upper part is chosen to be the same as the width of the lower part, which is half size of the signal region at the corresponding large- $R$  jet  $p_T$  point. From MC background samples, the number of background event yield in side-band region is similar to the background event yield in the signal region.

Figure 4.31 shows the comparison of the  $m_{J\gamma}$  distribution for MC background events in the side-band region and in the signal region for the single  $b$ -tagged and double  $b$ -tagged categories, respectively. For events in the side-band region, they are required to pass all the same selection criteria as the signal region, except for the large- $R$  jet mass optimization selection.

The reason to choose large- $R$  jet mass selection is that this analysis is searching for the heavy resonance, whose resonance mass is much heavier than the mass of the Higgs boson. When reconstructing the Jet+gamma system, the impact from the large- $R$  jet mass is much smaller



(a)

Figure 4.29: large- $R$  jet mass windows(central area between red curve) and side-band boundaries(outer area between black and blue area) as functions of large- $R$  jet  $p_T$ . Area between red and black curves is a 5GeV gap between signal region and side-band region.

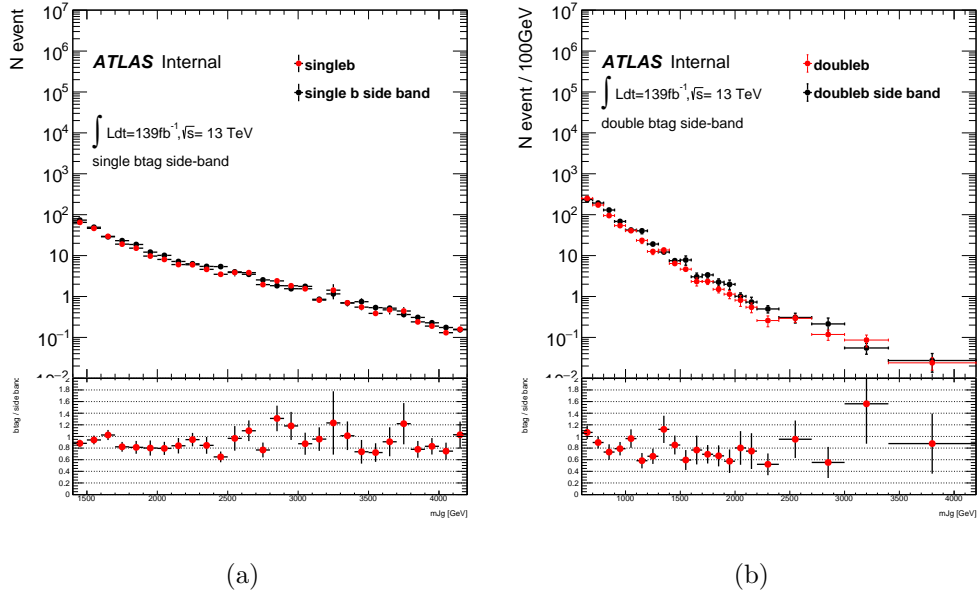


Figure 4.31: Comparison of  $m_{J\gamma}$  distributions for MC simulated events in (a) single  $b$ -tagged and (b) double  $b$ -tag signal and side-band regions. Number of background events in side-band and signal regions are in the same order and compatible.

compared with the large- $R$  jet momentum. So that the difference of large- $R$  jet mass between the signal region and side-band region won't affect much on the final invariant mass  $m_{J\gamma}$  distribution.

#### 4.6.3.2 Untag region

For the  $b$ -tagged selection, it defines two signal regions: double  $b$ -tagged category, corresponding to two CoM subjets passing the  $b$ -tagged selection; single  $b$ -tagged category, corresponding to only one CoM subjet passing the  $b$ -tagged selection. Instead of using the double  $b$ -tagged or single  $b$ -tagged category, the un-tagged category is used for the control region to reduce the potential signal leaking from the signal region to the control region. In order to further suppress the potential signal leaking from the signal region to the control region, a looser  $b$ -tagged selection cut value, 0.27, corresponding to 85 % overall signal efficiency in Graviton sample, is used to define the un-tagged events, whose two CoM subjets fail this looser  $b$ -tagged selection. Note that on top of the  $b$ -tagged selection, the  $p_T$  optimization is applied separately for the two signal region. So to better mimic the kinematic distributions of events in the signal region, the  $p_T$  optimization for double  $b$ -tagged and single  $b$ -tagged is also applied on the un-tagged events and two un-tagged categories are defined: double b-un-tagged and single b-un-tagged. Events in double (single) b-un-tagged category pass all the selection criteria in the double(single)  $b$ -tagged category except for the  $b$ -tagging selection for the CoM subjets.

Figure 4.33 shows the comparison of the  $m_{J\gamma}$  distribution for MC background events in the un-tagged region and in the signal region for the single  $b$ -tagged and double  $b$ -tagged categories, respectively. For events in the un-tagged region, they are required to pass all the same selection criteria as the signal region, except for the  $b$ -tagging selection criteria. From the MC background samples, the number of background events in the un-tagged region is around 10 times more than the ones in the single  $b$ -tagged signal region, and 100 times more than the ones in the double  $b$ -tagged signal region.

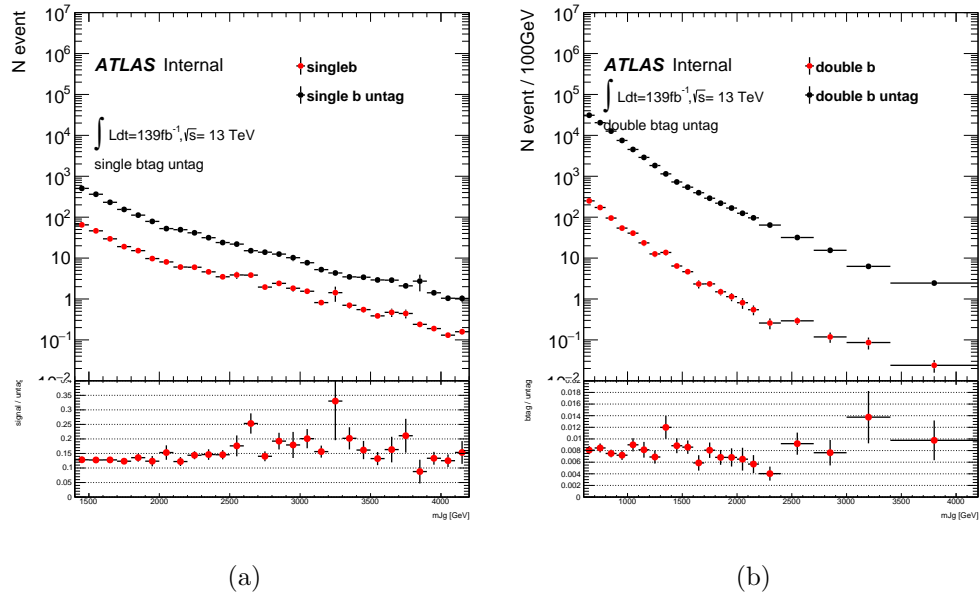


Figure 4.33: Comparison of  $m_{J\gamma}$  distributions for MC simulated events in (a) single  $b$ -tagged and (b) double  $b$ -tag signal and un-tagged regions. Number of background events in un-tagged region is around 10 times more than the ones in the single  $b$ -tagged signal region, and 100 times more than the ones in double  $b$ -tagged signal region. Good shape agreements observed between signal and un-tagged regions.

#### 4.6.3.3 Control region definition

MC study shows that the potential signal leaking in the large- $R$  jet mass side-band region and the un-tagged category may not be negligible. So in this analysis, the control regions are defined as the un-tagged events in the large- $R$  jet mass side-band which pass all the other selection used to define the signal region. Figure 4.35 shows the relationship between the signal region and the control region. Since there are two single regions, and the photon and large- $R$  jet  $p_T$  optimization for these two signal regions are different, so two different control regions are defined separately using the corresponding photon and large- $R$  jet  $p_T$  optimization. Totally there are four regions in this analysis, two signal regions and two control regions:

- single  $b$ -tagged signal region  $\Rightarrow$  single  $b$ -tagged control region
- double  $b$ -tagged signal region  $\Rightarrow$  double  $b$ -tagged control region

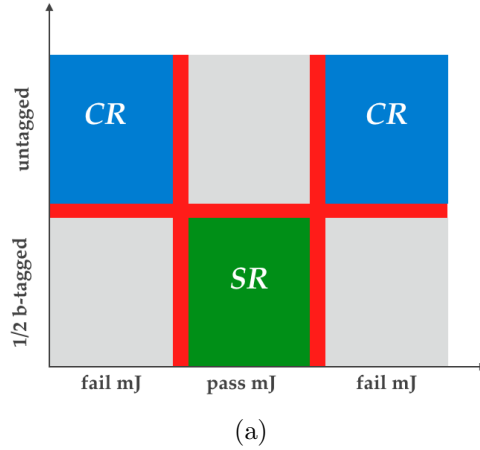


Figure 4.35: Signal region (SR) and control region (CR) definitions. Green area is the signal region whose events pass the large- $R$  jet mass optimization and the  $b$ -tagged selection, while the blue area is the control region whose events fall into large- $R$  jet mass side-band region and fail the looser  $b$ -tagging selection criteria. The red vertical area represents the 5 GeV gap between signal region and large- $R$  jet mass side-band, and the red horizontal line represents the difference in the  $b$ -tagging selection criteria.

Comparison of several kinematic distributions between data and MC background samples in the control regions are shown in Figure 4.37, 4.39. In general, the data distribution agrees with the MC background distribution very well.

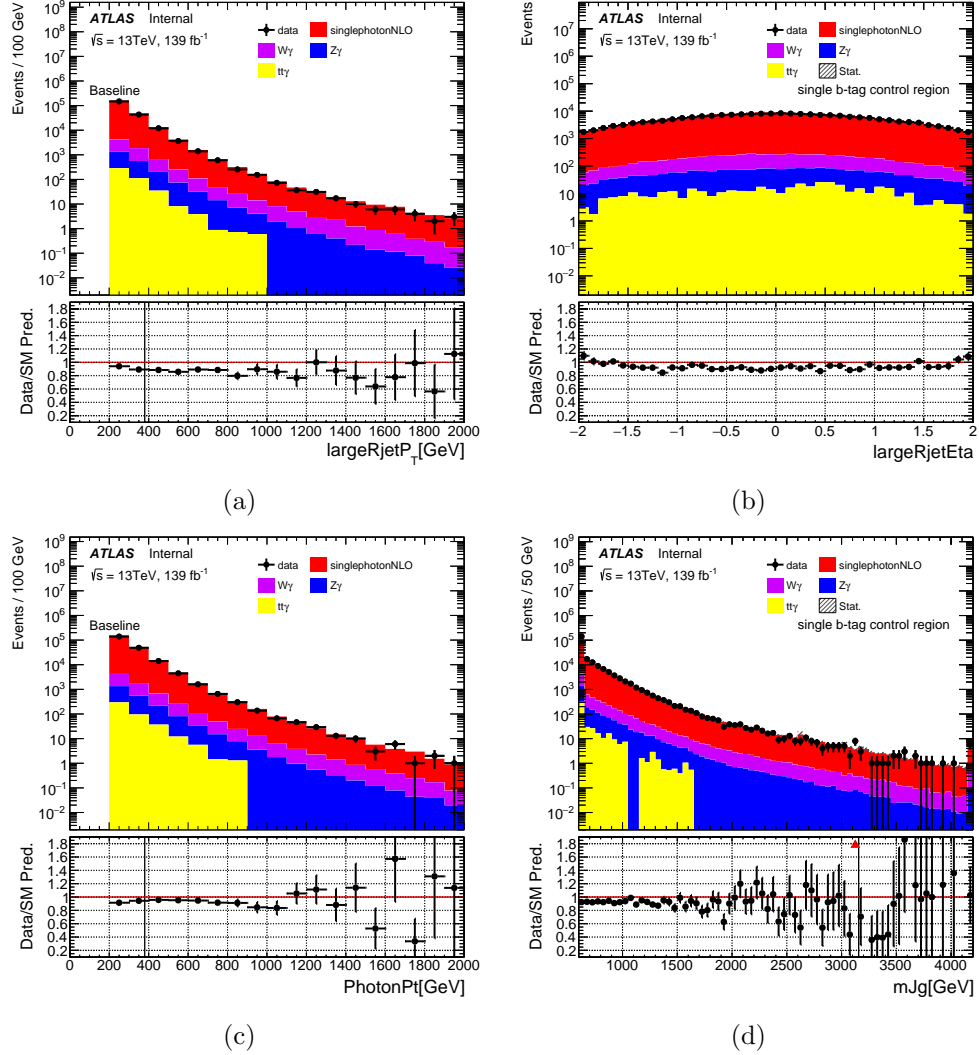


Figure 4.37: Control region single  $b$ -tagged data/MC comparison for (a) large- $R$  jet  $p_T$ , (b) large- $R$  jet  $\eta$ , (c) photon  $p_T$  and (d) invariant mass of large- $R$  jet and photon.

Figure 4.41 shows the comparison of  $m_{J\gamma}$  distribution in the signal region and the control region with MC background samples. The event yields in the control regions are scale to the

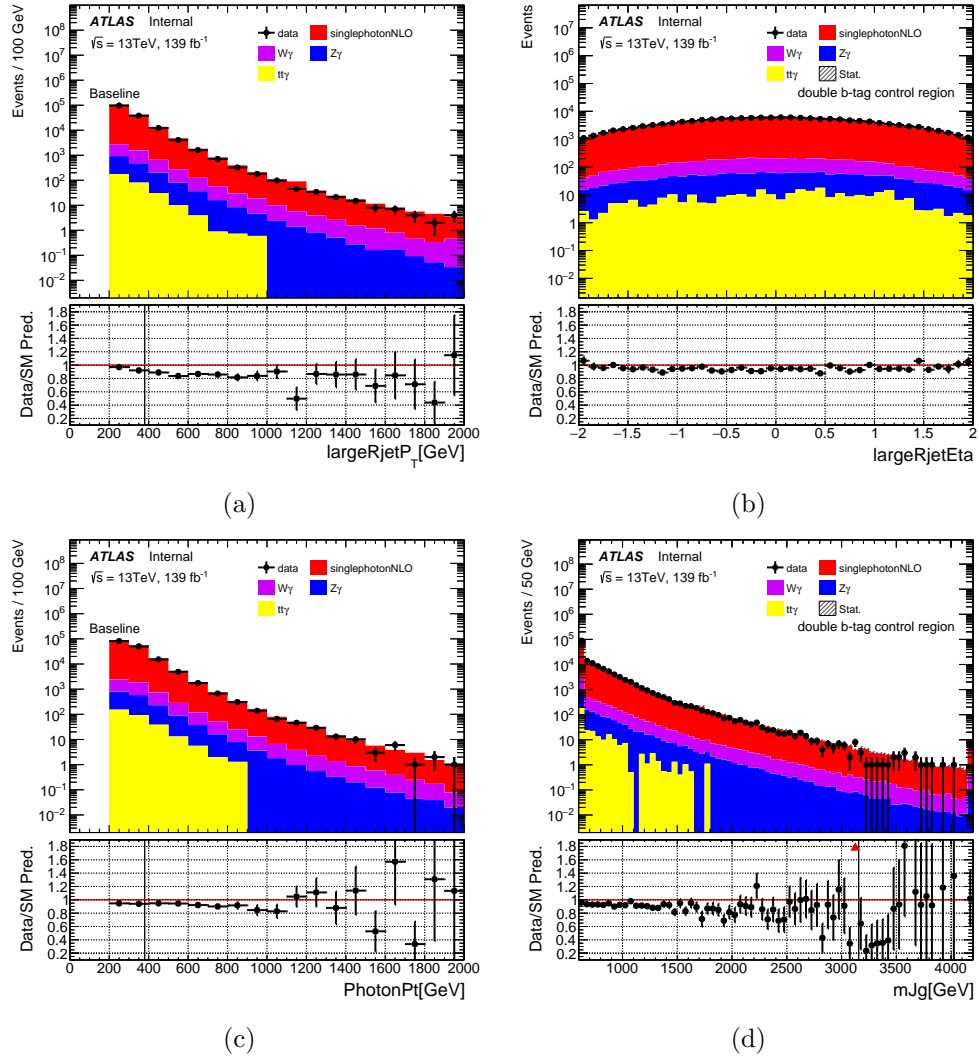


Figure 4.39: Control region double  $b$ -tagged data/MC comparison for (a) large- $R$  jet  $p_T$ , (b) large- $R$  jet  $\eta$ , (c) photon  $p_T$  and (d) invariant mass of large- $R$  jet and photon.



signal region. The  $m_{J\gamma}$  distribution in the signal region is similar to the distribution in the control region, for single  $b$ -tagged, the overall ratio is closed to 1, and for double  $b$ -tagged, the ratio decreases in the high  $m_{J\gamma}$  region. A second-order polynomial function is fitted to the ratio of two distributions to correct the difference between the signal region and the control region. This correction is then applied to control region data events for the  $F$ -test study in the next Section 4.6.4. The event yields in both control regions are almost the same, and are around ten times of that in single-btag signal region and one hundred times of in double-btag signal region. At the same time the signal efficiencies for the control regions are smaller than the signal efficiencies for the signal regions, so that the control region is pure enough for the background study.

To use the data events in the control region for the background model study, the  $m_{J\gamma}$  distribution for data events in the control region needs to be similar to the signal region. To prove this, first, Figure 4.37, 4.39 shows the good agreement between the  $m_{J\gamma}$  distribution for MC background samples and data, so that MC background sample can be used to study the difference between the control region and signal region for data events. Second, Figure 4.41 shows the agreement between the  $m_{J\gamma}$  distribution for MC background samples in the signal region and the control region. The variation, from the bottom ratio plots, is taken into account as a correction factor, which is parametrized using a second-order polynomial function. In the end, the fitted second-order polynomial function is applied to reweight the data distribution in the control regions to correct this variation between the control region and the signal region.

#### 4.6.4 F-test study for background model

To estimate the ability of the background model defined in Equation 4.4, data events in the control regions are used to study the performance of the fitting with the background model. As mentioned in Section 4.6.2, it is free to choose the arbitrary order of the background model. To determine the optimal order for the background model, this analysis applies the F-test [91], which is usually used to compare different statistical models.

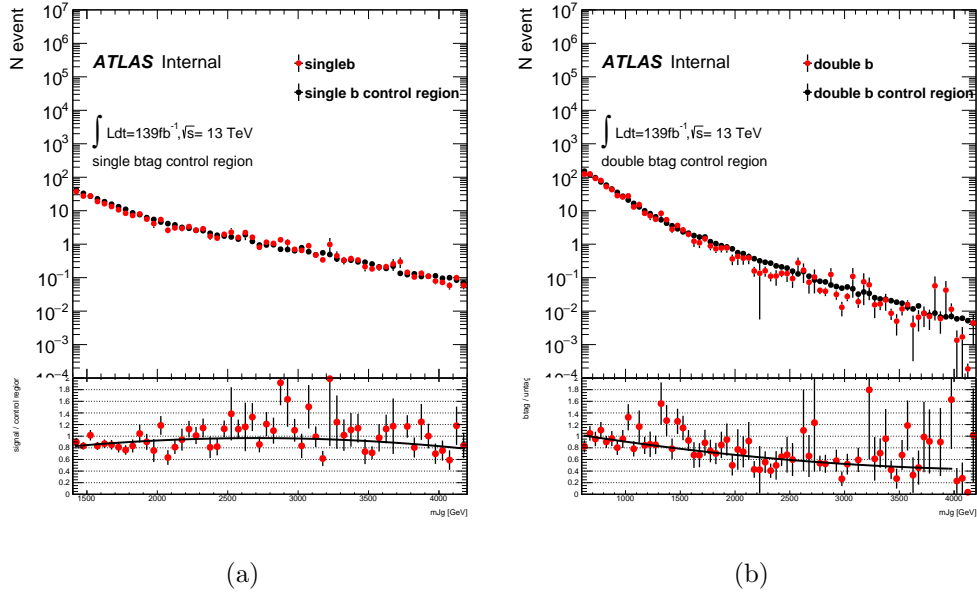


Figure 4.41: The comparison of the  $m_{J\gamma}$  distributions for the MC simulated events in the signal region and control regions and their ratio plot. The total number of events in the control region is scaled to be the same as the one in the signal region. A second-order polynomial function is used to fitted to the ratio plots.

This F-test is based on the  $\chi^2$  values from the fitting and the number of degrees of freedom of the fitting. Consider two functions with different number of freedom, for example, the  $2^{th}$  order and  $3^{th}$  order background function in this analysis. With more parameters the fitting result will always be better, but this F-test can show whether there is significantly improvement for including more free parameters in the function. It builds a F-statistic variable,  $F_{1,2}$ , based on the  $\chi^2$  value from the fitting using two functions  $f_1$ ,  $f_2$ , which have different degrees of freedom:

$$F_{1,2} = \frac{(\chi_1^2 - \chi_2^2)/(p_2 - p_1)}{\chi_2^2/(N_{bin} - p_2)} \quad (4.5)$$

where  $\chi_1^2$  and  $\chi_2^2$  are the  $\chi^2$  value for these two functions,  $N_{bin}$  is the number of bins for the  $\chi^2$  value calculation (the fitting is done by minimizing the unbinned likelihood value).  $p_1$  and  $p_2$  are the number of degrees of freedom for these two functions, so  $p_1 = 2$  and  $p_2 = 3$  for  $2^{th}$  order and  $3^{th}$  order background function.  $p_2$  should be chosen to be larger than  $p_1$ . The F-statistic  $F_{1,2}$  follows a *Fisher* distribution:

$$\mathcal{F}(F|p_2 - p_1, n - p_2) \quad (4.6)$$

If function  $f_2$  can fit the  $m_{J\gamma}$  significantly better than function  $f_1$ ,  $F_{1,2}$  will be a large number, and the corresponding p value  $P(F > F_{1,2})$  will be a very small number. 0.1 is chosen to be the threshold.

In this analysis, the minimum number of order is 2, an additional parameter will be included if the p value from F-test is smaller than the threshold. The expected number of background events from MC background sample is around 10 times as the expected number of background events in single  $b$ -tagged category and 100 times as the expected number of background events in double  $b$ -tagged category. When doing the F-test in single  $b$ -tagged category, all the data events in single  $b$ -tagged control region is used. While for double  $b$ -tagged, to be consistent with single  $b$ -tagged, only 10% of the data events in double  $b$ -tagged control region are picked randomly and used for the F-test, so that for both single  $b$ -tagged and double  $b$ -tagged the F-test is done with 10 times of control region data events compared with the signal region.

Table 4.3 shows the  $F$  value and corresponding  $P$  value for the  $F$ -test for different number of shape parameters. Results show that for both the single and double  $b$ -tagged categories,  $3^{th}$  order background function can significantly improve the fitting performance compared with the  $2^{th}$  order background function, and additional parameters are not needed.

Table 4.3:  $F$ -test results with control region data events. 3-parameters function provides the best fit performance for both single and double  $b$ -tagged categories.

	2-para. vs 3-para.	3-para, vs 4-para.
control region single $b$ -tagged $F$ value	3.24	0.12
control region single $b$ -tagged $P$ value	0.086	0.728
control region double $b$ -tagged $F$ value	19.05	-1.91
control region double $b$ -tagged $P$ value	$3 \cdot 10^{-4}$	1

The data  $m_{J\gamma}$  distributions in the control regions and the fitting results with a  $3^{th}$  order background function are shown in Fig. 4.43.

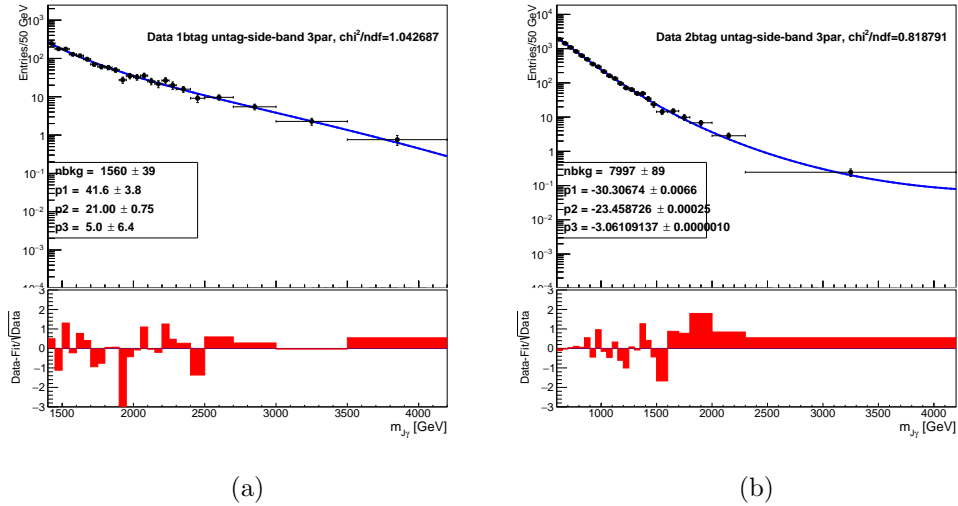


Figure 4.43: Background fits to the data  $m_{J\gamma}$  mass distributions in the control region. The bottom pad shows the significance, which is the variation between fitted function and the data distribution divided by the uncertainty of data events in that bin.

## 4.7 Systematic uncertainty

Systematic uncertainties are included in the limit calculation in Section 5.2.2. There are three different kinds of systematic uncertainties: systematic uncertainties from the detector modeling and MC sample modeling, in Section 4.7.1; theoretical systematic uncertainty, in Section 4.7.2; systematic uncertainty from background modeling, in Section 4.7.3. The systematic uncertainties from detector and MC modeling will affect the shape and yield of the signal  $m_{J\gamma}$  distribution. Theoretical systematic uncertainties will affect the yield of the signal events. Since our background model is an analytical function, and the free parameters are determined with the fitting using signal region data, the systematic uncertainties from detector modeling and MC sample modeling won't affect the background model. The systematic uncertainties from background modeling are estimated by the spurious signal result and will affect the fitting result of signal yield. This section will introduce these systematic uncertainties about how to estimate and how they affect the signal and background model.

### 4.7.1 Detector modeling systematic uncertainties

The impact of systematic uncertainties from detector modeling can affect the shape of the signal  $m_{J\gamma}$  distribution and also the signal efficiency, which is used in the limit calculation in Section 5.2.2. The systematic uncertainties from both detector effects and MC modeling will be introduced in this section. From the detector modeling, the physics objects used in this analysis includes photon, in Section 4.7.1.1, large- $R$  jet, in Section 4.7.1.2. The systematic uncertainty for  $b$ -tagging will be shown in Section 4.7.1.3. The other two systematic uncertainties related to the detector are the systematic uncertainties for luminosity in Section 4.7.1.4 and for pile-up in Section 4.7.1.5.

#### 4.7.1.1 Systematic uncertainty for photon

Systematic uncertainties related to photon includes uncertainties from photon energy resolution, photon energy scale [92] , photon ID efficiency scale factor and photon EM calorimeter isolation scale factor [93]

In ATLAS, Egamma group provides a simplified scheme for estimating EM energy scale and resolution uncertainties using the tool called: `EgammaCalibrationAndSmearingTool`. With this simplification only 2 systematic variations are provided: one for the scale, one for the resolution. In order to account for the ID efficiency differences between data and MC, Egamma group provides a tool called `PhotonEfficiencyCorrectionTool` to retrieve the scale factors. Similar as photon identification scale factor and corresponding uncertainties, isolation selection can also introduce different efficiencies in data and simulated events, and the efficiency corrections are also retrieved with `PhotonEfficiencyCorrectionTool` with systematic uncertainties.

#### 4.7.1.2 Systematic uncertainty for large- $R$ jet

The large- $R$  jet energy scale (JES) and resolution uncertainties are included following the prescription of the jet substructure group included in the `JetUncertainties` package. The uncertainty on the mass and  $p_T$  of large- $R$  jet are evaluated by comparing the ratio of calorimeter-based to track-based measurements in di-jet data and simulation. There are three different jet uncertainty configurations, and the one used in this analysis is “R10\_CategoryReduction.config”, which is recommended for typical precision results and has 30 JES uncertainty components.

The resolutions are conservative and are obtained assigning absolute 2 % for  $p_T$  resolution uncertainty, relative 20 % for mass resolution uncertainty and 15 % for any substructure resolution uncertainties [94]. The resolution is determined by fitting with a Gaussian of the  $O_{reco}/O_{truth}$  distribution and taking the width of this Gaussian (interquartile range (IQR) in case of low statistics). The nominal MC mass resolution  $\sigma_{nominal}$  to be smeared was parametrized in terms of  $p_T$ .

#### 4.7.1.3 Systematic uncertainty for $b$ -tagging

The systematic uncertainties associated to the CoM subjet  $b$ -tagging are applied using the official prescriptions. The uncertainties are derived from CoM  $b$ -jet in a semi-leptonic decay of  $t\bar{t}$  production, where the hadronic decay of the top-quark is reconstructed as a large- $R$  jet. Thanks to a large cross-section of  $t\bar{t}$ , an enriched CoM  $b$ -jet production is obtained through  $t \rightarrow bW(\rightarrow qq')$ . The calibration of CoM  $b$ -jets is performed as a function of CoM subjet  $p_T$  in 5  $p_T$  bins: [0, 125, 175, 225, 275, 750] GeV. For CoM  $b$ -jets beyond the measured  $p_T$  range, the scale factors from the last measured bin is used with an extrapolation of uncertainties estimated with MC simulation. Working points of  $b$ -jet tagging efficiency at 60 %, 70 %, 77 % and 85 % are performed. Systematic uncertainties due to the  $t\bar{t}$  modeling, large- $R$  jet energy scale and resolution, large- $R$  jet mass resolution as well as other uncertainties related to small backgrounds are estimated to be 4–6 % in total.

#### 4.7.1.4 Systematic uncertainty for luminosity

The uncertainty on the integrated luminosity for the full run 2 dataset is 1.7 % [95]. The luminosity uncertainty is applied to the signal samples.

#### 4.7.1.5 Systematic uncertainty for pile-up

The systematic uncertainty from pile-up is estimated using `PileupRewightingTool` [96]. This `PileupRewightingTool` will define a scale factor to correct for differences between Monte Carlo and Data and the corresponding systematic uncertainty.

#### 4.7.1.6 Effects of the systematic uncertainties from detector and MC sample modeling

Table 4.4 gives the summary of the systematic uncertainty. It shows the components for each systematic uncertainties and the corresponding name in the tools.

Table 4.4: Qualitative summary of the systematic uncertainties included in this analysis.

Source	Description	Systematic Uncertainty Name
Luminosity	Luminosity measurement	lumi
Pile-up	Pile-up measurement	PRW_DATASF
Photons	Photon energy resolution	EG_RESOLUTION_ALL
Photons	Photon energy scale	EG_SCALE_ALL
Photons	ID efficiency scale factors for photons	PH_EFF_ID_Uncertainty
Photons	Calorimeter isolation scale factors for photons	PH_Iso_DDonoff
large- $R$ Jets	$p_T$ scale and mass scale	FATJET_CR_JET_CombMass_Baseline
large- $R$ Jets	$p_T$ scale and mass scale	FATJET_CR_JET_CombMass_modeling
large- $R$ Jets	$p_T$ scale and mass scale	FATJET_CR_JET_CombMass_TotalStat
large- $R$ Jets	$p_T$ scale and mass scale	FATJET_CR_JET_CombMass_Tracking1
large- $R$ Jets	$p_T$ scale and mass scale	FATJET_CR_JET_CombMass_Tracking2
large- $R$ Jets	$p_T$ scale and mass scale	FATJET_CR_JET_CombMass_Tracking3
large- $R$ Jets	$p_T$ scale and mass scale	FATJET_CR_JET_EffectiveNP_R10_Detector1
large- $R$ Jets	$p_T$ scale and mass scale	FATJET_CR_JET_EffectiveNP_R10_Detector2
large- $R$ Jets	$p_T$ scale and mass scale	FATJET_CR_JET_EffectiveNP_R10_Mixed1
large- $R$ Jets	$p_T$ scale and mass scale	FATJET_CR_JET_EffectiveNP_R10_Mixed2
large- $R$ Jets	$p_T$ scale and mass scale	FATJET_CR_JET_EffectiveNP_R10_Mixed3
large- $R$ Jets	$p_T$ scale and mass scale	FATJET_CR_JET_EffectiveNP_R10_Mixed4
large- $R$ Jets	$p_T$ scale and mass scale	FATJET_CR_JET_EffectiveNP_R10_modeling1
large- $R$ Jets	$p_T$ scale and mass scale	FATJET_CR_JET_EffectiveNP_R10_modeling2
large- $R$ Jets	$p_T$ scale and mass scale	FATJET_CR_JET_EffectiveNP_R10_modeling3
large- $R$ Jets	$p_T$ scale and mass scale	FATJET_CR_JET_EffectiveNP_R10_modeling4
large- $R$ Jets	$p_T$ scale and mass scale	FATJET_CR_JET_EffectiveNP_R10_Statistical1
large- $R$ Jets	$p_T$ scale and mass scale	FATJET_CR_JET_EffectiveNP_R10_Statistical2
large- $R$ Jets	$p_T$ scale and mass scale	FATJET_CR_JET_EffectiveNP_R10_Statistical3
large- $R$ Jets	$p_T$ scale and mass scale	FATJET_CR_JET_EffectiveNP_R10_Statistical4
large- $R$ Jets	$p_T$ scale and mass scale	FATJET_CR_JET_EffectiveNP_R10_Statistical5
large- $R$ Jets	$p_T$ scale and mass scale	FATJET_CR_JET_EffectiveNP_R10_Statistical6
large- $R$ Jets	$p_T$ scale and mass scale	FATJET_CR_JET_EtaIntercalibration_modeling
large- $R$ Jets	$p_T$ scale and mass scale	FATJET_CR_JET_EtaIntercalibration_NonClosure_2018data
large- $R$ Jets	$p_T$ scale and mass scale	FATJET_CR_JET_EtaIntercalibration_R10_TotalStat
large- $R$ Jets	$p_T$ scale and mass scale	FATJET_CR_JET_Flavor_Composition
large- $R$ Jets	$p_T$ scale and mass scale	FATJET_CR_JET_Flavor_Response
large- $R$ Jets	$p_T$ scale and mass scale	FATJET_CR_JET_LargeR_TopologyUncertainty_top
large- $R$ Jets	$p_T$ scale and mass scale	FATJET_CR_JET_LargeR_TopologyUncertainty_V
large- $R$ Jets	$p_T$ scale and mass scale	FATJET_CR_JET_SingleParticle_HighPt
large- $R$ Jets	$p_T$ resolution	FATJET_JER
large- $R$ Jets	Mass resolution	FATJET_JMR
$b$ -tagging	Flavor tagging scale factors	FT_EFF_Eigen_B0
$b$ -tagging	Flavor tagging scale factors	FT_EFF_Eigen_B1
$b$ -tagging	Flavor tagging scale factors	FT_EFF_Eigen_B2
$b$ -tagging	Flavor tagging scale factors	FT_EFF_Eigen_B3
$b$ -tagging	Flavor tagging scale factors	FT_EFF_Eigen_B4



The impact on the signal  $m_{J\gamma}$  distribution at resonance mass  $H\gamma = 2$  TeV from these systematic uncertainties are shown in appendix in Figure .2, .4 and .6 for single  $b$ -tagged category and in Figure .8, .10 and .12 for double  $b$ -tagged category

For the signal model in Section 4.5.1, the systematic uncertainties variation will affect the fitting result of the value of each parameter. From the MC study, the impact from the systematic uncertainties variation on two of the parameters, signal peak position and the width of  $m_{J\gamma}$  distribution, significantly larger than the others. At the same time, the variation from these two parameters will affect the final limit calculation. To simplify the analysis, instead of fitting the signal distribution for each systematic uncertainties variation, for the signal  $m_{J\gamma}$  distribution for each systematic uncertainties variation, the peak position is found as the position of the maximum point of the distribution, the width variation is quantified as the variation of the standard deviation of the distribution.

Besides the parameters in the signal model, the systematic uncertainties will also affect the signal efficiency, which is directly related to the yield calculation in the limit calculation.

In summary, to quantify the impact from systematic uncertainties, the systematic variations affect signal modeling through changing the signal selection efficiency, the fitted peak position and the width of the  $m_{J\gamma}$  distribution. A summary of these impacts on the signal  $m_{J\gamma}$  distribution at resonance mass  $H\gamma = 2$  TeV are shown in Table 4.5 and 4.6. In the table,  $\Delta$  means the relative differences, which is (Nominal-Systematic)/Nominal.

#### 4.7.2 Theoretical systematic uncertainties

There are three sources for the theoretical systematic uncertainties:

- Choices of parton distribution function (PDF) set.
- Choice of the renormalization ( $\mu_R$ ) and factorization ( $\mu_F$ ) factor.
- Choices of parton shower modeling.

Table 4.5: Breakdown of systematics effects. The systematic variations on  $X \rightarrow H + \gamma$  signal modeling effecting the signal selection efficiency, the fitted peak position and the width of the  $m_{J\gamma}$  distribution. The mass of the signal resonance mass here is 2000 GeV.

Systematic Uncertainties	$m_X = 2000 \text{ GeV}$					
	double $b$ -tagging			single $b$ -tagging		
	$\Delta\epsilon$ (%)	$\Delta \text{ peak}$ (%)	$\Delta\sigma$ (%)	$\Delta\epsilon$ (%)	$\Delta \text{ peak}$ (%)	$\Delta\sigma$ (%)
EG_RESOLUTION_ALL_1down	-0.0	-0.4	-0.4	-0.0	0.5	-0.7
EG_RESOLUTION_ALL_1up	-0.0	-0.4	0.9	0.1	-0.1	1.0
EG_SCALE_ALL_1down	-0.2	-1.1	-0.1	-2.4	0.2	-2.4
EG_SCALE_ALL_1up	0.1	0.3	2.1	0.5	1.7	2.0
FATJET_JER_1up	0.0	-0.8	3.2	0.1	-0.1	3.6
FATJET_JMR_1up	-30.2	0.0	2.6	-28.7	-0.1	2.5
FATJET_CR_JET_CombMass_Baseline_1down	-1.3	0.0	-2.1	-1.5	0.0	-1.8
FATJET_CR_JET_CombMass_Baseline_1up	1.2	0.0	1.9	1.5	0.0	1.9
FATJET_CR_JET_CombMass_Modelling_1down	-8.3	0.0	-7.0	-9.9	1.0	-3.4
FATJET_CR_JET_CombMass_Modelling_1up	0.2	0.0	6.8	2.3	0.0	4.4
FATJET_CR_JET_CombMass_TotalStat_1down	0.0	0.0	-0.1	-0.0	0.0	-0.0
FATJET_CR_JET_CombMass_TotalStat_1up	0.0	0.0	0.1	0.0	0.0	0.0
FATJET_CR_JET_CombMass_Tracking1_1down	-0.6	0.0	-1.5	-0.6	0.0	-0.6
FATJET_CR_JET_CombMass_Tracking1_1up	0.6	0.0	1.4	0.7	0.0	0.9
FATJET_CR_JET_CombMass_Tracking2_1down	-1.2	0.0	-1.9	-1.4	0.0	-1.0
FATJET_CR_JET_CombMass_Tracking2_1up	1.0	0.0	1.9	1.4	0.0	1.3
FATJET_CR_JET_CombMass_Tracking3_1down	-0.7	0.0	-1.5	-0.8	0.0	-0.7
FATJET_CR_JET_CombMass_Tracking3_1up	0.7	0.0	1.4	1.0	0.0	1.0
FATJET_CR_JET_EffectiveNP_R10_Detector1_1down	-0.0	0.0	-0.2	-0.0	0.0	-0.1
FATJET_CR_JET_EffectiveNP_R10_Detector1_1up	0.1	0.0	0.1	0.0	0.0	0.1
FATJET_CR_JET_EffectiveNP_R10_Detector2_1down	0.0	0.0	-0.1	-0.0	0.0	-0.0
FATJET_CR_JET_EffectiveNP_R10_Detector2_1up	0.0	0.0	0.0	0.0	0.0	0.0
FATJET_CR_JET_EffectiveNP_R10_Mixed1_1down	-0.4	0.0	-1.2	-0.3	0.0	-0.8
FATJET_CR_JET_EffectiveNP_R10_Mixed1_1up	0.5	0.0	1.4	0.5	0.5	1.0
FATJET_CR_JET_EffectiveNP_R10_Mixed2_1down	0.2	0.0	0.4	0.2	0.5	0.2
FATJET_CR_JET_EffectiveNP_R10_Mixed2_1up	-0.1	0.0	-0.3	-0.2	0.0	-0.2
FATJET_CR_JET_EffectiveNP_R10_Mixed3_1down	0.0	0.0	0.2	0.0	0.0	0.2
FATJET_CR_JET_EffectiveNP_R10_Mixed3_1up	0.0	0.0	-0.2	-0.0	0.0	-0.2
FATJET_CR_JET_EffectiveNP_R10_Mixed4_1down	-0.0	0.0	-0.1	-0.0	0.0	-0.0
FATJET_CR_JET_EffectiveNP_R10_Mixed4_1up	0.0	0.0	0.0	0.0	0.0	0.0
FATJET_CR_JET_EffectiveNP_R10_Modelling1_1down	-0.4	0.0	-1.3	-0.3	0.0	-0.8
FATJET_CR_JET_EffectiveNP_R10_Modelling1_1up	0.5	0.0	1.3	0.5	0.5	1.0
FATJET_CR_JET_EffectiveNP_R10_Modelling2_1down	0.0	0.0	-0.1	0.0	0.0	-0.1
FATJET_CR_JET_EffectiveNP_R10_Modelling2_1up	-0.0	0.0	0.1	0.0	0.0	0.2
FATJET_CR_JET_EffectiveNP_R10_Modelling3_1down	0.2	0.0	0.5	0.2	0.5	0.3
FATJET_CR_JET_EffectiveNP_R10_Modelling3_1up	-0.1	0.5	-0.4	-0.2	0.0	-0.2
FATJET_CR_JET_EffectiveNP_R10_Modelling4_1down	-0.0	0.0	-0.1	-0.0	0.0	-0.1
FATJET_CR_JET_EffectiveNP_R10_Modelling4_1up	0.1	0.0	0.2	0.0	0.0	0.1
FATJET_CR_JET_EffectiveNP_R10_Statistical1_1down	-0.1	0.0	-0.3	-0.1	0.0	-0.2

Table 4.6: Breakdown of systematics effects. The systematic variations on  $X \rightarrow H + \gamma$  signal modeling effecting the signal selection efficiency, the fitted peak position and the width of the  $m_{J\gamma}$  distribution. The mass of the signal resonance mass here is 2000 GeV.

Systematic Uncertainties	$m_X = 2000 \text{ GeV}$					
	double $b$ -tagging			single $b$ -tagging		
	$\Delta\epsilon$ (%)	$\Delta \text{ peak}$ (%)	$\Delta\sigma$ (%)	$\Delta\epsilon$ (%)	$\Delta \text{ peak}$ (%)	$\Delta\sigma$ (%)
FATJET_CR_JET_EffectiveNP_R10_Statistical1_1up	0.1	0.5	0.3	0.1	0.0	0.3
FATJET_CR_JET_EffectiveNP_R10_Statistical2_1down	0.0	0.0	-0.0	0.0	0.0	0.0
FATJET_CR_JET_EffectiveNP_R10_Statistical2_1up	-0.0	0.0	-0.0	-0.0	0.0	0.0
FATJET_CR_JET_EffectiveNP_R10_Statistical3_1down	0.0	0.0	0.2	0.1	0.0	0.1
FATJET_CR_JET_EffectiveNP_R10_Statistical3_1up	-0.0	0.0	-0.2	-0.1	0.0	-0.1
FATJET_CR_JET_EffectiveNP_R10_Statistical4_1down	-0.0	0.0	-0.0	-0.0	0.0	0.0
FATJET_CR_JET_EffectiveNP_R10_Statistical4_1up	0.0	0.0	0.0	0.0	0.0	-0.0
FATJET_CR_JET_EffectiveNP_R10_Statistical5_1down	-0.0	0.0	-0.1	-0.0	0.0	-0.0
FATJET_CR_JET_EffectiveNP_R10_Statistical5_1up	0.0	0.0	0.0	0.0	0.0	-0.0
FATJET_CR_JET_EffectiveNP_R10_Statistical6_1down	-0.0	0.0	-0.1	-0.0	0.0	-0.0
FATJET_CR_JET_EffectiveNP_R10_Statistical6_1up	0.0	0.0	0.1	0.0	0.0	0.1
FATJET_CR_JET_EtaIntercalibration_Modelling_1down	-0.2	0.0	-0.7	-0.2	0.0	-0.3
FATJET_CR_JET_EtaIntercalibration_Modelling_1up	0.2	0.0	0.6	0.1	0.5	0.5
FATJET_CR_JET_EtaIntercalibration_NonClosure_2018data_1down	-0.1	0.0	-0.2	-0.0	0.0	-0.1
FATJET_CR_JET_EtaIntercalibration_NonClosure_2018data_1up	0.1	0.0	0.0	-0.0	0.0	0.1
FATJET_CR_JET_EtaIntercalibration_R10_TotalStat_1down	-0.0	0.0	-0.2	-0.0	0.0	-0.2
FATJET_CR_JET_EtaIntercalibration_R10_TotalStat_1up	0.1	0.0	0.2	0.1	0.0	0.1
FATJET_CR_JET_Flavor_Composition_1down	-0.2	0.0	-0.7	-0.3	0.5	-0.6
FATJET_CR_JET_Flavor_Composition_1up	0.3	0.5	1.0	0.3	0.5	0.7
FATJET_CR_JET_Flavor_Response_1down	-0.1	0.5	-0.5	-0.2	0.0	-0.3
FATJET_CR_JET_Flavor_Response_1up	0.2	0.0	0.7	0.2	0.5	0.4
FATJET_CR_JET_LargeR_TopologyUncertainty_V_1down	0.0	0.0	-0.0	0.0	0.0	-0.0
FATJET_CR_JET_LargeR_TopologyUncertainty_V_1up	0.0	0.0	-0.0	0.0	0.0	-0.0
FATJET_CR_JET_LargeR_TopologyUncertainty_top_1down	0.0	0.0	-0.0	0.0	0.0	-0.0
FATJET_CR_JET_LargeR_TopologyUncertainty_top_1up	0.0	0.0	-0.0	0.0	0.0	-0.0
FATJET_CR_JET_SingleParticle_HighPt_1down	-0.0	0.0	-0.0	-0.0	0.0	-0.0
FATJET_CR_JET_SingleParticle_HighPt_1up	0.0	0.0	0.0	0.0	0.0	0.0
PH_EFF_ID_Uncertainty_1down	0.0	0.0	0.0	0.0	0.0	0.0
PH_EFF_ID_Uncertainty_1up	0.0	0.0	0.0	0.0	0.0	0.0
PH_EFF_ISO_Uncertainty_1down	0.0	0.0	0.0	0.0	0.0	0.0
PH_EFF_ISO_Uncertainty_1up	0.0	0.0	0.0	0.0	0.0	0.0
PRW_DATASF_1down	0.1	0.0	-0.1	-0.2	0.3	0.1
PRW_DATASF_1up	0.1	-0.1	0.0	-0.5	0.0	0.0
EFF_Eigen_B_0.down	12.5	0.0	-0.0	-14.5	0.0	-0.3
EFF_Eigen_B_0.up	-11.8	0.0	0.0	12.3	0.0	0.2
EFF_Eigen_B_1.down	3.1	0.0	-0.0	-3.6	0.0	-0.0
EFF_Eigen_B_1.up	-3.1	0.0	0.0	3.5	0.0	0.0
EFF_Eigen_B_2.down	2.6	0.0	-0.0	-3.8	0.0	-0.0
EFF_Eigen_B_2.up	-2.6	0.0	0.0	3.7	0.0	0.0
EFF_Eigen_B_3.down	-1.4	0.0	0.0	1.9	0.0	-0.0
EFF_Eigen_B_3.up	1.4	0.0	-0.0	-2.0	0.0	0.0
EFF_Eigen_B_4.down	0.1	0.0	-0.0	-0.3	0.0	-0.0
EFF_Eigen_B_4.up	-0.1	0.0	0.0	0.3	0.0	0.0

#### 4.7.2.1 PDF uncertainties

The proton parton density function (PDF) is an important part in the MC sample generation. Different PDF set in event generation can have different kinematic distribution and furthermore affect the signal efficiency after the selection. And the variation due to different PDF set is considered as the PDF uncertainties. The MC signal samples are produced by MADGRAPH [97], the event-by-event weight can be calculated by using LHAPDF package [98] as:

$$w = \frac{f'_1(x_1, Q, \text{PID}) \times f'_2(x_2, \mu_F, \text{PID})}{f_1(x_1, Q, \text{PID}) \times f_2(x_2, \mu_F, \text{PID})} \quad (4.7)$$

Where  $f_i, i = 1, 2$  are the nominal PDFs, which is the functions of parton momentum fraction  $x$ , factorization scale  $\mu_F$  and parton types.  $f'_i, i = 1, 2$  are the alternative PDFs. For samples generated with MADGRAPH, the central value of NNPDF set is used as the nominal PDF.

Figure 4.44 shows the PDF uncertainty in the acceptance as a function of the resonance mass.

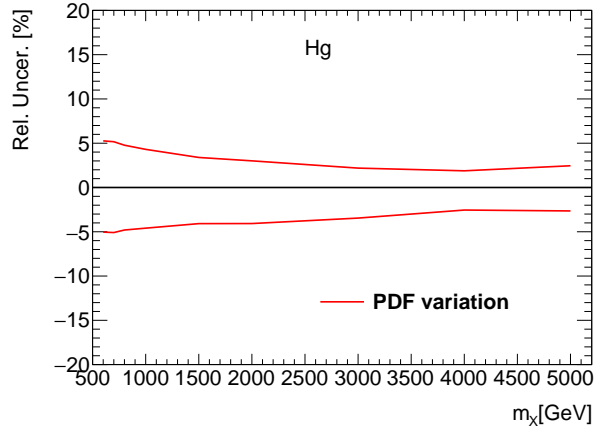


Figure 4.44: PDF uncertainty in the signal efficiency as a function of the resonance mass.

#### 4.7.2.2 QCD scale

The renormalization scale  $\mu_R$  and factorization scale  $\mu_F$  are introduced in perturbative quantum chromodynamic (pQCD) to avoid the ultraviolet and infrared divergence of limited

order QCD calculation. The physics observation should not depend on the value of these two factors, and normally the choices of two parameters are arbitrary. But in pQCD different choices will cause the different cross-section and kinematic predictions for MC samples. To evaluate the effect due to different choice of these two factors, alternative samples with  $\mu_R$  and  $\mu_F$  varying by a factor of 0.5 and 2 separately are produced. In total the combinations of  $\mu_R$  and  $\mu_F$ :  $\{0.5, 1, 2\} \times \{0.5, 1, 2\}$  are available. The systematic uncertainties for these two factors are quantified as the largest signal efficiency variation between the nominal choice and the alternative combinations, the final variation is shown in Figure 4.45

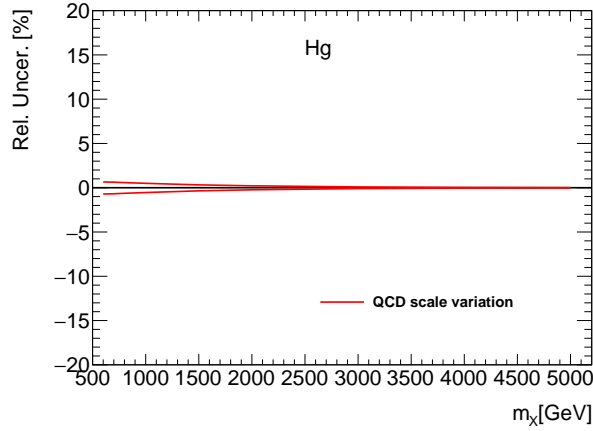


Figure 4.45: QCD scale uncertainty in the signal efficiency as a function of the resonance mass.

#### 4.7.2.3 Parton shower uncertainty

The parton shower simulation in the MC sample depends on the algorithm and parameters in the generator. The parton shower uncertainty is estimated by considering the eigen variations for PYTHIA A14 tunes as the alternative parton shower models. Recommended eigen variations on the parton shower parameters have 5 variations with up and down components for each variation. The acceptance for alternative parton models is compared to the nominal acceptance value. The final uncertainty is calculated as the quadratic sum of the acceptance differences for 5 eigen variations.

Table 4.7: Acceptance difference due to the effect of parton shower for  $m = 1000, 3000, 5000$  GeV.

	1000 GeV	3000 GeV	5000 GeV
Var1	0.12 %, -0.26 %	-0.22 %, -1.00 %	0.26 %, 1.21 %
Var2	0.16 %, 0.04 %	0.85 %, -0.09 %	0.90 %, -1.37 %
Var3a	0.32 %, -0.40 %	0.33 %, -0.60 %	1.26 %, -0.02 %
Var3b	-0.54 %, -0.48 %	-0.88 %, -0.82 %	-0.67 %, 0.21 %
Var3c	-0.70 %, -0.34 %	0.11 %, -0.74 %	0.74 %, -1.01 %

Table 4.7 presents the effect of parton shower on the signal efficiency. The impact on the signal efficiency for different mass point is parametrized using a first order polynomial function.

### 4.7.3 Background modeling systematic uncertainties

In this analysis, the background models are the analytical functions, introduced in Section 4.6.2. In each signal region, there are three parameters to control the shape of the background function, which are determined in the fitting with data samples. However, the background model shape may not be 100 % agreed with the distribution of actual background events in the data, and that will cause bias for the signal+background fitting. To describe this possible bias on the signal+background best fit, the spurious signal test is performed and the corresponding spurious signal uncertainty is introduced in this section, and will be added into the limit calculation in Chapter 5.

The spurious signal is defined as the fake signal events from the signal+background fitting with a background only sample. The data events in the control region are used for the spurious signal test, since the signal leaking in the control region is negligible, more detail in Section 4.6.3. The control region to signal region correction factor is applied for each control region. Since there are much more events in the control region than the signal region, as a factor of 100 compared with double b-tagged signal region and a factor or 10 for single b-tagged signal region, the yield in the control region is scaled to the same number of events in double/single b-tagged signal region to estimate the magnitude of the spurious signal in the signal region. And the number of spurious

signal events equals the number of signal in the signal+background fitting using data events in the control region. Figure 4.47 shows the number of spurious signal events as a function of resonance mass, which is scanned with a step size of 20 GeV. In the limit setting in Chapter 5, the absolute number of spurious signal events is applied as a systematic uncertainty to describe the potential bias between the function shape and the actual background distribution.

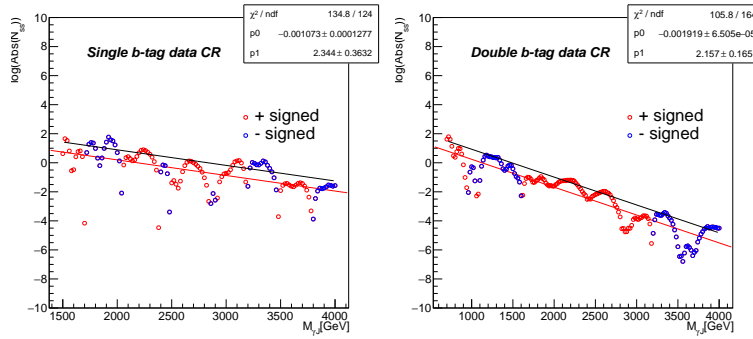


Figure 4.47: The number of spurious signal events, which is from the fitting with signal+background model using data events in (a) single b-tagged control region and (b) double b-tagged control region. The Y-axis is the absolute value of number of spurious signal events, in log scale. The number of spurious signal events distribution are fitted with a straight line, the red line. To cover most of the spurious signal events, the red line is moved up for  $\log_2$  and becomes the black straight line, which is used for the limit calculation.

## CHAPTER 5. ANALYSIS STATISTICAL RESULT

In this section, the statistic analysis will be introduced. The data distribution is shown in Section 5.1. With the signal and background model and the corresponding systematic uncertainties, data events are used to determine whether the signal is observed or not. In this analysis, the data is interpreted with a frequentist analysis. In general, searching for a new phenomenon, which is the signal model in this analysis, is to test the null hypothesis, which is the background only model  $H_0$ , against the alternative signal+background model  $H_1$ . Opposite to the new phenomenon search, for the limit setting it is using signal+background model as  $H_0$  and to be tested against the background only model, denoted as  $H_1$ . If there is no obvious signal evidence (more detail in Section 5.2.1), then the upper limit is set (more detail in Section 5.2.2). First the likelihood function is defined in Section 5.2. With the likelihood function, we can define the hypothesis testing statistic, which is introduced in Section 5.2. For searching for new phenomenon, the sensitivity is defined in Section 5.2.1 to quantify the confidence level of “seeing” the new signal. If no signal is observed, an upper limit is set on the product of the signal production cross-section and its decaying branching fraction, as described in Section 5.2.2.

### 5.1 Data distribution

Figure 5.2 shows the data distributions and background only fit functions in the single b-tagged signal region and double b-tagged signal region. The significance, which is defined as deviation / statistical uncertainty for each bin, is shown at the bottom pad. The data distribution is in good agreement with the fit function.



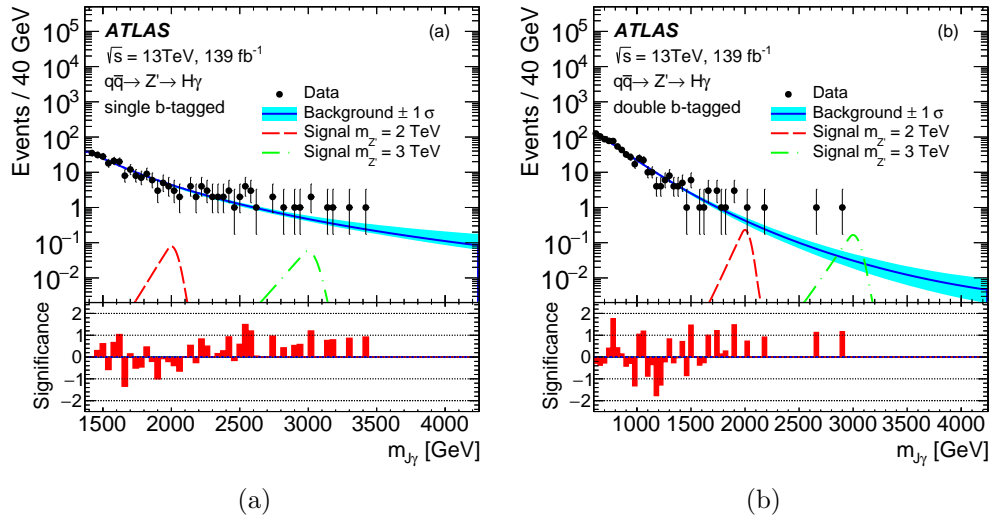


Figure 5.2: (a) and (b): Distribution of the reconstructed  $m_{J\gamma}$  in the single b-tagged and double b-tagged categories. Blue curves show the background only fitting result. Hypothetical signal distributions for  $m_{Z'} = 2\text{ TeV}$  and  $m_{Z'} = 3\text{ TeV}$  with arbitrary normalizations are plotted for illustration purposes. The bottom panel gives the significance (deviation / statistical uncertainty) for each bin. The impact on the background fit from the statistical uncertainties of background pdf parameters is shown as a light band around the solid line.

## 5.2 Likelihood and hypothesis testing

In general, the likelihood function is based on the model pdf,  $f(\theta, X)$ , where  $\theta$  represents the parameters and  $X$  is the measurement, and in this analysis  $X$  is the invariant mass  $m_{J\gamma}$  for each events. The likelihood function is defined as the product of the model pdf of each event:

$$\mathcal{L} = \prod_i f(\theta, X_i) \quad (5.1)$$

Here  $i$  represents the event order. The likelihood function can describe how well the pdf describes the observed data distribution. The larger likelihood value it is, the better agreement between the distribution and the model shape is observed. In this analysis, since both the signal and background model are analytical function, an unbinned likelihood is built based on the two models and the systematic uncertainties:

$$\begin{aligned} \mathcal{L}(\mu, \theta) = & \left( \prod_{j,l} \text{Pois} \left( n_j^{\text{obs}} \middle| n_j^{\text{sig}}(\mu, \theta_k) + n_j^{\text{SS}} \cdot \theta_j^{\text{SS}} + n_j^{\text{bkg}} \right) \times [f_s \cdot S_j(x_{l,j}; m_{J\gamma}, \theta_k) + f_b \cdot B_j(x_{l,j}; m_{J\gamma})] \right) \\ & \left( \prod_k p_k(\theta_k) \right) \left( \prod_j p_j(\theta_j^{\text{SS}}) \right) \end{aligned} \quad (5.2)$$

$J$  represents the signal region, which can be single  $b$ -tagged and double  $b$ -tagged signal region.  $l$  is the event order. “Pois” means Poisson function, which is used to determined the event yield in each signal region.  $n_j^{\text{obs}}$  is the total data events in  $j$  signal region.  $n_j^{\text{sig}}$  is the number of signal events in  $j$  signal region.  $\mu$  is the signal strength, which is the parameter of interest (POI). In this analysis, the POI is cross-section  $\times$  branch ratio, and the relationship between the POI and the  $n_j^{\text{sig}}$  is:  $n_j^{\text{sig}} = L \times \sigma \times \text{Br}(Z' \rightarrow H\gamma) \times \epsilon_j$ , here  $L$  is the luminosity,  $\sigma \times \text{Br}(Z' \rightarrow H\gamma)$  is the cross-section for the heavy resonance  $Z'$  times the decay branching fraction of  $Z'$  decaying into one Higgs boson plus one photon.  $\epsilon_j$  is the signal efficiency in signal region  $j$ . The nominal signal efficiency is derived from MC signal sample, in Section 4.4.  $\theta_k$  is the nuisance parameter for the systematic uncertainties except for spurious signal uncertainty. It describes the variation from the nominal value of the fitting result for the parameters in signal model. Detail about the implementation of the systematic uncertainties and the corresponding nuisance parameters will be introduced later.  $n_j^{\text{SS}}$  is the number of spurious signal in signal region  $j$ , and  $\theta_j^{\text{SS}}$  is the nuisance

parameter for the spurious signal.  $n_j^{bkg}$  is the number of background events in signal region  $j$ .  $S_j$  and  $B_j$  are the signal and background pdf in signal region  $j$ , which are the function of invariant mass  $m_{J\gamma}$ .  $f_s$  and  $f_b$  are the signal and background fraction.  $f_s + f_b = 1$ .  $x_{l,j}$  represents the  $l^{th}$  event in signal region  $j$ .  $p_k(\theta_k)$  and  $p_j(\theta_j^{SS})$  are the pdf constraining the nuisance parameters.

These constrain pdfs are chosen to be the Gaussian function:

$$p_k(\theta_k) = \frac{1}{\sqrt{2\pi}} e^{-\theta_k^2/2} \quad (5.3)$$

All the systematic uncertainties in Section 4.7, except for the spurious signal uncertainty, will cause variation for the signal efficiency, signal peak position and signal distribution resolution. A linear extrapolation method is applied for these systematic uncertainties. For example, for the large- $R$  jet mass resolution (JMR) systematic uncertainty, the final efficiency including the JMR systematic uncertainty impact is:

$$\epsilon = \epsilon_{Nominal} \times (1 + \theta_{JMR} \times \Delta_{JMR}) \quad (5.4)$$

Here  $\epsilon$  is the final signal efficiency function, which is a function of the nuisance parameter of JMR  $\theta_{JMR}$ . And  $\epsilon$  is the nominal signal efficiency, which is from the signal MC sample in Section 4.4.  $\Delta_{JMR}$  is the variation of the signal efficiency from the JMR systematic uncertainty. For example, for 2 TeV resonance mass, this variation is -30.2%, as shown in Table 4.5. It is the same for the signal peak position and the signal distribution resolution, a linear extrapolation is introduced for each systematic uncertainties, and multiply all the systematic uncertainties together, except for the spurious signal uncertainty. For the spurious signal uncertainty, mentioned in Section 4.7.3, the number of spurious signal events is from the signal+background fitting with data events in the control region. And the corresponding nuisance parameters are treated the same as other systematic uncertainties, which are constrained with the Gaussian function. Based on the likelihood function, the “one-side profiled likelihood ratio” [99] is defined as:

$$\tilde{\lambda}(\mu) = \begin{cases} \frac{L(\mu, \hat{\hat{\theta}}(\mu))}{L(\hat{\mu}, \hat{\hat{\theta}})}, & \hat{\mu} \geq 0 \\ \frac{L(\mu, \hat{\hat{\theta}}(\mu))}{L(0, \hat{\hat{\theta}}(0))}, & \hat{\mu} < 0 \end{cases} \quad (5.5)$$

$\mu$  is the POI, which is the cross-section  $\times$  branch ratio.  $\hat{\hat{\theta}}(\mu)$  represents the value of  $\theta$  which maximize the likelihood function for the specific  $\mu$  value. It is the conditional maximum-likelihood estimator of  $\theta$ .  $\hat{\mu}$  and  $\hat{\theta}$  are the values to maximize the likelihood based on the observed data distribution. The reason for choosing this one-side profile likelihood is that it is assumed that the new signal can only increase the mean number of events for the expected background. So if the POI value corresponding to the maximum-likelihood is negative, then from this assumption the best value can be used for POI is  $\mu = 0$ . The higher  $\tilde{\lambda}(\mu)$  means the better agreement between the data and the hypothesis at value of  $\mu$ . With the profile likelihood function, the statistic is defined as:

$$\tilde{t}_\mu = -2\ln\tilde{\lambda}(\mu) = \begin{cases} -2\ln\frac{L(\mu,\hat{\hat{\theta}}(\mu))}{L(\hat{\mu},\hat{\theta})}, & \hat{\mu} \geq 0 \\ -2\ln\frac{L(\mu,\hat{\hat{\theta}}(\mu))}{L(0,\hat{\hat{\theta}}(0))}, & \hat{\mu} < 0 \end{cases} \quad (5.6)$$

and as the basis of the statistical test. Opposite to the profile likelihood ratio, the higher statistic  $\tilde{t}_\mu$ , the larger incompatibility between data and the hypothesis  $\mu$ . To quantify the disagreement between the data and the hypothesis  $\mu$ , the p-value is defined as the integral from the observed statistic value to infinity to show the probability of the sum of incompatibility:

$$p_\mu = \int_{\tilde{t}_{\mu,\text{obs}}}^{\infty} f(\tilde{t}_\mu | \mu) d\tilde{t}_\mu \quad (5.7)$$

Here  $\tilde{t}_{\mu,\text{obs}}$  is the statistic  $\tilde{t}_\mu$  value observed from the actual data.  $f(\tilde{t}_\mu | \mu)$  is the pdf of the statistic  $t_\mu$  with the hypothesis signal strength  $\mu$ . This pdf is from either toy MC measurement or from asymptotic approximation. In this analysis, the sensitivity in Section 5.2.1 is calculated using asymptotic approximation[99], while for limit setting in Section 5.2.2, this pdf is from toy MC study. More detail about the toy MC study in ATLAS will be introduced in 5.2.2. Usually this p-value is converted to the significance, Z:

$$Z = \Phi^{-1}(1 - p) \quad (5.8)$$

Here  $\Phi$  is the cumulative distribution of the standard normal distribution:  $\varphi(x) = \frac{1}{\sqrt{2\pi}}e^{-\frac{1}{2}x^2}$ .

Figure 5.4 shows the p-value at 0.05 and the corresponding significance value Z.

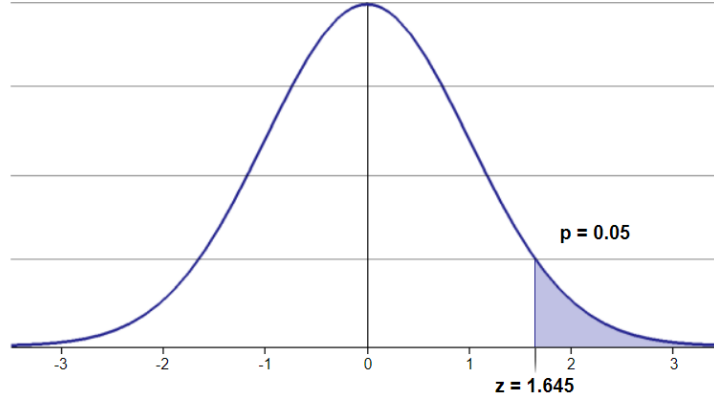


Figure 5.4: The standard normal distribution and the relationship between p-value at 0.05 and the significance.

### 5.2.1 Search for the signal

For searching for the signal, the null hypothesis is the background only model. To find out the new signal, it is equivalent to reject this background only model as  $H_0$ . For the background only model, the signal strength  $\mu = 0$ . The statistic, denoted with a special notation  $q_0 = \tilde{t}_0$ , is:

$$q_0 = \begin{cases} -2 \ln \frac{L(0, \hat{\theta}(0))}{L(\hat{\mu}, \hat{\theta})}, & \hat{\mu} \geq 0 \\ 0, & \hat{\mu} < 0 \end{cases} \quad (5.9)$$

To quantify whether the new phenomenon is observed or not, the p-value is defined as:

$$p_0 = \int_{q_{0,\text{obs}}}^{\infty} f(q_0 | 0) dq_0 \quad (5.10)$$

Here the distribution  $f(q_0 | 0)$  is from the asymptotic approximation[99]. The smaller p-value it is, the more inconsistency between data and the background only hypothesis. In high energy physics, to claim a discovery, just like the Higgs boson in 2012, usually it is required that  $Z > 5$ , corresponding to  $p = 2.87 \times 10^{-7}$ . Since  $\sigma = 1$ , this  $Z > 5$  requirement is usually quoted as  $5\sigma$ . And a strong “evidence” for the discovery requires  $3\sigma$ , corresponding to  $Z > 3$ .

Figure 5.6 shows the p-value scan result for different resonance mass  $m_{J\gamma}$  hypothesis with a step 25 GeV. No large significance is observed along the search region and the largest significance is below  $3\sigma$ . The largest significance is  $2.69\sigma$  at 775 GeV.

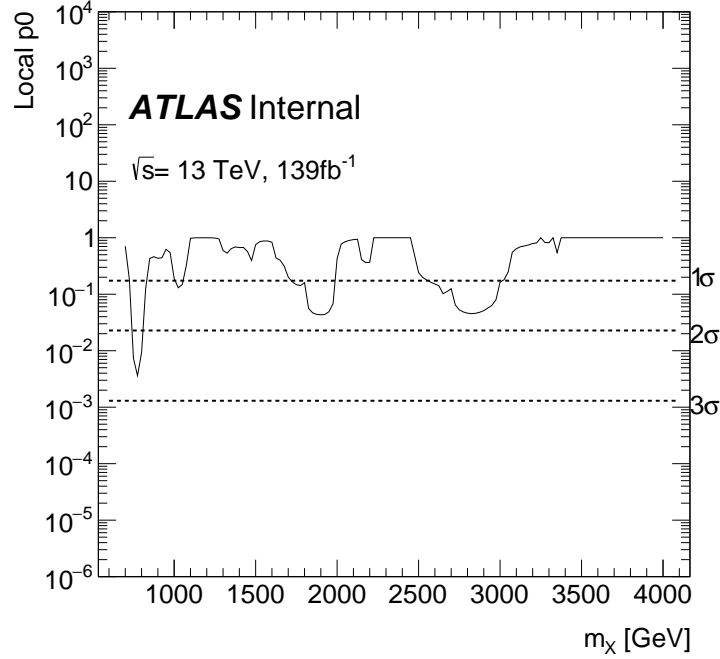


Figure 5.6: p-value scan for different resonance mass  $m_{J\gamma}$  hypothesis with a step 25 GeV. Left axis shows the p-value and the right axis shows the corresponding significance value. No large significance is observed along the search region and the largest significance is below  $3\sigma$ . The largest significance is  $2.69\sigma$  at 775 GeV.

### 5.2.2 Limit

Since there is no large deviation from the background only model, in Section 5.2.1, the [upper limit](#) is set along the search range. Different from discovering the signal, the null hypothesis for the limit setting is the signal+background model. So to set the limit is to find out the smallest signal strength which can be used to reject this signal+background model as  $H_0$ . On the other thing, in high energy physics, the  $CL_s$  method is usually used for the upper limit calculation [100].

The statistic for the signal strength  $\mu$  is denoted with a special notation  $q_\mu = \tilde{t}_\mu$ , is:

$$q_\mu = \begin{cases} -2\ln \frac{L(\mu, \hat{\theta}(\mu))}{L(0, \hat{\theta}(0))}, & \hat{\mu} < 0 \\ -2\ln \frac{L(\mu, \hat{\theta}(\mu))}{L(\hat{\mu}, \hat{\theta})}, & 0 \leq \hat{\mu} \leq \mu \\ 0, & \hat{\mu} > \mu \end{cases} \quad (5.11)$$

For the  $CL_s$  method, it defines two p-value  $p_\mu$  and  $p_b$  from the statistic  $q_\mu$ :

$$p_\mu = \int_{q_{\mu, \text{obs}}}^{\infty} f(q_\mu | \mu) dq_\mu \quad \text{and} \quad p_b = \int_{\infty}^{q_{\mu, \text{obs}}} f(q_\mu | 0) dq_\mu \quad (5.12)$$

The confidence level is defined as:

$$CL_s(\mu) = \frac{p_\mu}{1 - p_b} \quad (5.13)$$

For the upper limit of the signal strength  $\mu$ , usually it is chosen to be 95 % confidence level upper limit:  $CL_s = 0.05$ .

In this analysis the toy MC sample is generated to get the distribution used in Equation 5.12. There are two kinds of upper limit: observed upper limit and expected (median) upper limit. The observed upper limit shows the 95 % confidence level upper limit for the signal+background model using the observed data events, while the expected limit shows the upper limit for the signal+background model but using the events generated with background only model. Here is the summary about how to calculate both the observed limit and the expected limit using toy MC sample. For observed limit:

- 1: Calculate the observed test statistic value, Equation 5.11, using the data events with signal strength  $\mu$ , called  $q_{\mu, \text{obs}}$ ;
- 2: Generate two groups of toy MC experiments to construct the pdf of  $q_\mu$  for: 1:  $p_\mu$  using signal+background model whose parameters, including all the nuisance parameters for systematic uncertainties and all the parameters in background function, are from the signal+background fitting:  $\hat{\theta}(\mu)$ ; 2:  $p_b$  using the background only model. Each group has 5000 experiments.

- 3: Calculate the test statistic value  $q_\mu$  for each toy MC experiment for both of the two groups toy MC experiments, and form the distribution:  $f(q_\mu | \mu, \hat{\theta}(\mu))$  and  $f(q_\mu | 0, \hat{\theta}(0))$ ;
- 4: From the pdf,  $p_\mu$  and  $p_b$  can be calculated using Equation 5.12 and the corresponding  $CL_s$  value;
- 5: Repeat the above steps for different  $\mu$  value, to find the  $\mu_{up}$  which satisfies  $CL_s = 5\%$ , then this  $\mu_{up}$  is the observed upper limit for the signal strength  $\mu$ .

Instead of using the data events to calculate the observed test statistic, the expected upper limit uses the events generated from the background only model:

- 1: Generate many toy MC experiments(2500 in this analysis) using the background only model, whose parameters are from the background only fitting:  $\hat{\theta}(0)$ ;
- 2: For each background only toy MC experiment, repeat the calculation procedure for the observed limit mentioned above, replacing the real data with these background only toy MC experiments, to calculate the observed limit for each background only toy MC experiment;
- 3: Draw the distribution for these 2500 observed limits and the median of the distribution is the expected limit. It is called median limit;
- 4: The  $\pm 1$  and  $\pm 2\sigma$  bands are the corresponding 68 % and 95 % bands in the above distribution;

When calculating the combined limit, different invariant mass ranges are used for different categories, which are listed as follows:

- single b-tagged category: fit  $m_{J\gamma}$  range [1.4 TeV - 4.2 TeV], signal resonance mass range [1.5 TeV - 4 TeV]
- double b-tagged category: fit  $m_{J\gamma}$  range [0.6 TeV - 4.2 TeV], signal resonance mass range [0.7 TeV - 4 TeV]



For the combined limit, the searching range is the same as double b-tagged category. The fit range is chosen to be larger than the searching range to take the width of signal shape into account.

Figure 5.8 shows the observed and expected 95 % confidence-level limits on  $\sigma \times B$  for search range. No obvious deviation is observed.

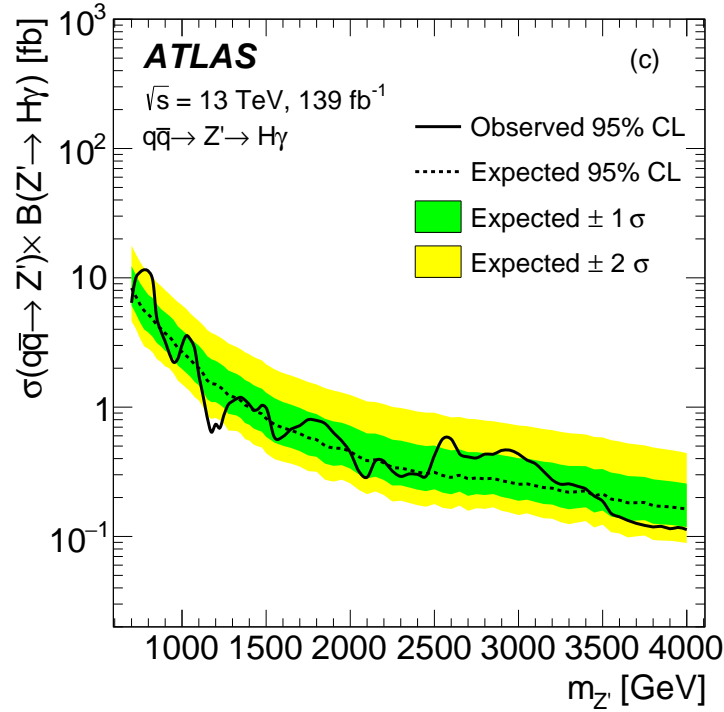


Figure 5.8: Observed and expected 95 % confidence-level limits on  $\sigma \times B$  for search range. No obvious deviation is observed.

Figure 5.10 shows the comparison for the expected upper limit between the result in this thesis, shown in Figure 5.8, and the previous CMS result[101]. For the previous CMS result, it used the data collected in 2015 and 2016 year by the CMS detector, corresponding to a total luminosity of  $36 \text{ fb}^{-1}$ . Higher luminosity means more number of events are collected, which can increase the search sensitivity. So even though the analysis doesn't change anything, with more luminosity, a better (smaller) upper limit is always expected. To separate the improvement due to

statistic gain and the improvement from the analysis strategy, which is the novel  $H \rightarrow b\bar{b}$  for ATLAS, the luminosity of CMS result should be scaled to the same luminosity of ATLAS result.

From the asymptotic approximation[99], the upper limit:

$$\mu_{\text{up}} = \hat{\mu} + \sigma \Phi^{-1}(1 - \alpha) \quad (5.14)$$

Here  $\mu_{\text{up}}$  is the upper limit for the signal strength.  $\hat{\mu}$  is the mean value for the signal strength, for the expected upper limit, the average value for the signal strength is zero.  $\sigma$  is the uncertainty of the signal strength.  $\Phi$  is the cumulative distribution of the standard Gaussian. For 95 % confidence level,  $\alpha$  is chosen to be 0.05. The number of events ( $N_{\text{event}}$ ) in a certain range follows the Poisson distribution, so the uncertainty for the number of events is  $\sqrt{N_{\text{event}}}$ . The signal strength in this analysis is the cross-section times the branching ratio, which is proportional to the number of events divide by the luminosity. So the upper limit and the uncertainty of the signal strength is proportional to the  $\sqrt{N_{\text{event}}}/\text{luminosity}$  (luminosity can be considered as a constant). In the end,  $N_{\text{event}}$  is proportional to the luminosity, the upper limit for the signal strength is proportional to the inverse of square root of luminosity:

$$\mu_{\text{up}} \propto \frac{1}{\sqrt{\text{Luminosity}}} \quad (5.15)$$

So if CMS has the same luminosity as ATLAS, the expected upper limit will be lower down by a factor of  $\sqrt{\frac{139}{36}} = 1.96$ . In Figure 5.10, the top plot shows the expected upper limit for both the ATLAS and CMS results. The bottom plot shows the CMS/ATLAS ratio for the expected upper limit, with a horizontal dashed line at 1.96, corresponding to the scale factor for the luminosity. The dashed line shows the improvement gain only from statistic, and if the ratio is above the dashed line, it means on top of statistic gain, the ATLAS result has better performance in the analysis strategy. From the blue ratio curve, in general the ratio is 30 % higher than the factor 1.96, which means the new ATLAS result in this analysis has 30 % better performance than the latest CMS result, and if CMS wants to achieve the same expected limit, 70 % more luminosity needs to be collected with the current analysis strategy. As for the high mass region, due to the

decreasing background, both the CMS and ATLAS results give reduced importance to the b-tagging, and therefore any benefits from the CoM algorithm will have less impact.

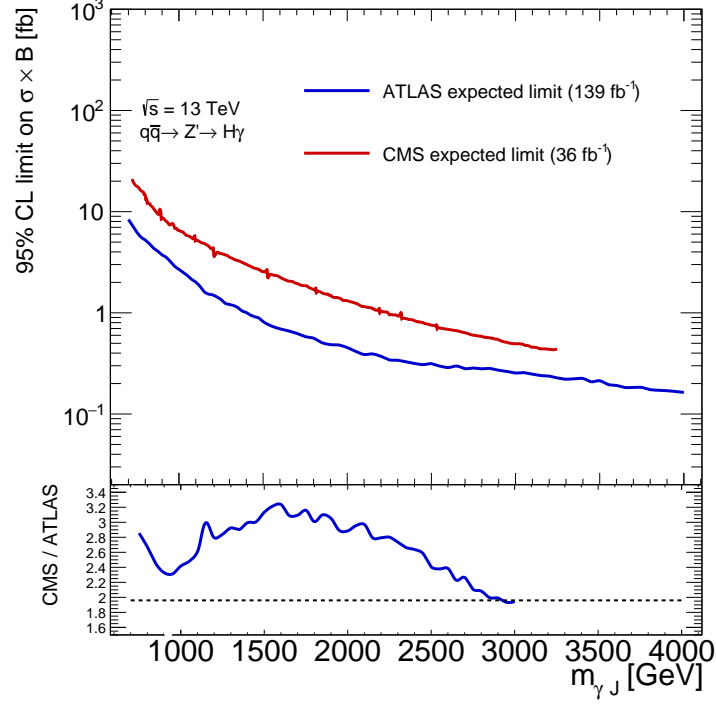


Figure 5.10: Comparison between the latest ATLAS result and the previous CMS result. On top of the statistic gain, the ATLAS upper limit is 30 % better than CMS result

## CHAPTER 6. CONCLUSION

### 6.1 SUMMARY

A search for heavy resonance decaying into a photon and a Higgs boson is performed, where the Higgs boson continually decaying into a pair of  $b$ -quarks, with the ATLAS detector at the LHC. Data was collected during the full Run 2 period in proton-proton collision of LHC at the center-of-mass(CoM) energy of  $\sqrt{s} = 13$  TeV with an integrated luminosity of  $139 \text{ fb}^{-1}$ . A novel boost  $H \rightarrow b\bar{b}$  tagger: CoM tagger, is applied to improve the search sensitivity. The final result is consistent with SM prediction.

#### 6.1.1 Future Work

ATLAS is going to restart in 2021 for run 3 data collection. More data can be studied to improve the search sensitivity. Besides more data, there are a few other possible studies which may increase the search sensitivity:

- Search for the heavy resonance in vector boson fusion (VBF) topology. In the analysis presented in this thesis, there is no associated object with the heavy resonance, the pure final decay product, one Higgs and one photon are required. However, the new particle can be produced with different topology, for example, in the VBF process, as shown in Figure 6.2. In the VBF, besides the high  $p_T$  Higgs boson and photon, there are two high  $p_T$  jet;
- There are many different developing algorithms in ATLAS from which this analysis can be benefited. For example, currently the large-R jet is using the default ATLAS jet reconstruction algorithm. In these two years a few different jet algorithms are proposed, for example, the unified flow object (UFO) jet[102]. This new jet algorithm combines

calorimeter and inner-detector-based signals in order to achieve optimal performance across a wide kinematic range, which can significantly improve the identification of large-R jet;

- Another possible improvement is from the new  $H \rightarrow b\bar{b}$  tagger. In this analysis, the CoM tagger is applying the MV2c10 algorithm for the b-tagging. In ATLAS flavor tagging group, people build a different algorithm based on the deep learning[103, 104].

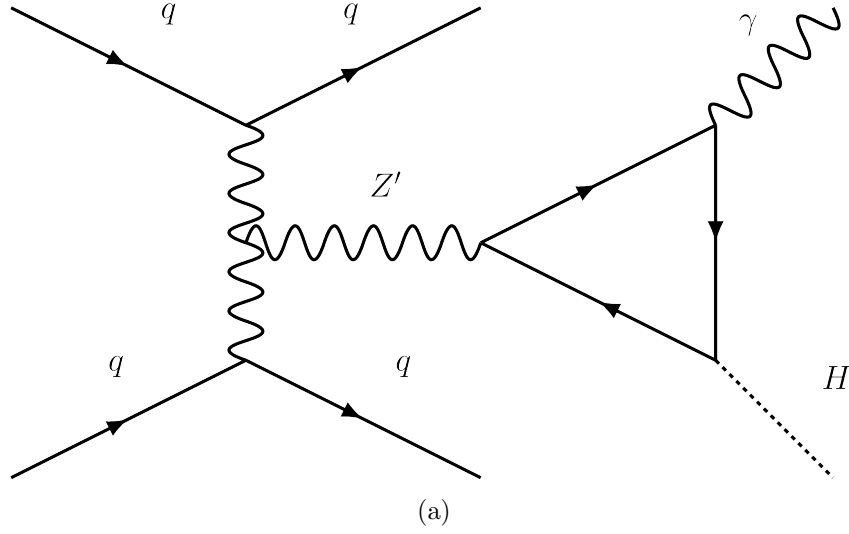


Figure 6.2: VBF topology for  $H\gamma$  resonance.

## Bibliography

- [1] B. Pullman and A.R. Reisinger. *The Atom in the History of Human Thought*. Oxford University Press, 2001.
- [2] A. Kenny. *Ancient Philosophy: A New History of Western Philosophy, Volume 1*. New History of Western Philosophy. OUP Oxford, 2006.
- [3] P.H.A. Grafton, A. Grafton, G.W. Most, S. Settis, and D.G.R.I.H.A.H.P.C.A.A.S. Settis. *The Classical Tradition*. Harvard University Press reference library. Harvard University Press, 2010.
- [4] H. Cohen and C. Lefebvre. *Handbook of Categorization in Cognitive Science*. Elsevier Science, 2017.
- [5] J. Dalton. "Essay IV. On the expansion of elastic fluids by heat". Number vol. 5, pt. 2, pages 595–602. Memoirs of the Literary and Philosophical Society of Manchester. The Society, 1802.
- [6] Rayleigh. Joseph john thomson. 1856-1940. *Obituary Notices of Fellows of the Royal Society*, 3(10):587–609, 1941.
- [7] Joseph John Thomson. Xxiv. on the structure of the atom: an investigation of the stability and periods of oscillation of a number of corpuscles arranged at equal intervals around the circumference of a circle; with application of the results to the theory of atomic structure. *The London, Edinburgh, and Dublin Philosophical Magazine and Journal of Science*, 7(39):237–265, 1904.
- [8] Ernest Rutherford. Lxxix. the scattering of  $\alpha$  and  $\beta$  particles by matter and the structure of the atom. *The London, Edinburgh, and Dublin Philosophical Magazine and Journal of Science*, 21(125):669–688, 1911.
- [9] Niels Bohr. I. on the constitution of atoms and molecules. *The London, Edinburgh, and Dublin Philosophical Magazine and Journal of Science*, 26(151):1–25, 1913.
- [10] Niels Bohr. Lxxiii. on the constitution of atoms and molecules. *The London, Edinburgh, and Dublin Philosophical Magazine and Journal of Science*, 26(155):857–875, 1913.
- [11] Niels Bohr. Xxxvii. on the constitution of atoms and molecules. *The London, Edinburgh, and Dublin Philosophical Magazine and Journal of Science*, 26(153):476–502, 1913.

- [12] E Rutherford. Collision of  $\alpha$  particles with light atoms. iv. an anomalous effect in nitrogen. *Philosophical Magazine*, 90(S1):31–37, 2010.
- [13] James Chadwick. Possible existence of a neutron. *Nature*, 129(3252):312–312, 1932.
- [14] Paul Adrien Maurice Dirac. The quantum theory of the electron. *Proceedings of the Royal Society of London. Series A, Containing Papers of a Mathematical and Physical Character*, 117(778):610–624, 1928.
- [15] Carl D Anderson. The apparent existence of easily deflectable positives. *Science*, 76(1967):238–239, 1932.
- [16] Seth H Neddermeyer and Carl D Anderson. Note on the nature of cosmic-ray particles. *Physical Review*, 51(10):884, 1937.
- [17] Murray Gell-Mann. A schematic model of baryons and mesons. *Physics Letters*, 8(3):214–215, 1964.
- [18] George Zweig. An  $su_3$  model for strong interaction symmetry and its breaking. Technical report, CM-P00042884, 1964.
- [19] J. E. Augustin, A. M. Boyarski, M. Breidenbach, F. Bulos, J. T. Dakin, G. J. Feldman, G. E. Fischer, D. Fryberger, G. Hanson, B. Jean-Marie, R. R. Larsen, V. Lüth, H. L. Lynch, D. Lyon, C. C. Morehouse, J. M. Paterson, M. L. Perl, B. Richter, P. Rapidis, R. F. Schwitters, W. M. Tanenbaum, F. Vannucci, G. S. Abrams, D. Briggs, W. Chinowsky, C. E. Friedberg, G. Goldhaber, R. J. Hollebeek, J. A. Kadyk, B. Lulu, F. Pierre, G. H. Trilling, J. S. Whitaker, J. Wiss, and J. E. Zipse. Discovery of a narrow resonance in  $e^+e^-$  annihilation. *Phys. Rev. Lett.*, 33:1406–1408, Dec 1974.
- [20] J. J. Aubert, U. Becker, P. J. Biggs, J. Burger, M. Chen, G. Everhart, P. Goldhagen, J. Leong, T. McCorriston, T. G. Rhoades, M. Rohde, Samuel C. C. Ting, Sau Lan Wu, and Y. Y. Lee. Experimental observation of a heavy particle  $j$ . *Phys. Rev. Lett.*, 33:1404–1406, Dec 1974.
- [21] SW Herb, DC Hom, LM Lederman, JC Sens, HD Snyder, JK Yoh, JA Appel, BC Brown, CN Brown, WR Innes, et al. Observation of a dimuon resonance at 9.5 gev in 400-gev proton-nucleus collisions. *Physical Review Letters*, 39(5):252, 1977.
- [22] Martin L Perl, GS Abrams, AM Boyarski, Martin Breidenbach, DD Briggs, F Bulos, William Chinowsky, JT Dakin, GJ Feldman, CE Friedberg, et al. Evidence for anomalous lepton production in  $e^+e^-$  annihilation. *Physical Review Letters*, 35(22):1489, 1975.
- [23] Frederick Reines and Clyde L Cowan. The neutrino. *Nature*, 178(4531):446–449, 1956.

- [24] G. Danby, J-M. Gaillard, K. Goulianos, L. M. Lederman, N. Mistry, M. Schwartz, and J. Steinberger. Observation of high-energy neutrino reactions and the existence of two kinds of neutrinos. *Phys. Rev. Lett.*, 9:36–44, Jul 1962.
- [25] K Kodama, N Ushida, C Andreopoulos, N Saoulidou, G Tzanakos, P Yager, B Baller, D Boehnlein, Walter Freeman, B Lundberg, et al. Observation of tau neutrino interactions. *Physics Letters B*, 504(3):218–224, 2001.
- [26] DP Barber, U Becker, H Benda, A Boehm, JG Branson, J Bron, D Buikman, J Burger, CC Chang, HS Chen, et al. Discovery of three-jet events and a test of quantum chromodynamics at petra. *Physical Review Letters*, 43(12):830, 1979.
- [27] G Arnison, A Astbury, B Aubert, C Bacci, G Bauer, A Bezaguët, R Böck, TJV Bowcock, M Calvetti, P Catz, et al. Experimental observation of lepton pairs of invariant mass around 95 gev/c<sup>2</sup> at the cern sps collider. *Physics Letters B*, 126(5):398–410, 1983.
- [28] G Arnison, A Astbury, B Aubert, C Bacci, G Bauer, A Bezaguët, R Böck, TJV Bowcock, M Calvetti, T Carroll, et al. Experimental observation of isolated large transverse energy electrons with associated missing energy at s= 540 gev. *Physics letters B*, 122(1):103–116, 1983.
- [29] M Banner, B Madsen, JC Chollet, JL Siegrist, H Hänni, L Di Lella, HM Steiner, V Vercesi, Pierre Darriulat, B Hahn, et al. Observation of single isolated electrons of high transverse momentum in events with missing transverse energy at the cern pp collider. *Phys. Lett. B*, 122(CERN-EP-83-25):476–485, 1983.
- [30] Georges Aad, Tatevik Abajyan, B Abbott, J Abdallah, S Abdel Khalek, Ahmed Ali Abdelalim, R Aben, B Abi, M Abolins, OS AbouZeid, et al. Observation of a new particle in the search for the standard model higgs boson with the atlas detector at the lhc. *Physics Letters B*, 716(1):1–29, 2012.
- [31] Serguei Chatrchyan, Vardan Khachatryan, Albert M Sirunyan, Armen Tumasyan, Wolfgang Adam, Ernest Aguilo, Thomas Bergauer, M Dragicevic, J Erö, C Fabjan, et al. Observation of a new boson at a mass of 125 gev with the cms experiment at the lhc. *Physics Letters B*, 716(1):30–61, 2012.
- [32] Yoshiyuki Fukuda, T Hayakawa, E Ichihara, K Inoue, K Ishihara, Hirokazu Ishino, Y Itow, T Kajita, J Kameda, S Kasuga, et al. Evidence for oscillation of atmospheric neutrinos. *Physical Review Letters*, 81(8):1562, 1998.
- [33] SNO collaboration et al. Measurement of the rate of  $\nu_e + d \rightarrow p + p + e^-$ -interactions produced by 8b solar neutrinos at the sudbury neutrino observatory. *arXiv preprint nucl-ex/0106015*, 2001.



- [34] Rabindra N. Mohapatra and Goran Senjanović. Neutrino mass and spontaneous parity nonconservation. *Phys. Rev. Lett.*, 44:912–915, Apr 1980.
- [35] Virginia Trimble. Existence and nature of dark matter in the universe. *Annual review of astronomy and astrophysics*, 25(1):425–472, 1987.
- [36] E. Corbelli and P. Salucci. The extended rotation curve and the dark matter halo of m33. *Monthly Notices of the Royal Astronomical Society*, 311(2):441–447, Jan 2000.
- [37] Gianfranco Bertone. *Particle dark matter: observations, models and searches*. Cambridge University Press, 2010.
- [38] P James E Peebles and Bharat Ratra. The cosmological constant and dark energy. *Reviews of modern physics*, 75(2):559, 2003.
- [39] Philippe Mouche. Overall view of the LHC. Vue d’ensemble du LHC. Jun 2014. General Photo.
- [40] Georges Aad, JM Butterworth, J Thion, U Bratzler, PN Ratoff, RB Nickerson, JM Seixas, I Grabowska-Bold, F Meisel, S Lokwitz, et al. The atlas experiment at the cern large hadron collider. *Jinst*, 3:S08003, 2008.
- [41] Brad Abbott, Justin Albert, Fabrizio Alberti, Markus Alex, Gianluca Alimonti, Steven Alkire, P Allport, Silke Altenheiner, Lucian Stefan Ancu, E Anderssen, et al. Production and integration of the atlas insertable b-layer. *Journal of instrumentation*, 13(05):T05008, 2018.
- [42] Joao Pequeno. Computer generated image of the whole ATLAS detector. Mar 2008.
- [43] Matthias Schott and Monica Dunford. Review of single vector boson production in pp collisions at  $\sqrt{s} = 7$  TeV. Review of single vector boson production in pp collisions at  $\sqrt{s} = 7$  TeV. *Eur. Phys. J. C*, 74(arXiv:1405.1160):60 p, May 2014. Comments: 60 pages, 64 figures, For Eur. Phys. J. C.
- [44] Joao Pequeno. Computer generated image of the ATLAS inner detector. Mar 2008.
- [45] Joao Pequeno. Computer Generated image of the ATLAS calorimeter. Mar 2008.
- [46] Aranzazu Ruiz-Martinez et al. The run-2 atlas trigger system. In *J. Phys.: Conf. Ser.*, volume 762, page 012003. ATL-COM-DAQ-2016-009, 2016.
- [47] Gergely Gábor Barnaföldi, András G. Agócs, and Péter Lévai. Underlying event studies for lh energy. 2011.

- [48] M. Aaboud, G. Aad, B. Abbott, J. Abdallah, O. Abdinov, B. Abeloos, S. H. Abidi, O. S. AbouZeid, N. L. Abraham, and et al. Performance of the atlas track reconstruction algorithms in dense environments in lhc run 2. *The European Physical Journal C*, 77(10), Oct 2017.
- [49] G. Aad, B. Abbott, D.C. Abbott, A. Abed Abud, K. Abeling, D.K. Abhayasinghe, S.H. Abidi, O.S. AbouZeid, N.L. Abraham, H. Abramowicz, and et al. Electron and photon performance measurements with the atlas detector using the 2015–2017 lhc proton-proton collision data. *Journal of Instrumentation*, 14(12):P12006–P12006, Dec 2019.
- [50] G. Aad, B. Abbott, J. Abdallah, O. Abdinov, B. Abeloos, R. Aben, M. Abolins, O. S. AbouZeid, N. L. Abraham, and et al. Muon reconstruction performance of the atlas detector in proton–proton collision data at  $\sqrt{s}=13$  tev. *The European Physical Journal C*, 76(5), May 2016.
- [51] Steven Schramm. Atlas jet reconstruction, calibration, and tagging of lorentzboosted objects. In *EPJ Web of Conferences*, volume 182, page 02113. EDP Sciences, 2018.
- [52] Peter Berta et al. Atlas jet and missing-et reconstruction, calibration, and performance. *Nuclear and particle physics proceedings*, 273:1121–1126, 2016.
- [53] Estia Eichten and Kenneth Lane. Low-scale technicolor at the tevatron and lhc. *Physics Letters B*, 669(3):235 – 238, 2008.
- [54] Nima Arkani-Hamed, Andrew G. Cohen, and Howard Georgi. Electroweak symmetry breaking from dimensional deconstruction. *Physics Letters B*, 513(1):232 – 240, 2001.
- [55] Ian Low, Joseph Lykken, and Gabe Shaughnessy. Singlet scalars as higgs boson imposters at the large hadron collider. *Phys. Rev. D*, 84:035027, Aug 2011.
- [56] Bogdan A Dobrescu, Patrick J Fox, and John Kearney. Higgs–photon resonances. *The European Physical Journal C*, 77(10):704, 2017.
- [57] Daniel de Florian, Christophe Grojean, F Maltoni, C Mariotti, A Nikitenko, M Pieri, P Savard, M Schumacher, R Tanaka, R Aggleton, et al. Handbook of lhc higgs cross sections: 4. deciphering the nature of the higgs sector. *arXiv. org*, 2016.
- [58] Georges Aad, Tatevik Abajyan, Brad Abbott, Jalal Abdallah, S Abdel Khalek, AA Abdelalim, R Aben, B Abi, M Abolins, OS AbouZeid, et al. Measurement of the flavour composition of dijet events in pp collisions at  $\sqrt{s}=7$ TeV with the atlas detector. *The European Physical Journal C*, 73(2):2301, 2013.
- [59] Enrico Bothmann et al. Event generation with Sherpa 2.2. *SciPost Phys.*, 7(3):034, 2019.

- [60] Tanju Gleisberg and Stefan Höche. Comix, a new matrix element generator. *JHEP*, 12:039, 2008.
- [61] Fabio Cascioli, Philipp Maierhöfer, and Stefano Pozzorini. Scattering Amplitudes with Open Loops. *Phys. Rev. Lett.*, 108:111601, 2012.
- [62] Steffen Schumann and Frank Krauss. A parton shower algorithm based on Catani–Seymour dipole factorisation. *JHEP*, 03:038, 2008.
- [63] Stefan Höche, Frank Krauss, Steffen Schumann, and Frank Siegert. QCD matrix elements and truncated showers. *JHEP*, 05:053, 2009.
- [64] Richard D. Ball et al. Parton distributions for the LHC run II. *JHEP*, 04:040, 2015.
- [65] H.-L. Lai et al. New parton distributions for collider physics. *Phys. Rev. D*, 82:074024, 2010.
- [66] J. Pumplin et al. New Generation of Parton Distributions with Uncertainties from Global QCD Analysis. *JHEP*, 07:012, 2002.
- [67] J. Alwall, R. Frederix, S. Frixione, V. Hirschi, F. Maltoni, O. Mattelaer, H. S. Shao, T. Stelzer, P. Torrielli, and M. Zaro. The automated computation of tree-level and next-to-leading order differential cross sections, and their matching to parton shower simulations. *JHEP*, 07:079, 2014.
- [68] T. Sjöstrand, S. Mrenna, and P. Skands. A brief introduction to PYTHIA 8.1. *Comput. Phys. Commun.*, 178:852–867, 2008.
- [69] Richard D. Ball et al. Parton distributions with LHC data. *Nucl. Phys. B*, 867:244, 2013.
- [70] ATLAS Collaboration. ATLAS Pythia 8 tunes to 7 TeV data. ATL-PHYS-PUB-2014-021, 2014.
- [71] D. J. Lange. The EvtGen particle decay simulation package. *Nucl. Instrum. Meth. A*, 462:152, 2001.
- [72] S. Agostinelli et al. GEANT4 - a simulation toolkit. *Nucl. Instrum. Meth. A*, 506:250–303, 2003.
- [73] ATLAS Collaboration. The ATLAS Simulation Infrastructure. *Eur. Phys. J. C*, 70:823, 2010.
- [74] ATLAS Collaboration. Performance of electron and photon triggers in ATLAS during LHC Run 2. *Eur. Phys. J. C*, 80:47, 2020.

- [75] ATLAS Collaboration. Measurement of the photon identification efficiencies with the ATLAS detector using LHC Run 2 data collected in 2015 and 2016. *Eur. Phys. J.*, 2018.
- [76] ATLAS Collaboration. Performance of top-quark and  $W$ -boson tagging with ATLAS in Run 2 of the LHC. 2018.
- [77] Wikimedia Commons. File:b-tagging diagram.png — wikimedia commons, the free media repository, 2020. [Online; accessed 26-October-2020].
- [78] Georges Aad, Tatevik Abajyan, Brad Abbott, Jalal Abdallah, S Abdel Khalek, Ahmed Ali Abdelalim, R Aben, B Abi, M Abolins, OS AbouZeid, et al. Performance of jet substructure techniques for large- $r$  jets in proton-proton collisions at  $\sqrt{s} = 7$  tev using the atlas detector. *Journal of High Energy Physics*, 2013(9):76, 2013.
- [79] Matteo Cacciari, Gavin P Salam, and Gregory Soyez. The catchment area of jets. *Journal of High Energy Physics*, 2008(04):005, 2008.
- [80] Matteo Cacciari and Gavin P Salam. Pileup subtraction using jet areas. *Physics Letters B*, 659(1-2):119–126, 2008.
- [81] Expected performance of the ATLAS  $b$ -tagging algorithms in Run-2. Technical Report ATL-PHYS-PUB-2015-022, CERN, Geneva, Jul 2015.
- [82] Alessandro Calandri. Flavour tagging algorithms and performance at the ATLAS experiment. Technical Report ATL-PHYS-PROC-2016-105, CERN, Geneva, Aug 2016.
- [83] Chunhui Chen. Identification of a bottom quark-antiquark pair in a single jet with high transverse momentum and its application. *Phys. Rev. D*, 92:093010, Nov 2015.
- [84] Chunhui Chen. New approach to identifying boosted hadronically decaying particles using jet substructure in its center-of-mass frame. *Phys. Rev. D*, 85:034007, Feb 2012.
- [85] David Krohn, Jesse Thaler, and Lian-Tao Wang. Jet trimming. *Journal of High Energy Physics*, 2010(2), Feb 2010.
- [86] Matteo Cacciari, Gavin P. Salam, and Gregory Soyez. Fastjet user manual. *The European Physical Journal C*, 72(3), Mar 2012.
- [87] S. Catani, Yu.L. Dokshitzer, M. Olsson, G. Turnock, and B.R. Webber. New clustering algorithm for multijet cross sections in  $e^+e^-$  annihilation. *Physics Letters B*, 269(3):432 – 438, 1991.
- [88] Variable Radius, Exclusive- $k_T$ , and Center-of-Mass Subjet Reconstruction for Higgs( $\rightarrow b\bar{b}$ ) Tagging in ATLAS. Technical Report ATL-PHYS-PUB-2017-010, CERN, Geneva, Jun 2017.

- [89] MJ Oreglia, ED Bloom, F Bulos, R Chestnut, J Gaiser, G Godfrey, C Kiesling, William S Lockman, DL Scharre, R Partridge, et al. A study of the reactions  $\psi$  prime to gamma gamma  $\psi$ . *Physical Review D*, 25:2259, 1980.
- [90] Robert M Harris and Konstantinos Kousouris. Searches for dijet resonances at hadron colliders. *International Journal of Modern Physics A*, 26(30n31):5005–5055, 2011.
- [91] R.G. Lomax. *Statistical Concepts: A Second Course*. Lawrence Erlbaum Associates, 2007.
- [92] Electron and photon energy calibration with the ATLAS detector using data collected in 2015 at  $\sqrt{s} = 13$  TeV. Technical Report ATL-PHYS-PUB-2016-015, CERN, Geneva, Aug 2016.
- [93] Morad Aaboud, G Aad, B Abbott, J Abdallah, B Abeloos, R Aben, OS AbouZeid, NL Abraham, H Abramowicz, H Abreu, et al. Measurement of the photon identification efficiencies with the atlas detector using lhcb run-1 data. *The European Physical Journal C*, 76(12):1–42, 2016.
- [94] In-situ measurements of the ATLAS large-radius jet response in 13 TeV pp collisions. Technical Report ATLAS-CONF-2017-063, CERN, Geneva, Jul 2017.
- [95] Luminosity determination in  $pp$  collisions at  $\sqrt{s} = 13$  TeV using the ATLAS detector at the LHC. Technical Report ATLAS-CONF-2019-021, CERN, Geneva, Jun 2019.
- [96] William Buttinger. Using Event Weights to account for differences in Instantaneous Luminosity and Trigger Prescale in Monte Carlo and Data. Technical Report ATL-COM-SOFT-2015-119, CERN, Geneva, May 2015.
- [97] J. Alwall, R. Frederix, S. Frixione, V. Hirschi, F. Maltoni, O. Mattelaer, H.-S. Shao, T. Stelzer, P. Torrielli, and M. Zaro. The automated computation of tree-level and next-to-leading order differential cross sections, and their matching to parton shower simulations. *Journal of High Energy Physics*, 2014(7), Jul 2014.
- [98] Andy Buckley, James Ferrando, Stephen Lloyd, Karl Nordström, Ben Page, Martin Rüfenacht, Marek Schönherr, and Graeme Watt. Lhapdf6: parton density access in the lhcb precision era. *The European Physical Journal C*, 75(3):1–20, 2015.
- [99] Glen Cowan, Kyle Cranmer, Eilam Gross, and Ofer Vitells. Asymptotic formulae for likelihood-based tests of new physics. *The European Physical Journal C*, 71(2):1–19, 2011.
- [100] A L Read. Presentation of search results: theCLstechnique. *Journal of Physics G: Nuclear and Particle Physics*, 28(10):2693–2704, sep 2002.
- [101] CMS Collaboration. Search for narrow  $h\gamma$  resonances in proton–proton collisions at  $\sqrt{s} = 13$  tev. *Phys. Rev. Lett.*, 122:081804, 2019.

- [102] ATLAS Collaboration. Optimisation of large-radius jet reconstruction for the atlas detector in 13 tev proton–proton collisions, 2020.
- [103] Georges Aad et al. ATLAS b-jet identification performance and efficiency measurement with  $t\bar{t}$  events in pp collisions at  $\sqrt{s} = 13$  TeV. *Eur. Phys. J. C*, 79(11):970, 2019.
- [104] Michela Paganini et al. Machine learning algorithms for b-jet tagging at the atlas experiment. In *Journal of Physics: Conference Series*, volume 1085, page 042031. IOP Publishing, 2018.

## APPENDIX. ADDITIONAL MATERIAL

### .1 Signal systematic uncertainties

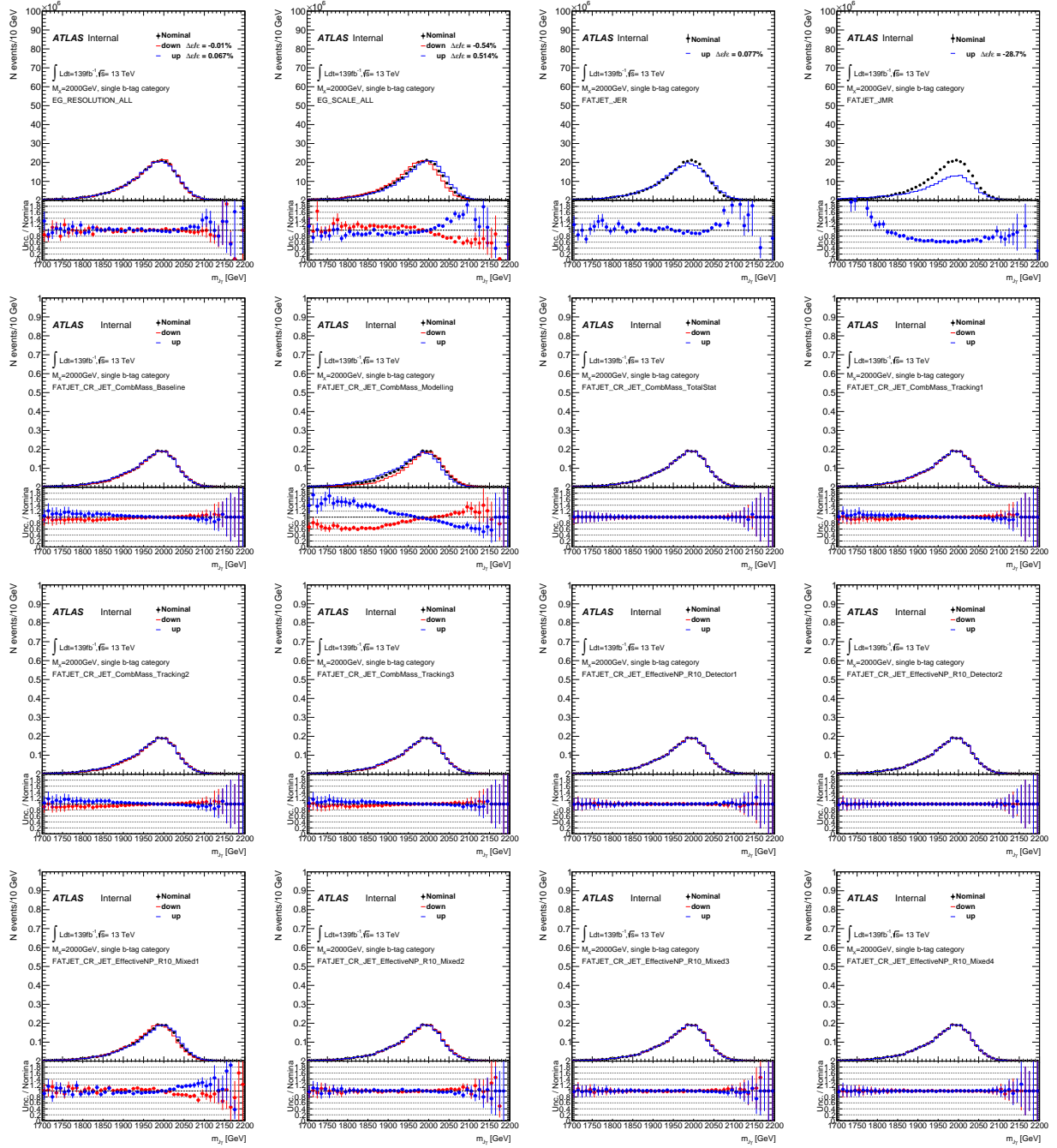


Figure .2: Signal resonance mass at 2000 GeV, in single  $b$ -tagged SR. Comparison of  $H\gamma$  mass spectrum between nominal signal MC sample and all the systematic variations.



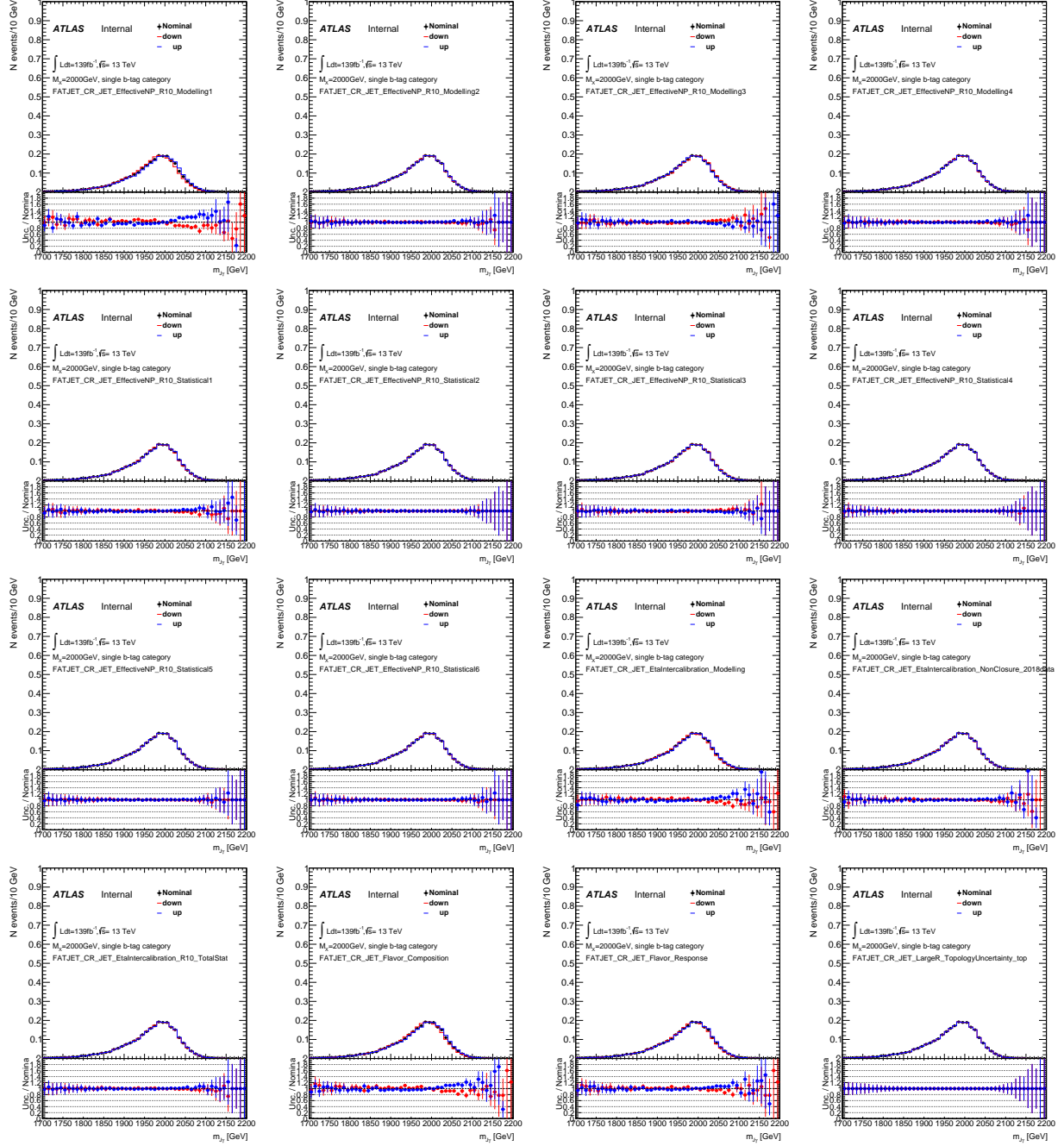


Figure .4: Signal resonance mass at 2000 GeV, in single  $b$ -tagged SR. Comparison of  $H\gamma$  mass spectrum between nominal signal MC sample and all the systematic variations.

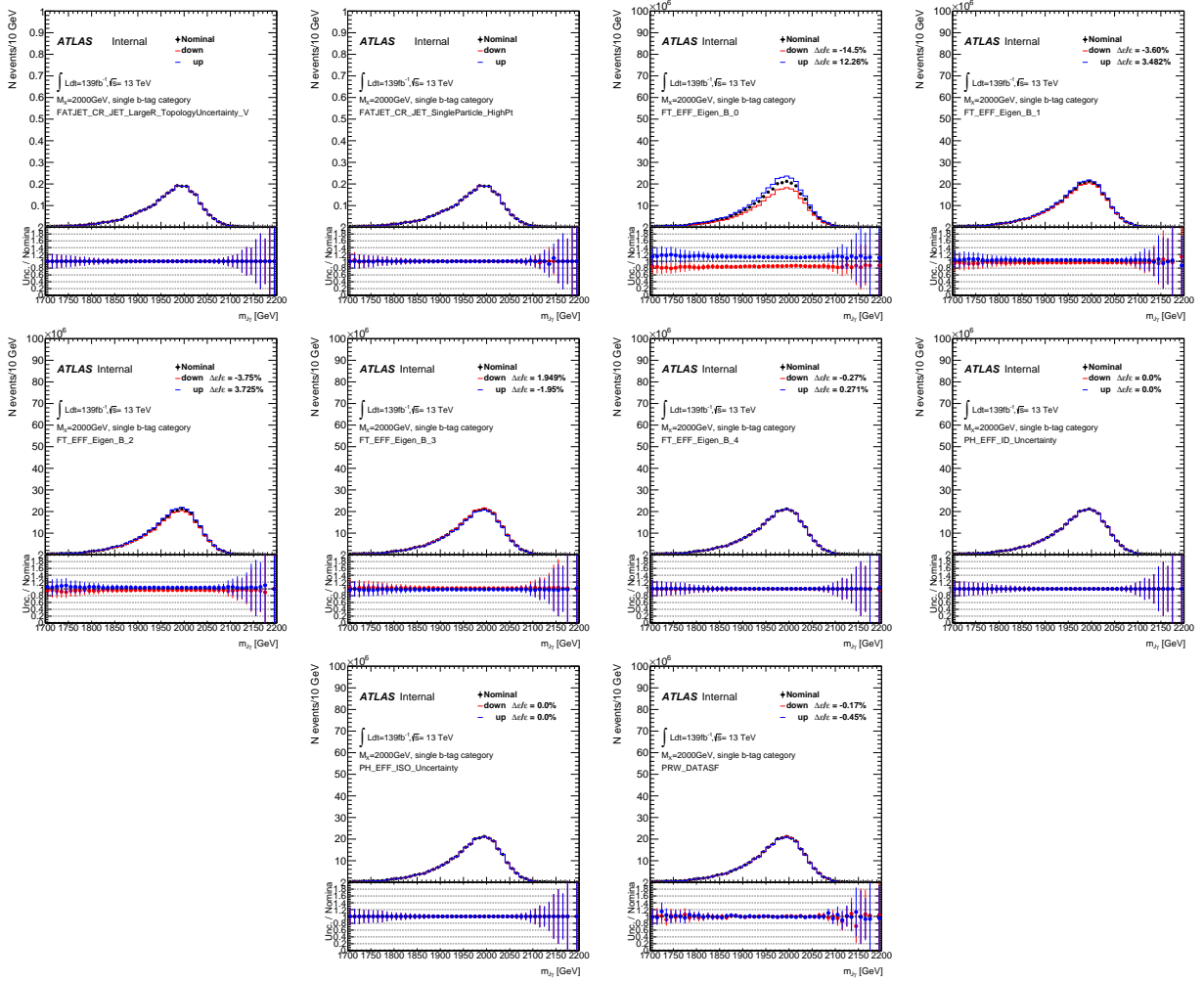


Figure .6: Signal resonance mass at 2000 GeV, in single  $b$ -tagged SR. Comparison of  $H\gamma$  mass spectrum between nominal signal MC sample and all the systematic variations.

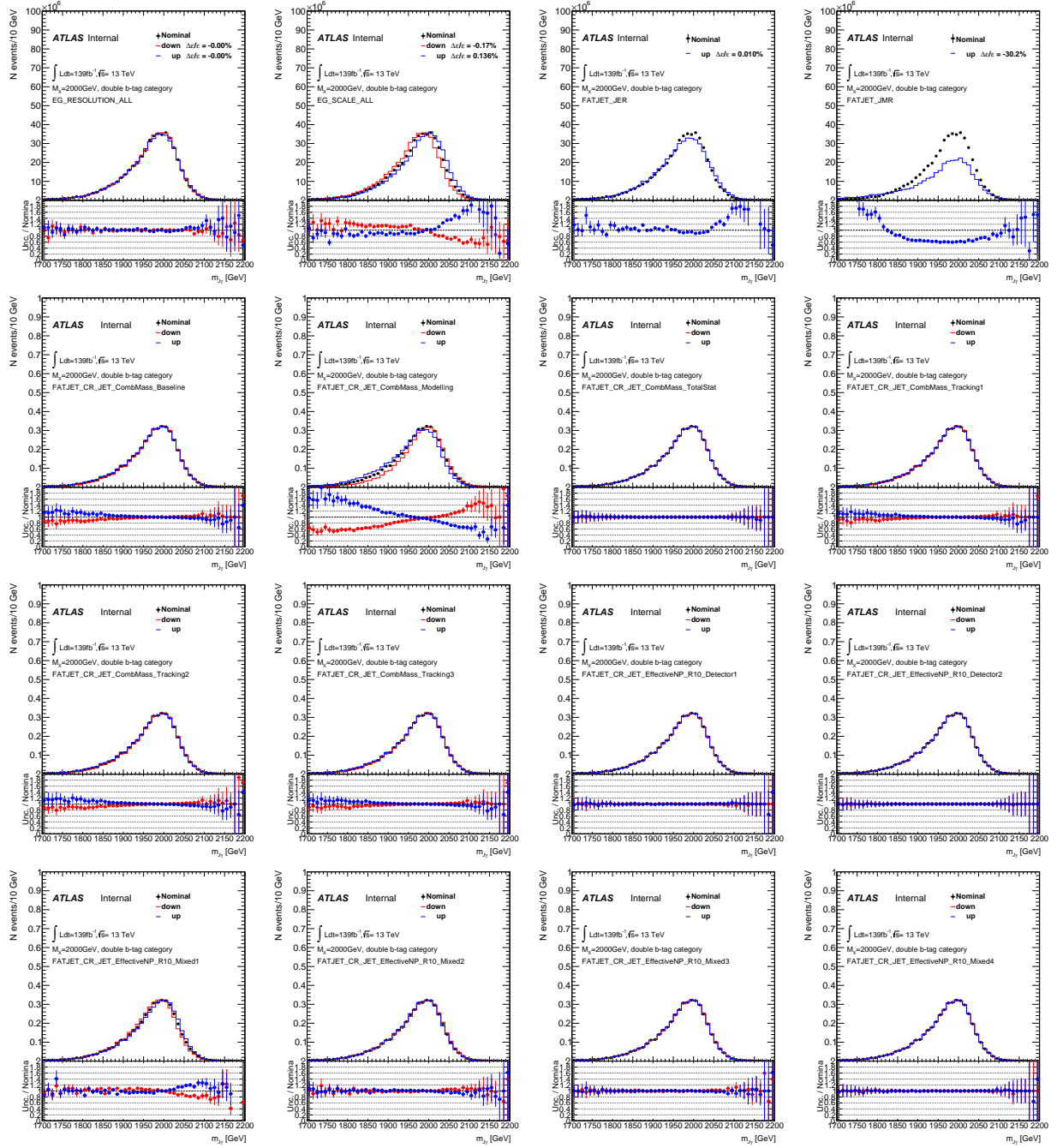


Figure .8: Signal resonance mass at 2000 GeV, in double  $b$ -tagged SR. Comparison of  $H\gamma$  mass spectrum between nominal signal MC sample and all the systematic variations.

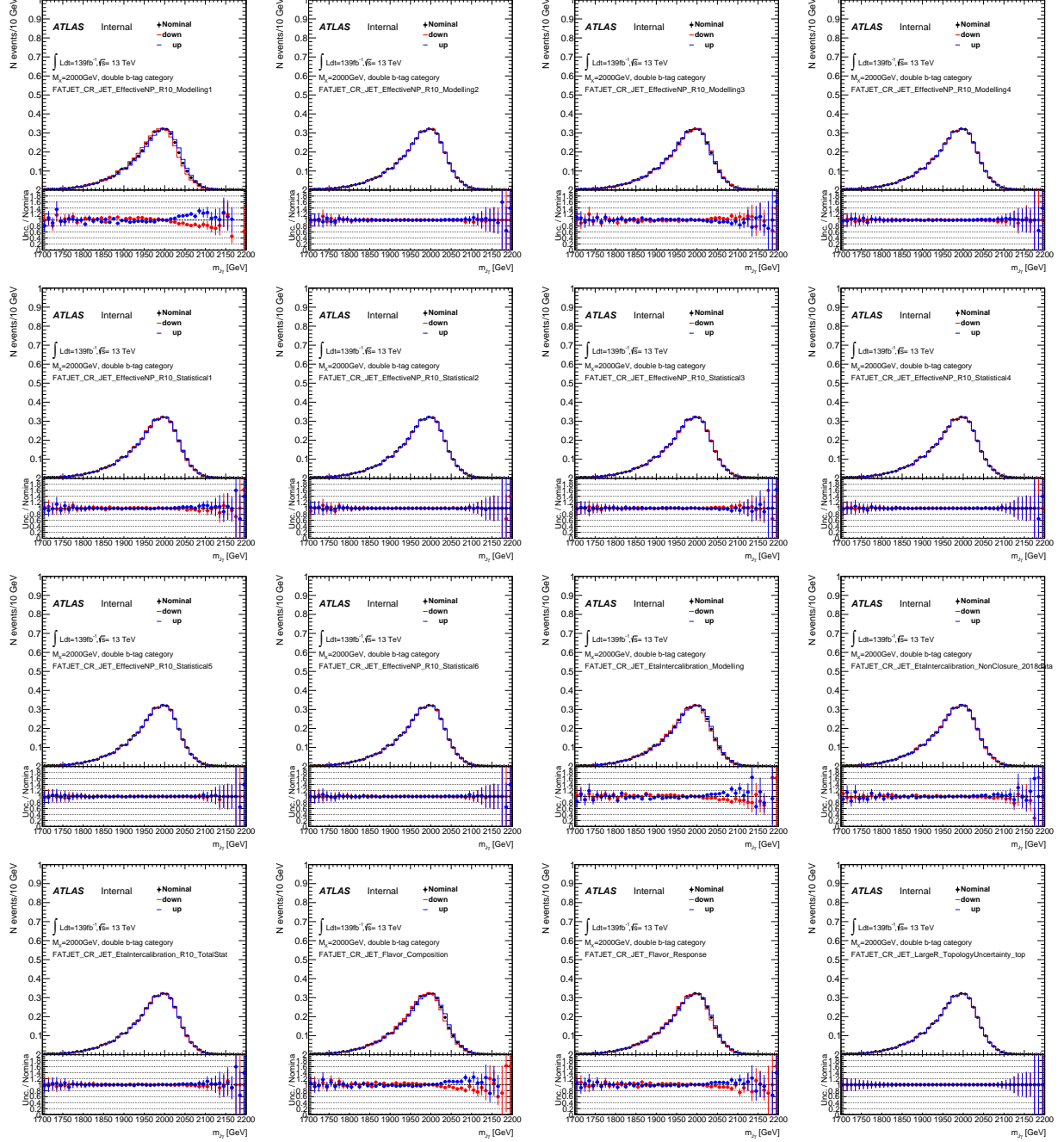


Figure .10: Signal resonance mass at 2000 GeV, in double  $b$ -tagged SR. Comparison of  $H\gamma$  mass spectrum between nominal signal MC sample and all the systematic variations.

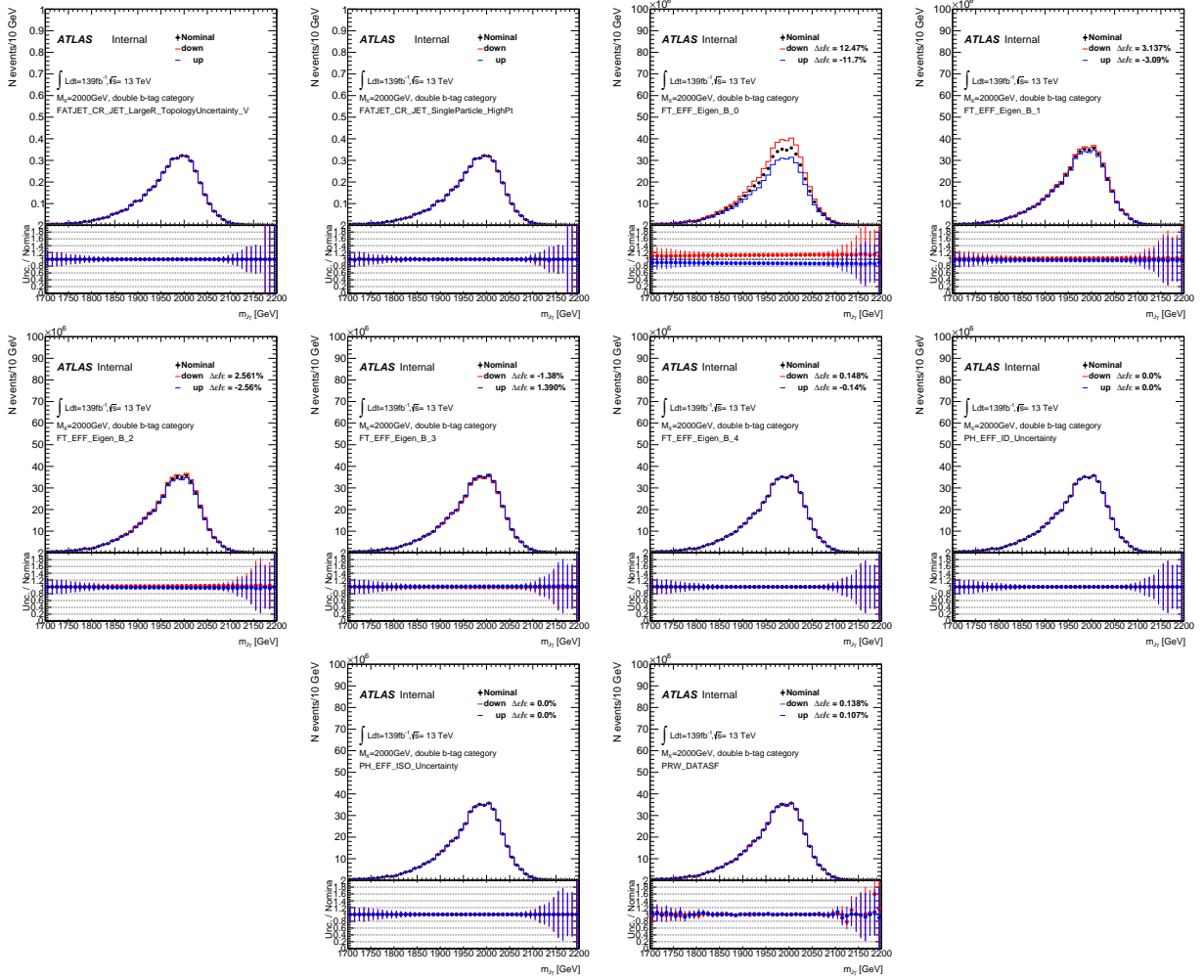


Figure .12: Signal resonance mass at 2000 GeV, in double  $b$ -tagged SR. Comparison of  $H\gamma$  mass spectrum between nominal signal MC sample and all the systematic variations.